IPP-Report

Raheesty Devi Nem

Surface Temperature Measurement of In-Vessel Components on ASDEX Upgrade using Infrared Spectroscopy

IPP 2017-10
Dezember 2017

Fakultät für Naturwissenschaften
Max-Planck-Institute for Plasma physics

Surface Temperature Measurement of In-Vessel Components on ASDEX Upgrade using Infrared Spectroscopy

Master thesis at University Ulm and Max-Planck-Institute for Plasma Physics, Garching Munich

Written by:
Raheesty Devi Nem
raheesty.nem@uni-ulm.de

Academic supervisors:
apl. Prof. Emanuele Poli
Dr. Thomas Eich

IPP supervisor:
Dr. Albrecht Herrmann

2017

Version: November 1, 2017

Contents

Abstract

Neutral beam injection (NBI) is one of the auxiliary heating methods used on ASDEX Upgrade. If the neutral beam is not completely absorbed by the plasma, it can deposit a heat load with a heat flux density of up to 40 $\frac{\mathrm{MW}}{\mathrm{m}^2}$, on the first wall. The heat load could damage the first wall. For machine protection, the **H**eat **S**hield **T**hermography (HST) system is used to observe the shine through locations of the beams. The current HST system uses two-color pyrometers at wavelengths of about 0.9 μm and 1.6 μm to evaluate the surface temperature. Volume radiation influences the measurement, resulting in an overestimation of the surface temperature. As a consequence, the NBI is switched off unnecessarily. Volume radiation like Bremsstrahlung has a continuous spectrum and therefore, the thermal radiation cannot be disentangle from the Bremsstrahlung by a two-color pyrometer. The aim of this work is to test a new diagnostic for the HST system by using infrared (IR) spectroscopy for more robust surface temperature evaluation. The surface temperature is deduced from the profile shape. A variety of models has been used where Planck's law with different emissivity functions are considered with an addition of Planck's law as well as Bremsstrahlung. The basic principles for the surface temperature evaluation using different devices like IR camera, two-color pyrometer and IR spectrometer is discussed. The influence of additional photon sources like reflections is discussed for a one-color pyrometer and a two-color pyrometer. The influence of Bremstrahlung on the HST system was investigated using synthetic data. In addition a sensitivity study for the spectroscopic measurement is carried out using synthetic data, where the influence of emissivity and Bremsstrahlung on the measurement is discussed. The spectrometer has been characterized in the lab, tested at the high heat flux test facility GLADIS and in ASDEX Upgrade. During the calibration process in ASDEX Upgrade a poor transmission of the optical fibre has been observed. The early switch off of the HST might be due to the poor transmission, as the surface temperature is overestimated. GLADIS results showed that the surface temperature can be evaluated using IR spetroscopy without any prior information about the material parameters and also that a sharp temperature rise can be detected sufficiently quick for a protection system. For unknown material parameters, a wavelength dependent emissivity needs to be considered because a constant emissivity leads to an overestimation of the surface temperature. From the ASDEX Upgrade results, it is seen that in the presence of a magnetic field and gas, a reduce heat flux is determined at the shine through location. The deflection of the part of the beam, which is ionized by the interaction with gas, together with an increased beam divergence is thought to be the reason for the reduced heat flux. The IR spectrometer has successfully measured the surface temperature in the presence of plasma and line radiations were observed during a plasma disruption.

1. Introduction

At the moment 80% of the world's primary energy is generated by coal, oil and natural gas. The burning of fossil fuels affects the climate and the environment due to the release of greenhouse gases such as carbon dioxide. It is desirable to replace the burning of fossil fuel by alternative energy sources. Therefore new ways for producing electricity are being investigated. Nuclear fusion is a promising candidate which in contrast to fossil fuel does not produce greenhouse gases. There is enough fuel in seawater for nuclear fusion to supply the world with energy for millions of years. Small amounts of fuel would be needed to run a nuclear fusion power plant. The current tokamaks used for fusion research do not produce a net surplus fusion energy. The next step is the International Thermonuclear Experimental Reactor (ITER). It is designed to demonstrate the possibility to produce more power by fusion than is needed to heat the plasma. ITER is not designed to produce electricity but to resolve critical scientific and technical issues. ITER is foreseen to produce 500 MW of fusion power from an input power of 50 MW. In case of success, this will lead to the next step: DEMO - A demonstration fusion power plant. In this chapter the theoretical background of nuclear fusion is presented and the working principle of a tokamak is described.

1.1. Nuclear Fusion

The process of combining two or more light nuclei together, to form a heavier nucleus is called nuclear fusion.

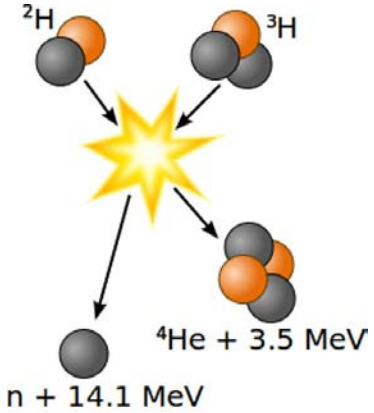

Figure 1.1.: The fusion of deuterium and tritium forming a helium atom and releasing a neutron and 17.6 MeV [1].

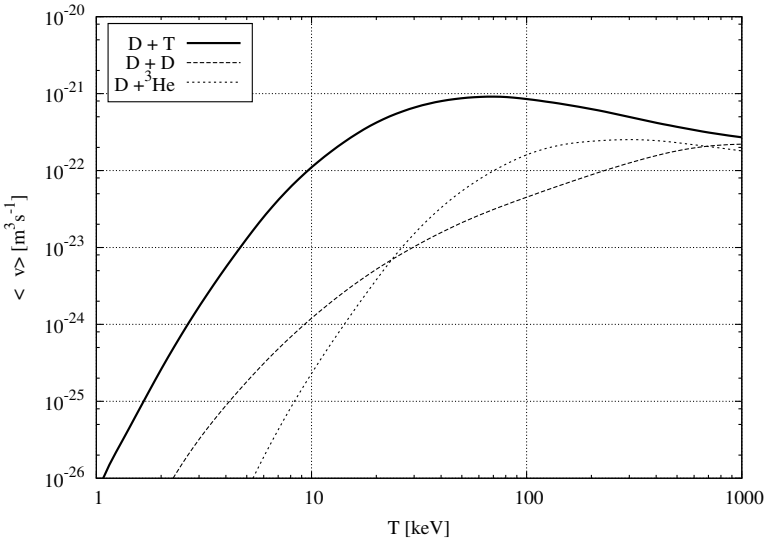

Figure 1.2.: The rate coefficient of different fusion reactions [2].

There are various types of fusion reactions, that may occur:

$$\mathrm{D} + \mathrm{D} \rightarrow \mathrm{He}_2^3 + \mathrm{n} + 3.3\ \mathrm{MeV} \tag{1.1}$$

$$\mathrm{D} + \mathrm{D} \rightarrow \mathrm{T} + \mathrm{p} + 4.0\ \mathrm{MeV} \tag{1.2}$$

$$\mathrm{D} + \mathrm{He}_2^3 \rightarrow \mathrm{He}_2^4 + \mathrm{p} + 18.4\ \mathrm{MeV} \tag{1.3}$$

$$\mathrm{D} + \mathrm{T} \rightarrow \mathrm{He}_2^4 + \mathrm{n} + 17.6\ \mathrm{MeV} \tag{1.4}$$

The most promising reaction, for the use in a fusion power plant is that of deuterium and tritium because this reaction has the highest fusion cross section at the lowest energy. Figure 1.1 shows an illustration of deuterium tritium fusion and in figure 1.2 the rate coefficient of the different fusion reactions are shown in dependence of the temperature.

Tritium has a half-life of 12.3 years and therefore does not occur in nature. Tritium can be bred from lithium using the neutron released by the deuterium-tritium reaction 1.4. For the two lithium isotopes, the following reactions are possible:

$$\mathrm{n} + \mathrm{Li}_3^6 \rightarrow \mathrm{He}_2^4 + \mathrm{T} + 4.8\ \mathrm{MeV} \tag{1.5}$$

$$\mathrm{n} + \mathrm{Li}_3^7 \rightarrow \mathrm{He}_2^4 + \mathrm{T} + \mathrm{n} - 2.5\ \mathrm{MeV} \tag{1.6}$$

Lithium-6 will be used for tritium breeding together with neutrons multipliers such as beryllium. Lithium-7 is not suitable due to the low reaction cross section. Deuterium and lithium are abundant on our planet, providing almost inexhaustible sources for nuclear fusion for around 10^7 years [3].

For the fusion reactions to occur, high temperatures of around 150 million Kelvin are needed. At such high temperatures the atoms are fully ionized and the fuel is in the state of plasma. There is no wall material that can withstand such a high temperature. Therefore, the plasma must not have direct contact to the wall. Magnetic fields are used to confine the plasma, because it is made up of ionized particles which can be trapped in a magnetic field. A pinch, which is the compression of an electrically conducting

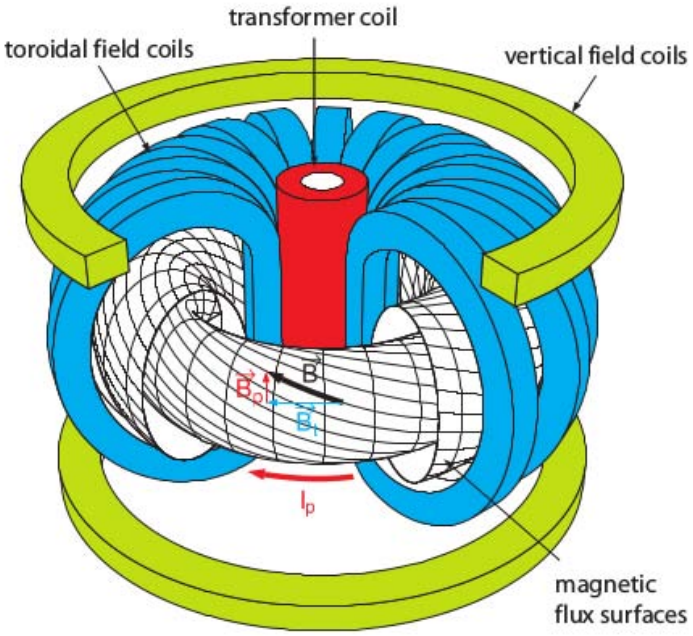

Figure 1.3.: Schematic view of the tokamak principle [2].

filament by magnetic forces, may be used for plasma confinement. Unfortunately the linear configuration of a pinch has large end losses. These end losses can be avoided in a toroidal system but a simple toroidal system is unstable due to the E× B drift that arises from charge seperation due to the drift of the particles in inhomogeneous magnetic field [4]. Therefore, the magnetic field lines are twisted helically by a toroidal plasma current to prevent charge separation to suppress in the E× B drift. Thus, creating a tokamak.

1.2. Tokamak

So far the most advanced confinement concept is the tokamak. In the following section the basic principles of a tokamak will be described [5]. The tokamak is a magnetic confinement concept with a torus shaped vacuum vessel which contains the plasma. Experimental research of tokamak systems started in 1956 in the Kurchatov Institute, Moscow, by a group of Soviet scientists led by Lev Artsimovich [6]. The group constructed the first tokamaks, the most successful being T-3.

The tokamak consists of three sets of magnetic field coils, as shown in figure 1.3.

1. The first set of coils are the toroidal magnetic field coils (blue). These coils produce a toroidal magnetic field.

2 The poloidal field coils (green) create a vertical magnetic field. The poloidal field coils are used for the control of the plasma shape and position.

3 The central solenoid is the third component of the magnet system. By changing the current in the central solenoid, which is essentially the primary winding of a large

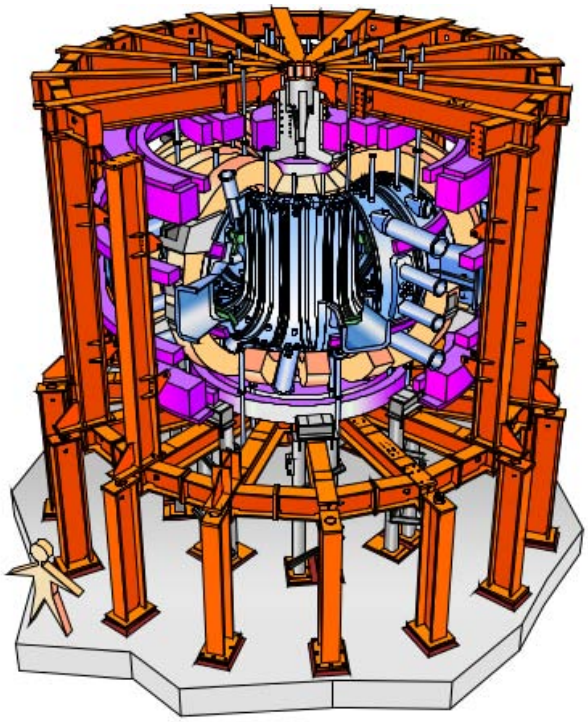

Figure 1.4.: A cut away picture of the ASDEX Upgrade tokamak [8]

transformer, a toroidal electric field is induced, which leads to the formation of the toroidal plasma current (the plasma acting as the secondary winding). The plasma current leads to a poloidal magnetic field which confines the plasma. The confinement of the plasma is described by $\mathbf{j} \times \mathbf{B} = \nabla \mathrm{p}$, where $\boldsymbol{j}$ is the current density, p is the pressure and $\boldsymbol{B}$ is the magnetic field.

1.3. ASDEX Upgrade

The **A**xial **S**ymmetric **D**ivertor **Ex**periment Upgrade or short ASDEX Upgrade, is in operation since 1991 at the Max Planck Institute for Plasma Physics in Garching, Germany [7]. It has a plasma volume of around 13 cubic metres. It can operate with a magnetic field up to 3.9 T. The tokamak has a major radius of 1.65 m and a minor radius of 0.5 m. ASDEX Upgrade has three different sources for auxiliary heating [7]:

- Neutral beam injection (NBI): 20 MW
- Ion cyclotron (ICRH) heating: 6 MW
- Electron cyclotron (ECRH) heating: 4 MW

In 2007 ASDEX Upgrade, figure 1.4, which initially started operating with carbon plasma facing components, was the first tokamak to demonstrate operation with tungsten as first wall material [9]. The aim of ASDEX Upgrade is to study the behaviour of a magnetically confined plasma in a reactor relevant environment [10].

1.4. Neutral Beam Injection

Neutral beam injection (NBI) is one of the three auxiliary method used to heat the plasma. The NBI system at ASDEX Upgrade delivers a power of up to 20 MW. The plasma is heated by the absorption of energy from the neutral particles due to collisions. Neutral particles are used because they are not deflected by the magnetic field. Figure 1.5 illustrates the working principle of the neutral bean injection in ASDEX Upgrade. To start with, a gas, usually deuterium, is ionized. The ionized particles are accelerated over an electrical grid, resulting in energetic ionized particles. The particles are then neutralized in a gas target neutralizer. Any non-neutralized ions in the neutral beam are then deflected onto an ion dump using a magnetic field, as shown in figure 1.5.

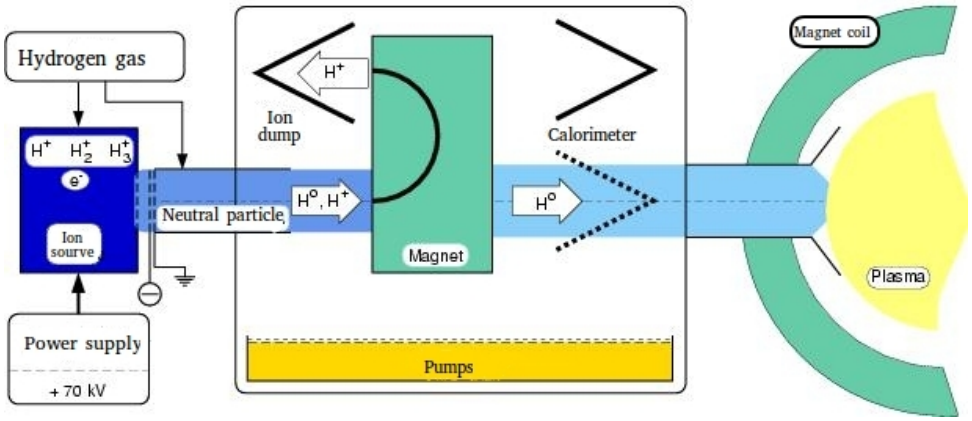

Figure 1.5.: Illustration of the working principle of the neutral beam injection [11].

In the plasma, the neutral particles ionize and lose their high energy due to Coulomb collisions, thus, heating the plasma. ASDEX Upgrade is equipped with two neutral beam injectors, each with four neutral beam sources. NBI1 has a full particle energy of 60 keV while NBI2 has 93 keV. Depending on the initial beam energy and on the energy of the plasma electrons and ions, the high energetic particles can either heat the ions or the electrons. A movable calorimeter is mounted in front of the entrance of the torus duct to measure the heating power of the NBI and for conditioning the sources. Figure 1.6 (a) shows an overview of ASDEX Upgrade and the two beam boxes. The beams of NBI1 are all directed radially on the inner first wall. Beams of NBI2 is tilted toroidally, two of the four beams are directed radially on the inner first wall and two tangentially on the outer first wall. Figure 1.6 (b) shows the poloidal projection of the machine, where the shine through location of the six radial beams and two tangential beams are shown. If the plasma does not absorb the beams a high heat load is deposited at the shine through location,therefore, leading to possible erosion of the first wall or melting if metal is used as plasma facing material.

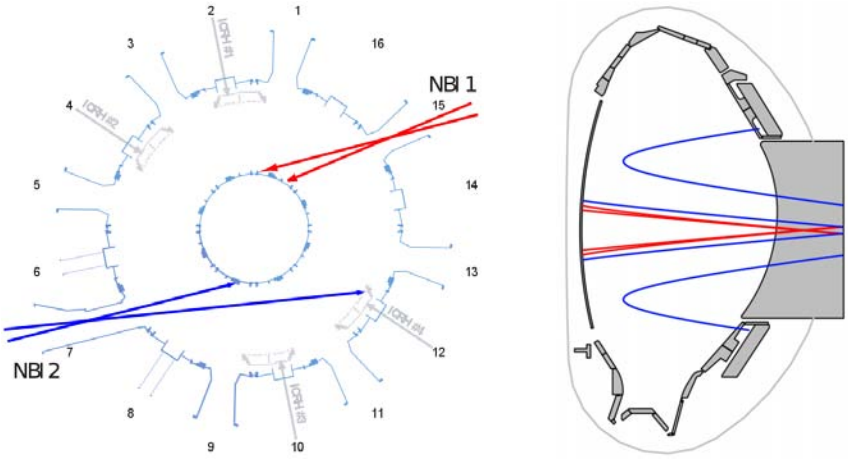

(a) Toroidal projection (b) Poloidal projection

Figure 1.6.: Neutral beam boxes and injection trajectories as seen in (a) toroidal projection and (b) in poloidal projection.

Heat **S**hield **T**hermography (HST) protects the first wall against shine through of the beams and is used to prevent damaging of the first wall by switching off the NBI heating system if overheating is detected. A detailed description of the HST is given in section 2.4.1. The support of the inner wall, see figure 1.7, is water cooled. The components mounted on the inner wall are therefore passively cooled. Figure 1.7 shows the internal view of ASDEX Upgrade as viewed radially from the NBI2. The lower and upper region in figure 1.7 shows the divertor and in the mid-plane three ICRH antennas. The shine through location of the tangential beams, as shown in figure 1.7, are on the protection of the ELM control coils of the outer first wall, where the surface temperature is not allowed to exceed 1500 K. The system measuring the surface temperature at the shine through location of the beams on the first wall uses two-color pyrometers.

The principle of infrared (IR) thermography is discussed in chapter 2. Chapter 3 discusses the uncertainties of IR spectroscopy for the temperature measurement using synthetic data. The calibration of the IR spectrometer used in the thesis is shown in chapter 4. Experimental results in the High Heat Flux test facility, GLADIS, and in ASDEX Upgrade are discussed in chapter 5 and 6 respectively. Conclusions are drawn together with an outlook in chapter 7.

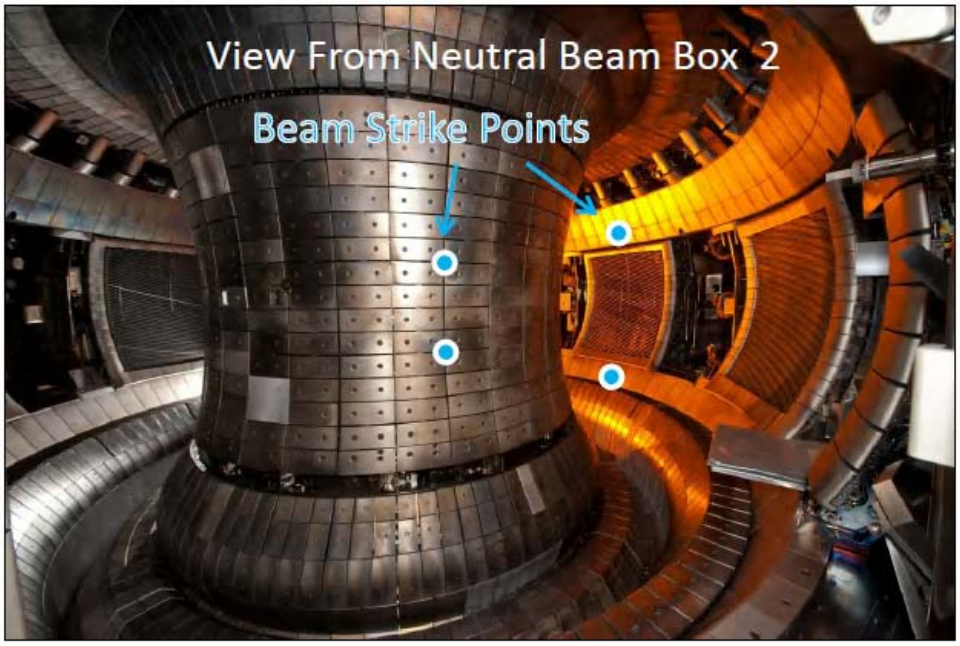

Figure 1.7.: The approximate radial and tangential shine through location as viewed from the neutral beam box 2.

2. IR Thermography

In the following section the measurement of the surface temperature using infrared (IR) thermography is discussed. Every surface emits photons which can be measured by different devices. Using Planck's law, the surface temperature can be determined from the photon flux measured. In this chapter a brief introduction of the different measuring devices and the method used for surface temperature evaluation is given. The influence of additional photon flux on the measurements due to reflection and volume radiation is discussed.

2.1. Radiation Laws

All bodies radiate or absorb electromagnetic radiation. The amount of radiation emitted depends on the temperature of the body. The relation between the temperature of a black body and the emitted photon flux is given by Planck's law. In this section Planck's law and other radiation laws derived from it are described.

2.1.1. Planck's Equation

Planck's law describes the photon emission of a black body, an idealized body that absorbs all incident electromagnetic radiation, at a given temperature. The emitted radiation has a spectrum that is determined by the temperature alone [12].

$$\mathrm{M}^0_\lambda(\lambda, T)\mathrm{d}A\mathrm{d}\lambda = \frac{2\pi hc^2}{\lambda^5} \cdot \frac{1}{\exp\left(\frac{hc}{\lambda k_B T}\right) - 1}\mathrm{d}A\mathrm{d}\lambda \qquad \left[\frac{\mathrm{W}}{\mathrm{m}^2\ \mathrm{nm}}\right] \tag{2.1}$$

M^0_λ (λ, T) indicates the power emitted per area dA and wavelength interval dλ. λ denotes the wavelength of the emitted photons, h is the Planck constant, c the speed of light in vacuum, k_B is the Boltzmann constant and T the temperature of the black body.

Figure 2.1 shows the spectral emission of a black body at different temperatures. The peak of the spectral radiance shifts toward smaller wavelength for higher temperatures.

In reality surfaces are not ideal black bodies. The deviation from a black body is described by the so called emissivity ε. If $\varepsilon = 1$ the surface is a black body and if $\varepsilon = 0$ the surface does not absorb or emit any radiation.

The emissivity is influenced by the material and the condition of the surface. This can lead to an over or underestimation of the temperature if the emissivity is not known. The

emissivity is defined as the ratio of the radiant flux emitted per unit area by the surface of an object to that of a black body at the same temperature [13]:

$$\varepsilon(\lambda, T) = \frac{i_{obj}(\lambda, T)}{i_{bb}(\lambda, T)} \tag{2.2}$$

where i_{obj} is the radiance of an object's surface and i_{bb} is the radiance of a black body. The emissivity of a body depends on different factors such as the temperature of the body, wavelength of the emitted energy and angle of emission.

With the emissivity ε Planck's law is extended as follows [8]:

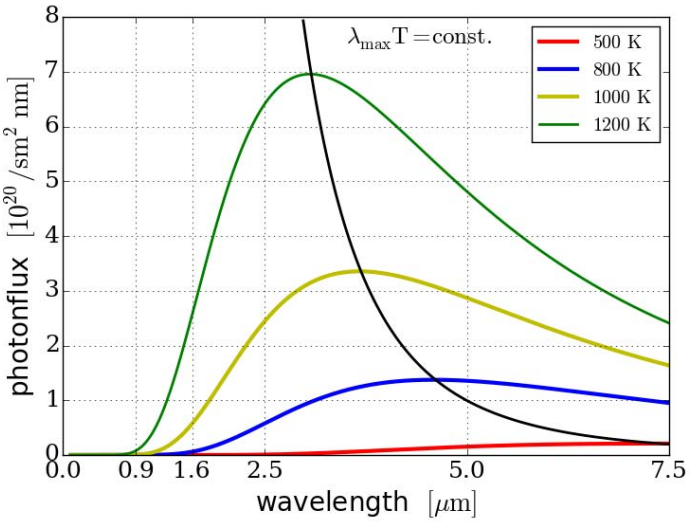

Figure 2.1.: Photon flux of an ideal black body at different temperatures with Wien's displacement law.

$$\mathrm{I}_\lambda(\lambda, T)\mathrm{d}A\mathrm{d}\lambda = \epsilon\frac{2\pi hc^2}{\lambda^5} \cdot \frac{1}{\exp\left(\frac{hc}{\lambda k_B T}\right) - 1}\mathrm{d}A\mathrm{d}\lambda \qquad \left[\frac{\mathrm{W}}{\mathrm{m}^2\ \mathrm{nm}}\right] \tag{2.3}$$

By dividing equation 2.3 by the energy of a photon $E = \frac{hc}{\lambda}$ the photon flux Γ is obtained, which is the number of photons emitted per surface area $\mathrm{d}A$ and wavelength interval $\mathrm{d}\lambda$ per second.

$$\Gamma_\lambda \mathrm{d}A\mathrm{d}\lambda = \varepsilon\frac{2\pi c}{\lambda^4} \cdot \frac{1}{\exp\left(\frac{hc}{\lambda k_B T}\right) - 1}\mathrm{d}A\mathrm{d}\lambda \qquad \left[\frac{1}{\mathrm{s}\,\mathrm{m}^2\ \mathrm{nm}}\right] \tag{2.4}$$

The photon flux for evaluation is required here since the scientific IR cameras used at ASDEX Upgrade are photon detectors (diodes), in contrast to bolometers, which are based on IR detectors.

2.1.2. Wien's Displacement Law

Wien's displacement law is derived by considering the following equation:

$$M_\lambda(\lambda, T) = \frac{2\pi hc^2}{\lambda^5} \cdot \frac{1}{\exp\left(\frac{hc}{\lambda k_B T}\right) - 1} \tag{2.5}$$

To find the position of the maximum, function $M_\lambda(\lambda, T)$ is differentiated and equated to zero, thus, leading to the following simplified equation:

$$\frac{hc}{\lambda k_B T} \frac{\exp(\frac{hc}{\lambda k_B T})}{1 - \exp(\frac{hc}{\lambda k_B T})} = 5 \tag{2.6}$$

This equation is solved iteratively giving, $hc/\lambda k_B T = 4.965$. Solving for the wavelength in µm and temperature T in K gives:

$$\lambda_{\max} = \frac{2898\,\mu\text{m} \cdot \text{K}}{T} \qquad [\mu\text{m}] \tag{2.7}$$

From equation 2.7, it is deduced that objects of different temperatures emit different spectra which peak at different wavelength. Since the wavelength is inversely proportional to the temperature of the object, hotter objects have a maximum at shorter wavelength and cooler objects emit spectra which peaks at longer wavelengths. The maximum of the spectra are identified by Wien's displacement law.

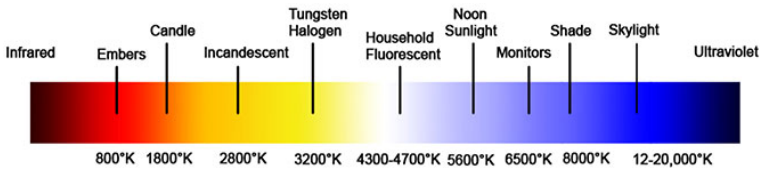

Figure 2.2.: Illustration of the color change at different temperatures [14].

Figure 2.2 shows how the color changes with increasing temperature. It is seen that with increasing temperature the color changes from red to blue.

2.1.3. Wien's Law

A simplified version of the Planck equation 2.1 for short wavelength is formed for the limit $\frac{hc}{\lambda k_B T} \gg 1$. This is known as Wien's approximation. Wien's approximation applies when the wavelength is well below the peak of the spectral radiance.

From equation 2.4 follows:

$$\Gamma_\lambda \mathrm{d}A\mathrm{d}\lambda = \varepsilon \frac{2\pi c}{\lambda^4} \cdot \frac{1}{\exp\left(\frac{hc}{\lambda k_B T}\right)} \mathrm{d}A\mathrm{d}\lambda \qquad \left[\frac{1}{\text{sm}^2\ \text{nm}}\right] \tag{2.8}$$

The surface temperature is obtained by rearranging equation 2.8:

$$\mathrm{T}(\lambda, \Gamma) = \frac{hc}{\lambda k_B \ln\left(\frac{2\pi\varepsilon c}{\lambda^4 \Gamma_\lambda}\right)} \qquad [\mathrm{K}] \tag{2.9}$$

2.1.4. Rayleigh-Jeans Law

Rayleigh-Jeans law is the long wavelength approximation of Planck's law. It states that the intensity is proportional to the temperature of the body and inversely proportional to the fourth power of the wavelength. The photon flux is:

$$\Gamma_\lambda(\lambda, T) = \frac{2\pi k_B T}{h\lambda^3} \mathrm{d}A\mathrm{d}\lambda \qquad \left[\frac{1}{\mathrm{sm}^2\ \mathrm{nm}}\right] \tag{2.10}$$

$$\Gamma(T) = \int_0^\infty \frac{2\pi k_B T}{h\lambda^3} \mathrm{d}A\mathrm{d}\lambda = \infty \tag{2.11}$$

Figure 2.3 shows Wiens's approximation and Rayleigh-Jeans law in comparison to Planck's law. Wien's law holds for short wavelengths, Rayleigh-Jeans law is valid for only long wavelengths. The Rayleigh-Jeans law fails for short wavelengths. Equation 2.11 shows that Rayleigh-Jeans law diverges for small wavelengths. Since this does not actually happen, this discrepancy is known as the UV catastrophe.

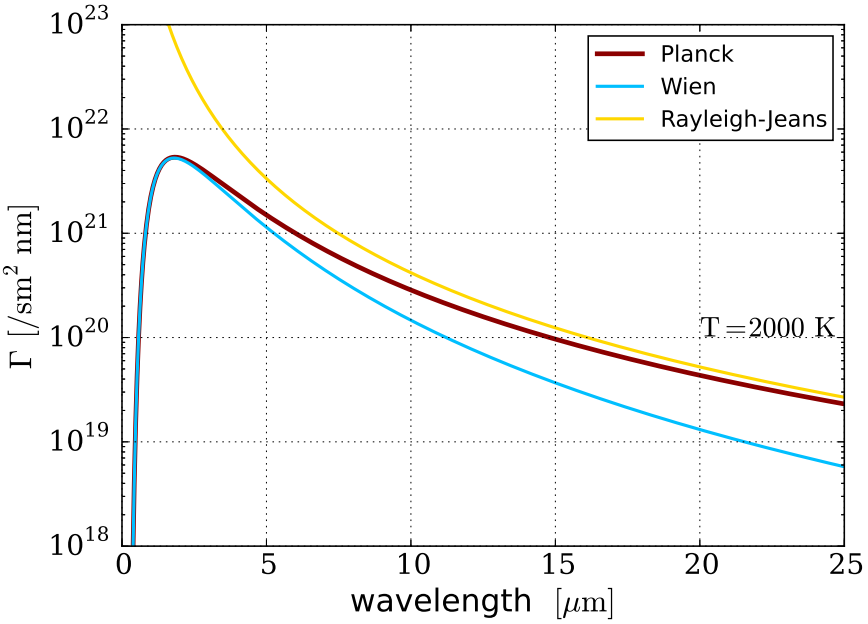

Figure 2.3.: Photon flux of an ideal black body at a temperature of 2000 K as described by Planck's equation (red), Wien's approximation (blue) and Rayleigh-Jeans law (yellow).

2.2. Method for Surface Temperature Evaluation

In the following section the temperature measurement of diode based one-color and two-color pyrometers is discussed.

2.2.1. One-Color Pyrometer

An example of a one-color pyrometer is an IR camera. Scientific IR cameras measure the photon flux. For a given wavelength and the measured photon flux, equation 2.4 can be rearranged to solve for the surface temperature T. The resulting equation is as follows:

$$T(\lambda, \Gamma) = \frac{hc}{\lambda k_B \ln(\frac{2\pi\varepsilon c c_0}{\lambda^4 \Gamma} + 1)} \tag{2.12}$$

$$c_0 = \mathrm{d}A \cdot \mathrm{d}\lambda \tag{2.13}$$

where c_0 is a constant containing information about the bandwidth and solid angle of the camera. The emissivity in equation 2.12 is assumed to be constant. For the experiment at ASDEX Upgrade, the equation is solved numerically because the emissivity of tungsten is temperature dependent. Since the IR camera is quasi monochromatic, the wavelength dependency of the emissivity is not considered. The spectral range for the IR camera in ASDEX Upgrade is about $3.6 - 4.9\,\mu$m. The wavelength range is a compromise between the temperature range to be measured and the camera resolution [15]. Figure 2.4 shows the photon flux of a black body in dependence to the temperature of four different photon wavelengths.

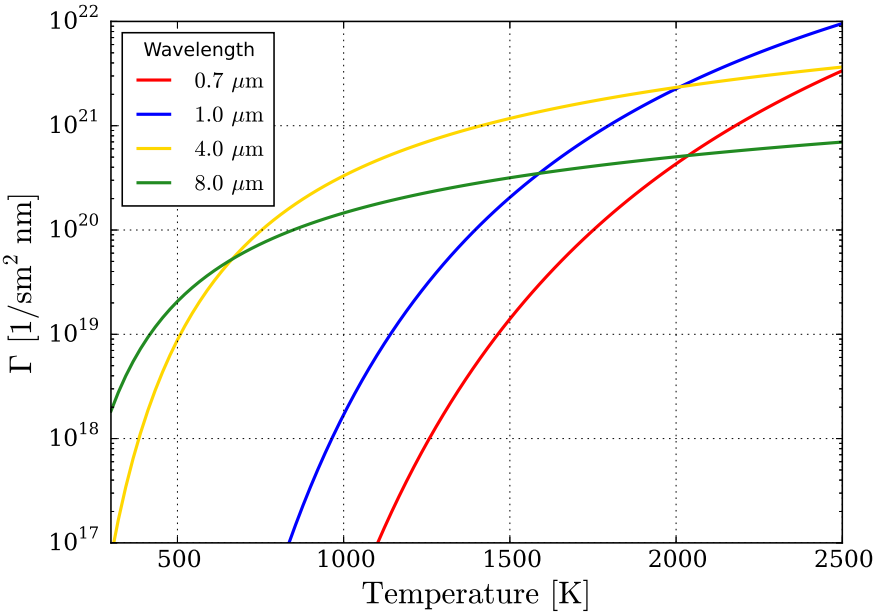

Figure 2.4.: Photon flux of an ideal black body in dependence of the temperature of photons at different wavelength.

It is observed that for wavelengths in near IR range (0.7 and 1.0 μm), the photon flux is low at low temperatures. For 0.7 μm (red), the photon flux increases significantly as from 1100 K and for 1.0 μm a strong increases of the photon flux is observed as from 800 K. This implies that the wavelengths are not suitable for low surface temperature measurement but can be used at high temperatures. The HST system in ASDEX Upgrade uses two-color pyrometers at wavelengths of 0.9 and 1.6 μm.

For a wavelength of 4 μm (yellow) the photon flux rises significantly over the temperature range of 300 - 2500 K. For the IR camera in ASDEX Upgrade wavelength from this region (mid-wavelength IR) is chosen for a good coverage of the surface temperature over the whole divertor [15].

A wavelength of 8 μm belongs to the long wavelength IR region. It is observed that at 8 μm (green) the photon flux at low temperatures is higher compared to the 4 μm wavelength but at high temperatures this trend is reversed. As from 700 K, the photon flux calculated for the wavelength of 4 μm increases faster than at 8 μm. The long wavelength region can be used for systems that measure low photon fluxes resulting in only small temperature increase.

2.2.2. Two-Color Pyrometer

A two-color pyrometer measures the photon flux at two different wavelengths. To determine the surface temperature the ratio of the photon flux at the two different wavelengths is calculated:

$$\frac{\Gamma_1(\lambda_1,T)}{\Gamma_2(\lambda_2,T)} = \frac{\varepsilon_1}{\varepsilon_2}\left(\frac{\lambda_2}{\lambda_1}\right)^4 \cdot \frac{\left(\exp\left(\frac{hc}{\lambda_2 k_B T}\right)-1\right)}{\left(\exp\left(\frac{hc}{\lambda_1 k_B T}\right)-1\right)} \tag{2.14}$$

The Planck's functions can be simplified for short wavelengths, if Wien's approximation is fulfilled, i.e $\lambda_{max}T < 2892\,\mu$mK [16]. The resulting photon flux ratio is then:

$$\frac{\Gamma_1(\lambda_1,T)}{\Gamma_2(\lambda_2,T)} = \frac{\varepsilon_1}{\varepsilon_2}\left(\frac{\lambda_2}{\lambda_1}\right)^4 \cdot \frac{\exp\left(\frac{hc}{\lambda_2 k_B T}\right)}{\exp\left(\frac{hc}{\lambda_1 k_B T}\right)} \tag{2.15}$$

Wien's approximation is valid for all wavelengths below the maximum of Wien's displacement law, as shown in figure 2.1. Taking the natural logarithm on both sides and solving for the surface temperature T, the following equation is obtained:

$$T(\lambda_{1,2},\Gamma_{1,2}) = \frac{hc}{k_B}\left(\frac{\lambda_1-\lambda_2}{\lambda_1\lambda_2}\right) \cdot \frac{1}{\ln\left((\frac{\lambda_1}{\lambda_2})^4 \cdot \frac{\varepsilon_2\Gamma_1(\lambda_1)}{\varepsilon_1\Gamma_2(\lambda_1)}\right)} \tag{2.16}$$

The inner heat shield of ASDEX Upgrade is made up partly of steel tiles and tungsten coated graphite. Metallic surfaces have low emissivities and require therefore short wavelengths for correct measurements. At short wavelengths the error in the radiation measurement due to emissivity is not significant and with the assumption that the surfaces

are true gray bodies, the ratio of the emissivity is then one. For low surface temperatures and surfaces with low emissivities, the measurement range of a two-color pyrometer should be between $0.5 - 2.5\,\mu$m.

2.3. Volume Radiation

Volume radiation is mainly made up of line radiation and Bremsstrahlung. The presence of volume radiation can result in a corrupt temperature evaluation. Volume radiation acts a an additional source of photons and influence on the measurements is similar to the influence produced by reflections. By choosing a specific wavelength range for the measurements and using spectral filters in front of the IR detector, the unwanted line radiation can be avoided. Bremsstrahlung on the other hand has a broad spectrum and can therefore not be avoided by the use of filters.

2.3.1. Bremsstrahlung

Bremsstrahlung is electromagnetic radiation generated by the deceleration of charged particles [17].

In a plasma, the electrons are mostly deflected by the ions. Due to the deflection a change in velocity occurs, this deceleration generates electromagnetic radiation. Bremsstrahlung that is emitted from a plasma is also known as free-free radiation [17].

A commonly known application of Bremsstrahlung is the X-ray spectrum with a wavelength of 0.01 nm to 10 nm used in X-ray tubes (e.g. for medical examinations.).

The power spectral density of Bremsstrahlung radiated in a uniform plasma with electrons of temperature T_e, is described by the following equation [17]:

$$\mathrm{P}_\lambda\,\mathrm{d}\lambda = \frac{2\pi c}{\lambda^2}\frac{8\sqrt{2}}{3\sqrt{\pi}}\left[1-\left(\frac{n_e e^2\lambda^2}{4\pi^2 c^2\varepsilon_0 m_e}\right)\right]^{\frac{1}{2}} n_e^2 r_e^3\left[\frac{(m_e c^2)^{\frac{3}{2}}}{(k_B T_e)^{\frac{1}{2}}}\right] E_1\left(\frac{1}{2}\left(\frac{hc}{k_B\lambda T_e}\right)^2\right)\mathrm{d}\lambda \quad \left[\frac{\mathrm{W}}{\mathrm{m^3 m}}\right] \tag{2.17}$$

where n_e is the number density of electrons, r_e the classical radius of an electron, e is elementary charge, m_e is the mass of an electron, k_B is the Boltzmann constant and c is the speed of light and E_1 is a special function known as exponential integral [18].

Here the atomic number Z is assumed to be one for a pure deuterium plasma with n_e equal to n_i.

A small amount of Bremsstrahlung is radiated at low temperatures. The radiated Bremsstrahlung increases with increasing temperature and decreasing wavelength. Figure 2.5 shows the logarithmic representation of the photon flux for different electron temperatures for a constant electron density. For the temperature evaluation, it is assumed that the electron temperature at the scrape off layer will not fall below 5 eV.

Figure 2.6 shows the dependence of Bremsstrahlung on the wavelength for different densities. It is observed that the amount of photons radiated increases with increasing density.

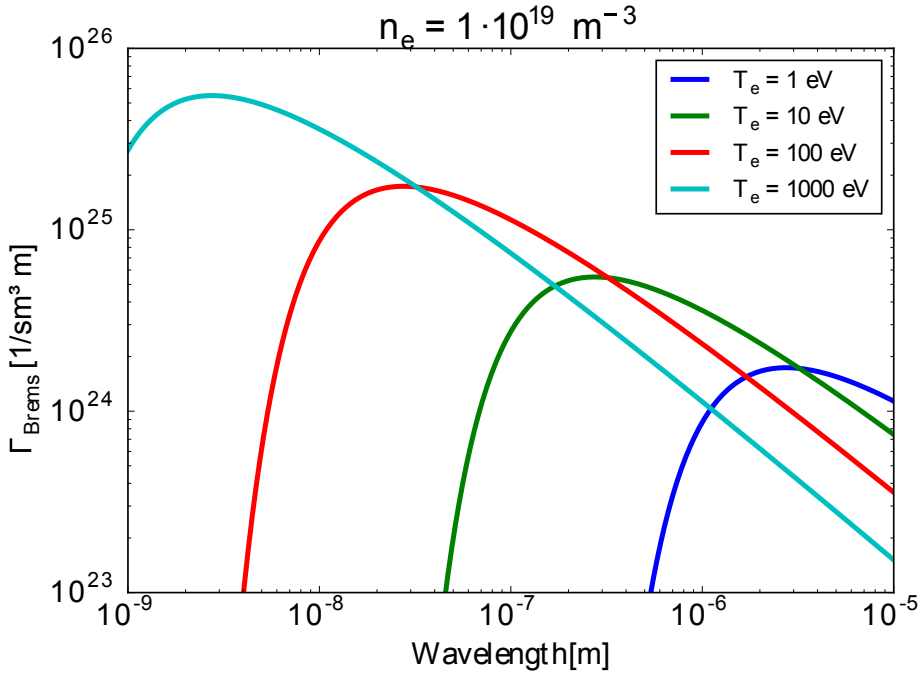

Figure 2.5.: The diagram shows the logarithmic dependence of Bremsstrahlung on the wavelength for different electron temperatures and for a constant density of $1 \cdot 10^{19}\,\mathrm{m}^{-3}$.

2.3.2. Line Radiation

Line radiation is observed when a bound electron in an ion, neutral or molecule undergoes a transition from an upper energy level (p) to a lower energy level (q) with energy $E(p)$ and $E(q)$ respectively . The spectral line is emitted at a wavelength frequency which is dependent on the element and the transition, thus acting as a fingerprint to identify an element or molecule. The wavelength of the photon emitted is then given as follows:

$$\lambda = \frac{hc}{E(p) - E(q)} \tag{2.18}$$

Each spectral line has a different intensity, meaning that the different transitions have different probability.

The spontaneous emission is described in terms of the Einstein coefficients A. The probability per unit time that an atom in state p emits a photon with wavelength λ_{pq} is written as:

$$P(p \to q) = A(p, q) \tag{2.19}$$

$I(\lambda, T)$ is the energy density at a wavelength λ and is defined by equation 2.1. In equilibrium, the rate of emission and rate of absorption have to be the same. The total emission

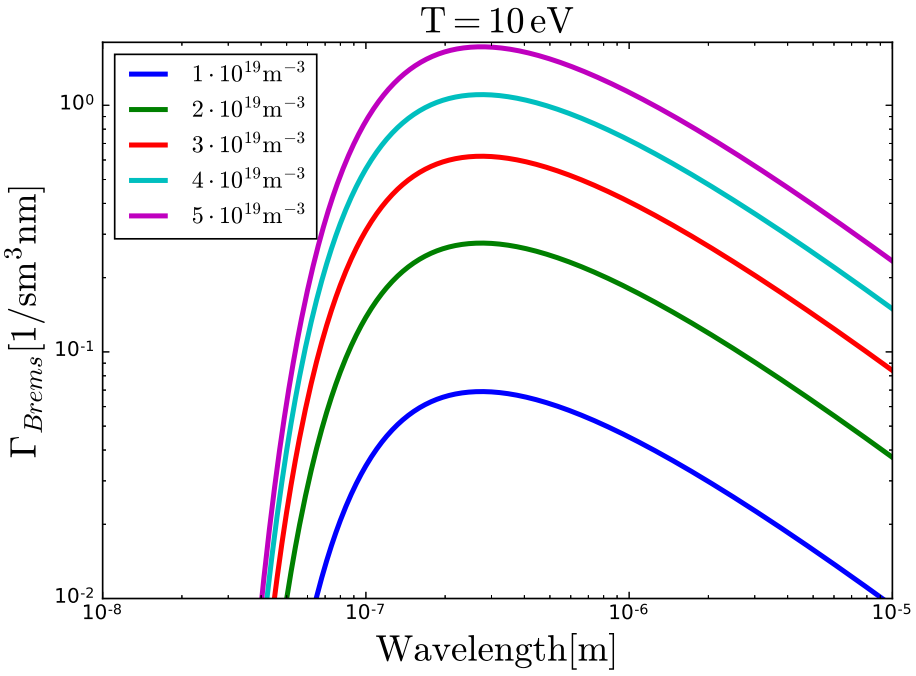

Figure 2.6.: The diagram shows the dependence of Bremsstrahlung on the wavelength for different densities, at a constant electron temperature of 10 eV

is therefore:

$$n(q)B(q,p)I(\lambda,T) = A(p,q)n(p) + B(p,q)I(\lambda,T)n(p) \tag{2.20}$$

The Einstein coefficients $B(p,q)$ and $B(q,p)$ are defined such that $B(p,q) \cdot I(\lambda,T)$ is the probability per unit time that the state p is induced to emit a photon and $B(q,p)I(\lambda,T)$ gives the probability per unit time that the state q absorbs a photon. The induced emission and absorption depend on the intensity of radiation $I(\lambda,T)$. Assuming a complete thermodynamic equilibrium at temperature T and applying Maxwell-Boltzmann statistics, the ratio of the population densities $n(p)$ and $n(q)$ of atoms in state p and q respectively is:

$$\frac{n(p)}{n(q)} = \frac{g(p)}{g(q)} \cdot \exp\left(-\frac{hc}{\lambda k_B T}\right) \tag{2.21}$$

where $g(p)$ and $g(q)$ are the statistical weights of a level p and q respectively. The relation between the Einstein coefficients are then:

$$B(p,q) = \frac{g(q)}{g(p)}B(q,p) \tag{2.22}$$

$$A(p,q) = \frac{2hc}{\lambda^3}B(p,q) \tag{2.23}$$

The total power radiated, P_t, in the line per unit solid angle is given as[19]:

$$P_t = \frac{hc}{4\pi\lambda} \cdot A(p,q)n(p) \tag{2.24}$$

For more detail please refer to [19].

2.4. Surface Temperature Evaluation

The aim of this thesis is to improve the safety and reliability of the HST diagnostics in ASDEX Upgrade. In this section the surface temperature evaluation method of the pyrometer and IR spectrometer is discussed. The following chapter describe the surface temperature measurement using two-color pyrometer and the IR spectrometer.

2.4.1. Pyrometery

The **H**eat **S**hield **T**hermography (HST) system uses a silicon - germanium sandwich diode to measure the signal. The sandwich diode acts as a two-color pyrometer which measures the surface temperature of the wall at two different wavelengths of $0.9\,\mu$m and $1.6\,\mu$m. The surface temperature is evaluated as described in section 2.2.2. Figure 2.7 shows the photon flux for different temperatures. The black line, which is Wien's displacement law, shows the peak of the spectrum for each temperature. Since a two-color pyrometer uses Wien's law for the temperature evaluation, the wavelengths chosen for the pyromters need to be on the ascending slope of the spectrum. The wavelengths used by the two-color pyrometer in ASDEX Upgrade are marked in orange and pale blue respectively.

For the measurements by the HST system, the ratio of the different emissivities is assumed to be constant. Since short wavelengths are used for the two-color pyrometer, the error in the measurement due to the emissivity is not significant.

2.4.2. IR Spectroscopy

In the presence of volume radiation the NBI can be switched off before the actual surface temperature limit is reached. The advantage of the IR spectrometer compared to the two-colour pyrometer is the wide spectral range of the spectrometer instead of using only two wavelengths. The wide spectral range allows one to disentangle black body radiation (from the surface) and Bremsstrahlung (from the plasma) in the measurement. This information is then used to derive the surface temperature. In this section the details and the working principle of an IR spectrometer is discussed.

The IR spectrometer used in this thesis is a commercially available spectrometer which is widely used for example in pharmaceutical and food industry to identify different organic substances and impurities detection in compounds. The spectrometer has a spectral range of $0.9 - 1.7\,\mu$m with a spectral resolution of 1.6 nm/pixel. The detector consists of an InGaAs line array with 512 pixels, with a sample ratio of up to 1 kHz, depending on the integration time.

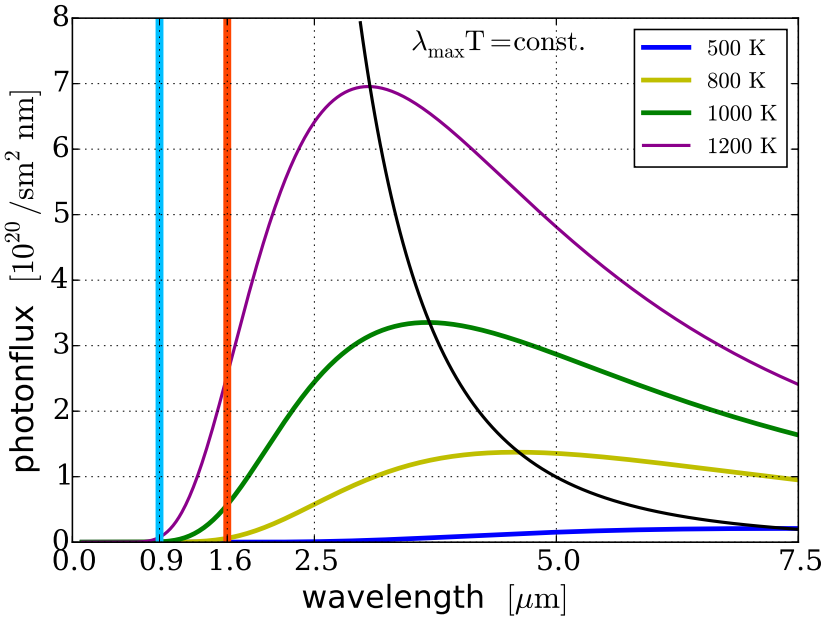

Figure 2.7.: Photon flux in dependence with the wavelength for different temperature.

Figure 2.8 shows a schematic representation of an IR spectrometer. An optical fibre is attached to the slit (1). The photons entering the slit are diffracted by a grating (2), which together with the width of the slit determines the resolution that the spectrometer will achieve. The diffracted photons then hit the detector (3). Each pixel in the detector represents a part of the spectrum which is converted by the electronics to a digital signal.

The surface temperature will be evaluated according to the shape of the spectrum obtained. Different models are used to fit the spectra. For the interpretation of the measurements three different models are used:

- Planck's Model
- Bremsstrahlung Model
- Line radiation

To evaluate the surface temperature in the ASDEX Upgrade, a combination of Planck and Bremsstrahlung equation is used. Depending on the fuelling gas used during the plasma discharges, line radiation has to be included in the evaluation models. However, as will be shown in section 6.6.2, the line spectra are rather complex and additional knowledge of the specific change of states is required for the analysis, which is not part of this thesis. The spectrometer is aimed to deliver a robust surface temperature measurement to prevent the NBI from switching off unnecessarily.

Figure 2.8.: Illustration of the working principle of an IR spectrometer [20]. 1 = slit 2 = grating 3 = detector 4 = optical bench

3. Temperature Measurement

In this chapter synthetic data is used to study the influence of systematic and statistical error on the temperature evaluation. The influence of Bremsstrahlung on the temperature evaluation is discussed for a one-color pyrometer and a two-color pyrometer. The effect of Bremsstrahlung on the HST system and the new IR spectroscopic system is shown with the help of synthetic data.

3.1. Influence of Volume Radiation

In the following section the influence of volume radiation on the surface temperature measurement using one-color and two-color pyrometers is discussed. Since the pyrometers measure at specific wavelengths, the influence of volume radiation on the measurement is similar to additional photons due to reflections.

3.1.1. One-Color Pyrometer

Since 2007 ASDEX Upgrade operates with all tungsten plasma facing components [9]. For IR thermography, metallic surfaces have the disadvantage of low emissivity ($\varepsilon \approx 0.05 - 0.4$) and high reflectivity compared to the previously used graphite ($\varepsilon \approx 0.9$). The low emissivity of the metal surface leads to a significant reduction of the emitted photon flux for the same temperature. Therefore additional photon sources like reflections can add significant photon flux to the measured signals, which can influence the temperature measurement.

Synthetic data for a one-color pyrometer at ASDEX Upgrade (IR camera) is generated for different surface temperatures by addition of different photon contributions at a constant background temperature:

$$\Gamma_{total} = \varepsilon \Gamma_{surface} + \varepsilon R \Gamma_{bb} \tag{3.1}$$

Here Γ_{total} is the total photon flux calculated for the IR camera. The emissivity ε, is assumed to be 0.3 and Γ_{bb} is the photon flux of a black body. R is the additional photon contribution on the synthetic data. Figure 3.1 shows the influence of of additional photons due to reflection, with a background radiator at a temperature of 700 K, on the measurements of an IR camera at a wavelength of 4.7 μm. Figure 3.1 shows how the error in the measurement varies with surface temperature and additional photon contribution. In order to determine the influences of additional photon flux on the temperature measurement, a scan of different contributions is carried out. Zero percent photon contribution represent the ideal data. From figure 3.1, it is seen that the error in the temperature

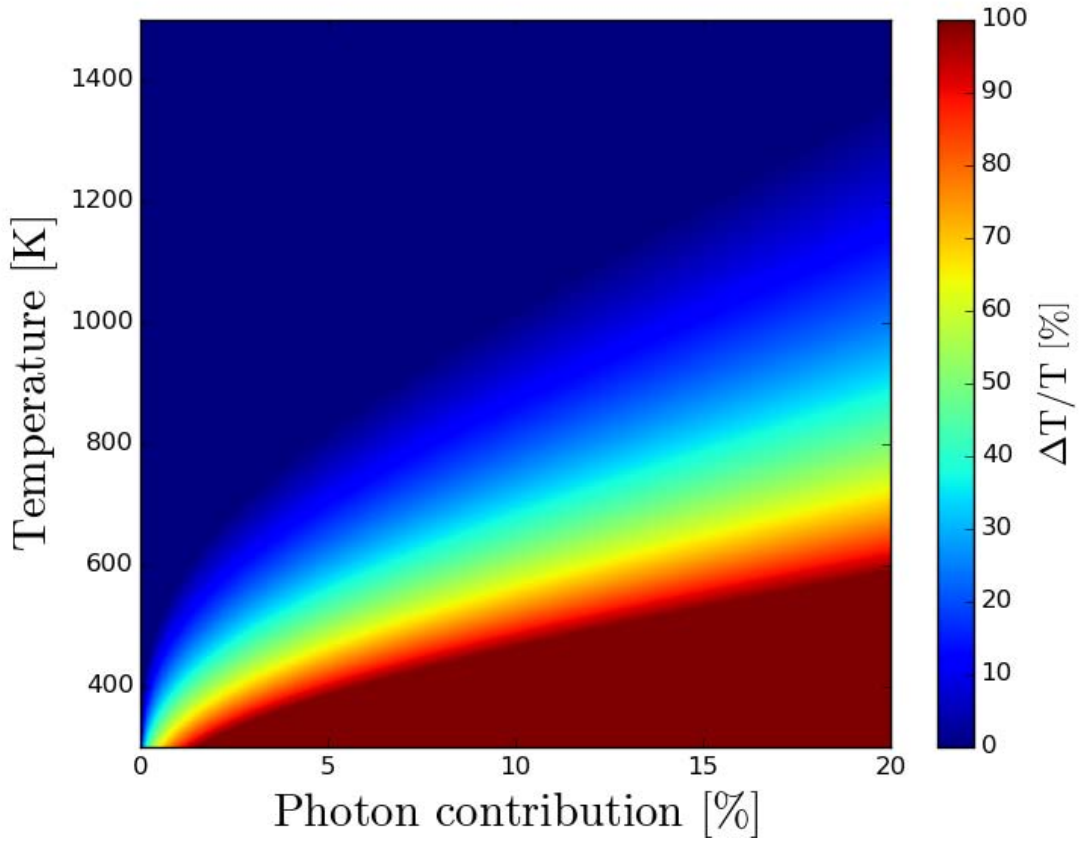

Figure 3.1.: Error calculated for the surface temperature measurement due to reflection from a source with a constant temperature of 700 K.

evaluation increases with increasing photon contribution due to reflection. Comparing the error obtained for high surface temperatures with those of low surface temperatures, it is seen that the error in the surface temperature measurement is significant only for low surface temperatures.

3.1.2. Two-Color Pyrometer

For the evaluation of the surface temperature using a two-color pyrometer only black body radiation is assumed. Bremsstrahlung and line radiation are both a source of photons and have therefore the similar effect on a measurement as reflection. The addition of photons measured by the two-color pyrometer lead to an overestimation as well as an underestimation of the calculated surface temperature as explained below. Synthetic data for the two-color pyrometer is generated using equation 3.1 for two different wavelengths, namely 0.9 and 1.6 μm. The surface temperature is evaluated from the ratio of the two photon fluxes as explained in section 2.2.2.

Figure 3.2 (a) shows that surface temperature calculated from the ratio of the photon fluxes for a two-color pyrometer including a reflected background radiance at 700 K. The color white represents the correct surface temperature evaluation. Blue shows the under-

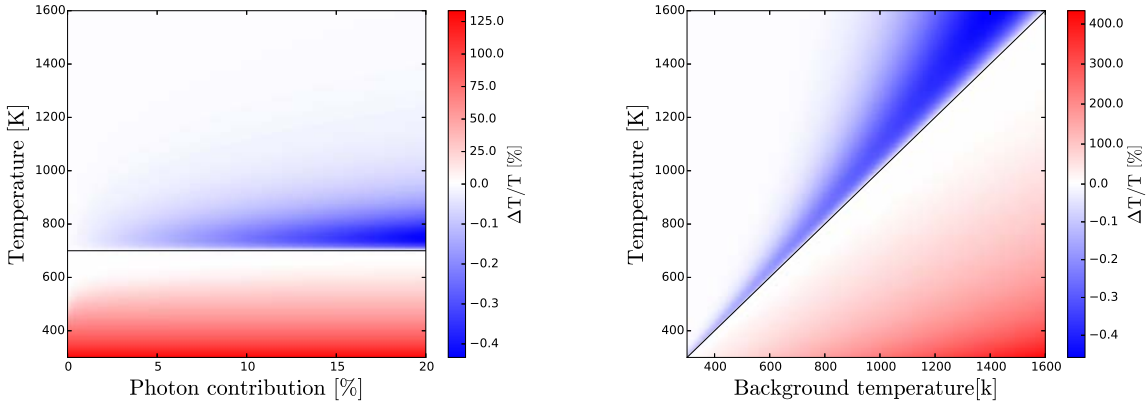

(a) Background with constant temperature of 700 K.

(b) Constant reflection of 10% for different background temperature.

Figure 3.2.: Figure(a) shows the error calculated for the surface temperature measurement with a two-color pyrometer due to reflection from a source at 700 K and figure (b) shows the error calculated for a constant reflection of 10% for different background temperature.

estimated surface temperature and red the overestimation of the surface temperature. It is observed that the surface temperature is significantly overestimated at temperatures below 700 K and has therefore a large error, marked in red. The black line shows the background temperature of 700 K. At 700 K, the surface temperature of the object and the background temperature are the same. The surface temperature is evaluated correctly (white color). For an object with temperature of above 700 K, it is seen that the surface temperature is underestimated, represented by the blue color. The temperature difference of the object and the background is small, and the object's temperature is higher than that of the background. Therefore, resulting in an underestimation of the surface temperature and the error is then negative. At high temperatures, the photon flux of the object is considerably larger than that of the background and therefore the influence of the background on the surface temperature evaluation becomes negligible. Figure 3.2 (b) shows the influence of 10% reflection, for different background temperatures, on the surface temperature evaluated for an object. The black line again represents the temperature when both the object and background have the same temperature. It is observed that the error in the surface temperature evaluation at high temperatures and around the black line is negligible since the influence of the background is negligible. At low temperatures and increasing background temperatures, the surface temperature of the object is overestimated, marked in red. The blue color represents the underestimation of the evaluated surface temperature. The percentage error calculated for the underestimation is about 0.4% whereas the percentage error in the overestimation of surface temperature is larger than 50%. Since the underestimation of the surface temperature is not as significant as the overestimation, it is not an issue for the machine protection.

It is concluded, that reflections and volume radiation at low temperatures affect the measurement of the surface temperatures significantly. At high temperatures, an additional photon flux due to reflections and volume radiation has only a minor influence on the determined surface temperatures.

3.1.3. Influence of Bremsstrahlung on the HST System

The HST system is efficient for high temperature measurements because only black body radiation is accounted. However, parasitic radiation like Bremsstrahlung and line radiation can influence the temperature evaluation. To investigate the influence

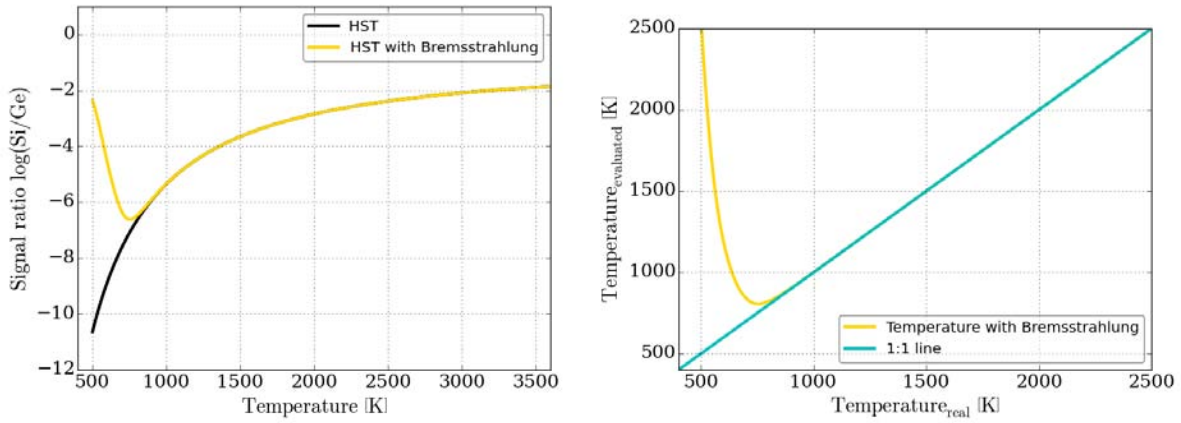

(a) Logarithmic signal ratio evaluated for HST

(b) Temperature evaluation.

Figure 3.3.: Figure (a) shows the ratio of silicon to germanium signal and figure (b) shows the evaluated temperature as measured by the HST.

of Bremsstrahlung on the HST system, equation 2.17 is added to Planck's equation to generate the photon flux for the HST system, which is then multiplied by the transmission and response of the diodes. Integrating the photon flux with respect to the wavelength gives the signal of each diode. For the measurements by the HST system, the ratio of the different emissivities is here assumed to be one. The HST system evaluates the surface temperature from the logarithmic ratio of the signal from the silicon and germanium diode. Figure 3.3 (a) shows the logarithmic signal ratio calculated in dependence to the surface temperature. The black curve shows the logarithmic signal ratio evaluated for the HST signal without taking Bremsstrahlung into consideration and in yellow the signal ratio accounting for Bremsstrahlung is shown. It is observed that at low temperature the influence of Bremsstrahlung on the temperature evaluation is significant. From the synthetic data, it is seen that as from 900 K the signal including Bremsstrahlung (yellow curve) follows the same path as the normal HST measurement (black curve). Due to the presence of volume radiation, an increased number of photons is measured at short wavelengths. This leads to an overestimation of the surface temperature at low temperatures as shown in figure 3.3 (b). With increasing surface temperatures the black body radiation dominates the measurements, leading to a negligible influence of Bremsstrahlung on the temperature evaluation.

3.2. Synthetic Data for IR Spectroscopic System

Synthetic data is generated to study the behaviour of different models for the evaluation of the surface temperature. To be able to evaluate the surface temperature using IR

thermography, the emissivity of the surface of the plasma facing components (PFCs) should be known as a priori [21]. Since ASDEX Upgrade has tungsten coated PFCs as well as bulk tungsten and steel [22, 9], the emissivity value can vary over a wide range. A study using synthetic data is conducted to see how the emissivity affects the surface temperature measurement.

3.2.1. Emissivity

IR thermography is often used to monitor the surface temperatures of plasma facing components in tokamaks. For IR thermography measurements, an accurate knowledge of the surface emissivity is important. However, the value of the emissivity can vary on a large range depending on many factors, for example the condition of the surface. The emissivity changes if the material used has a polished, unpolished or an oxidized surface. In addition it might be modified during plasma operation due to impurity deposition or erosion. Emissivity is a complex function dependent on variables like temperature, direction, wavelength, surface conditions, deposition of impurity and many more [23]. The emissivity of tungsten for example changes with both wavelength and surface temperature [23, 24]. The emissivity of tungsten varies in the range of 0.1 - 0.4 in dependence of the wavelength, thus making the measurement using IR thermography challenging. For the sensitivity study in this chapter only a wavelength dependent emissivity is assumed. The emissivity curves described by 2nd order polynomials are close to the real emissivity value of many materials with a metallic surface in IR spectral range [25, 26].

$$\varepsilon(\lambda) = a_0 + a_1 \cdot \lambda + a_2 \cdot \lambda^2 \tag{3.2}$$

Here a_0, a_1, a_2 are the prefactors of the polynomial function, λ is the wavelength. Using synthetic data the trend of the emissivity in dependence of the wavelength is investigated.

3.3. Planck's Law Model

Synthetic data for the spectrometer is generated to determine the dependence of the emissivity of tungsten on the wavelength and adding normally distributed noise, Γ_{noise}, which considers thermal and electronic noise, to equation 2.4:

$$\Gamma_{\text{spec}} = \varepsilon(\lambda) \cdot \Gamma_{\text{planck}} + \Gamma_{\text{noise}} \tag{3.3}$$

The Planck equation, 2.4 represent the model for a constant emissivity. Equation 2.4 is modified by multiplying a polynomial function of second order of the emissivity 3.2 :

$$\text{Model}_1 = \epsilon_{\text{const}} \cdot \frac{2\pi c}{\lambda^4} \cdot \frac{1}{\exp\left(\frac{hc}{\lambda k_B T}\right) - 1} \tag{3.4}$$

$$\text{Model}_2 = \epsilon(\lambda) \cdot \frac{2\pi c}{\lambda^4} \cdot \frac{1}{\exp\left(\frac{hc}{\lambda k_B T}\right) - 1} \tag{3.5}$$

The parameters of emissivity used to generate the synthetic data are chosen such that the emissivity matches that of tungsten ($a_0 = 0.7875, a_1 = -37500\ [\mathrm{m}^{-1}]\,,\ a_2 = -1 \cdot 10^{10}\ [\mathrm{m}^{-2}]$). The synthetic data is fitted using the two models. To have a statistically significant result, 1000 spectra are generated for a given surface temperature.

The surface temperature and the emissivity are evaluated by fitting the models (equations 3.4 and 3.5) to the synthetic data. Figure 3.4 shows the photon flux generated, for a surface temperature of 300 K and 1% noise level. The black dots represent the generated data, the red curve shows model$_1$ the Planck fit with a constant emissivity and the blue curve (which is not clearly seen due to the overlapping with the generated data) shows model$_2$ the polynomial Planck fit with a wavelength dependent emissivity function.

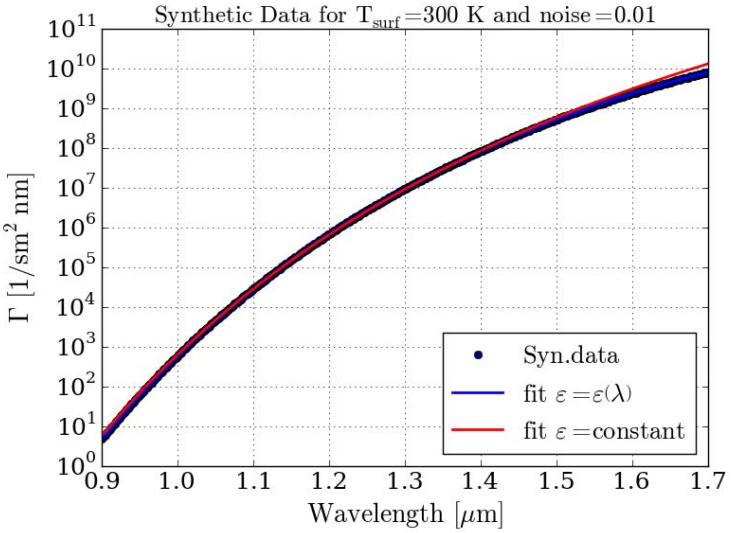

Figure 3.4.: Example of the synthetic data generated for a surface temperature of 300 K with the fit models.

From the fit using model$_1$, a constant emissivity and the surface temperature are evaluated. Using model$_2$ as fit gives the three prefactors (a_0, a_1, a_2) of the polynomial function and the surface temperature. From the prefactors the emissivity is then reproduced. The spectral range of the spectrometer is 0.9 - 1.7 μm with a resolution of 512 pixels. Therefore using the given wavelength and resolution, the spectra generated are adjusted to those expected from the spectrometer.

Figures 3.5 shows the synthetic data for different surface temperatures and different noise levels. Profiles at low (300 K) and high (1500 K) surface temperature are shown for noise levels of 1%, 5% and 10%. The synthetic data, represented by black dots, is fitted using model$_1$ (red) and model$_2$ (blue). The signal of the spectrum at high wavelength is reduced due to the wavelength dependent emissivity compare to a constant emissivity. The increasing scattering of the black dots represents the increasing noise level.

The surface temperature evaluated from both models is examined. Figure 3.6 shows the surface temperatures evaluated using both models. On the $x-$axis, the surface temperature used to generate the synthetic data is represented and the surface temperature evaluated using the respective models is represented on the $y-$axis. Figure 3.6 (a) shows

the temperatures obtained from the model with constant emissivity $model_1$ and figure 3.6 (b) represent the temperatures evaluated using the polynomial emissivity model $model_2$. In general, it is observed that the uncertainty, represented by the error bars, increases with increasing noise level and surface temperature. In figure 3.6 (a) it is seen that with increasing surface temperature and noise level the constant model overestimates the surface temperature. The constant emissivity evaluated using $model_1$ is 0.07 which is significantly lower than the original value given (0.4 - 0.1), hence the surface temperature is overestimated. If the emissivity in a measurement varies with the wavelength and is not considered, the assumption of a constant emissivity would results in an overestimation of the surface temperature. Figure 3.6 (b), shows that the surface temperatures evaluated using $model_2$ correspond to those initially used to generate the synthetic data. Therefore, the trend of the emissivity evaluated using $model_2$ is investigated.

The behaviour of the polynomial emissivity is plotted in dependence of the wavelength for different temperatures and noise levels, shown in figure 3.7 (a), (b) and (c). The black line represents the emissivity curve used to generate the synthetic data. The curve is calculated using equation 3.2. The figures are divided in three parts. The upper and lower dotted line show the upper limit and lower limit of the standard deviation respectively whereas the filled line in the middle show the actual emissivity calculated using the fitted parameters and wavelengths. The averaged emissivity reconstructed for each surface temperature is close to the emissivity used for the generation of the synthetic data. This observation is valid for increasing noise level in the synthetic data. It is observed that the reconstructed emissivity deviates from the original emissivity with increasing noise level. The upper and lower limits of the standard deviation, of the respective emissivities, also increases. It is seen that the emissivity reconstructed is more precise for longer wavelengths. The reason is that at longer wavelengths the photon flux is higher. Therefore, the signal to noise ratio is higher for longer wavelengths. Figure 3.7 (d) shows the relative error of the emissivity evaluated in dependence of the wavelength for 1% noise. It is observed that the relative error decreases with increasing wavelength. With increasing noise level the relative error increases. The relative error is scanned for a noise level up to 10%. The relative error for 10% noise level is about seven time higher than that evaluated for 1% noise level.

The behaviour of the emissivity in the spectral range of the spectrometer was investigated using synthetic data. It is seen that considering a constant emissivity model for data with a wavelength dependent emissivity results in a systematic error. This leads to an overestimation of the surface temperature as the emissivity is underestimated. From the results, it is seen that in the spectral range of the spectrometer, the emissivity calculated decreases with increasing wavelength and has been correctly reproduced. Thus, it is concluded that for the surface temperature evaluation the wavelength dependence of the emissivity has to be taken into account.

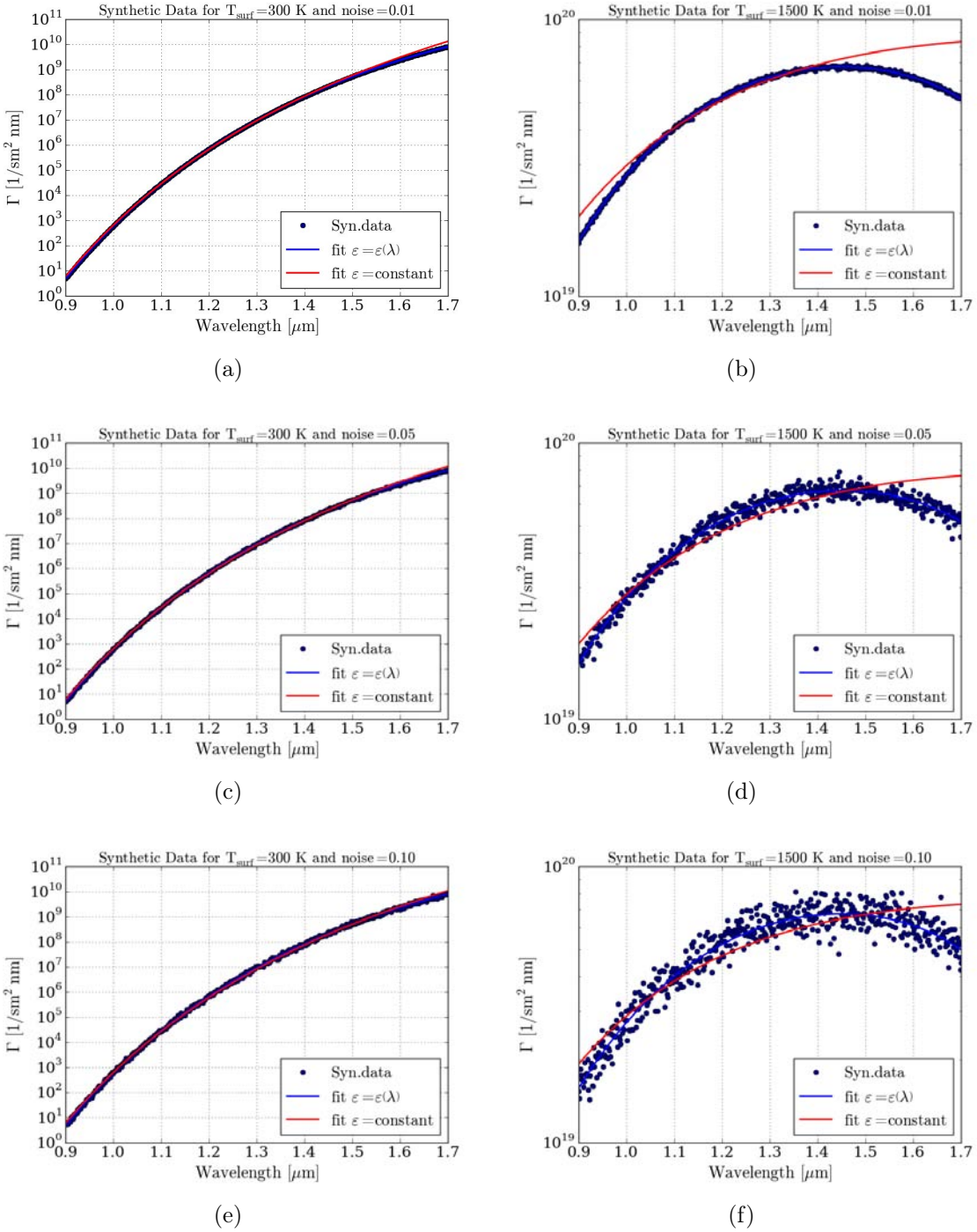

Figure 3.5.: Figure (a), (c) and (e) show the photon flux for data generated for a surface temperature of 300 K and figure (b), (d) and (f) shows the photon flux for a surface temperature of 1500 K, for 1 %, 5% and 10% noise level .

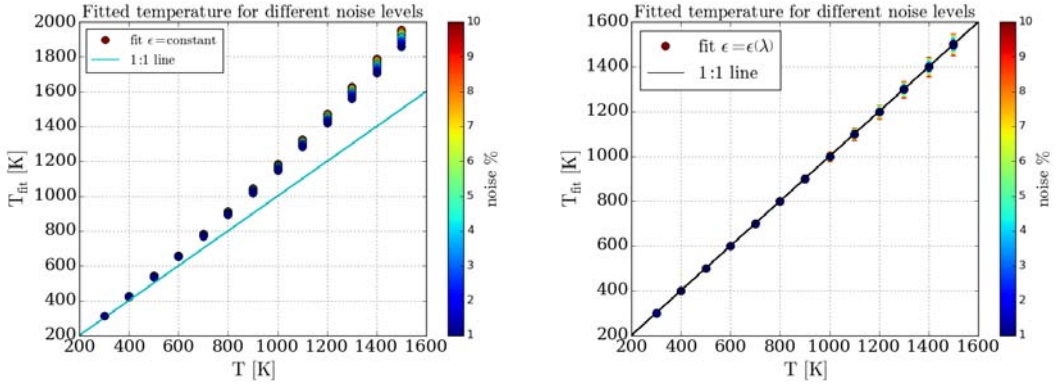

(a) (b)

Figure 3.6.: The figure shows the different temperatures fitted by the two different models for different noise level. (a) represent the results for model_1 and (b) shows the results using model_2 fit

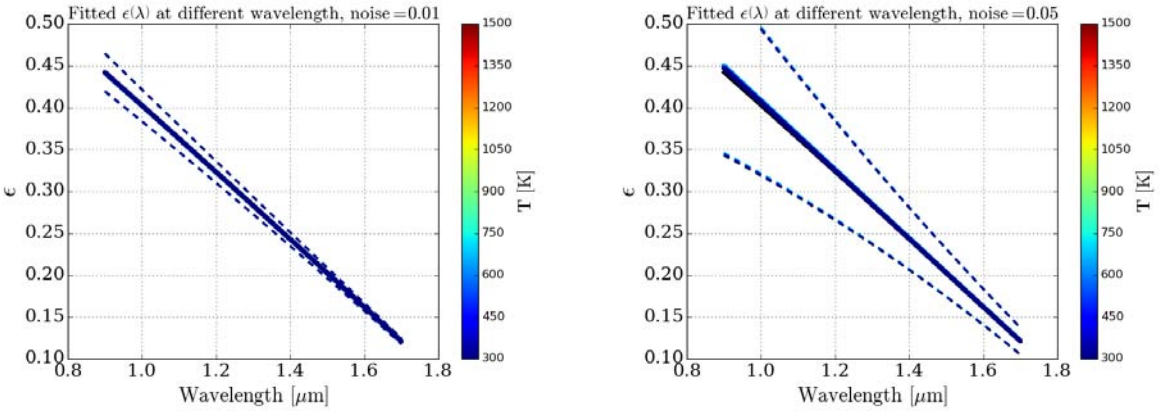

(a) Emissivity for 1% noise (b) Emissivity for 5% noise

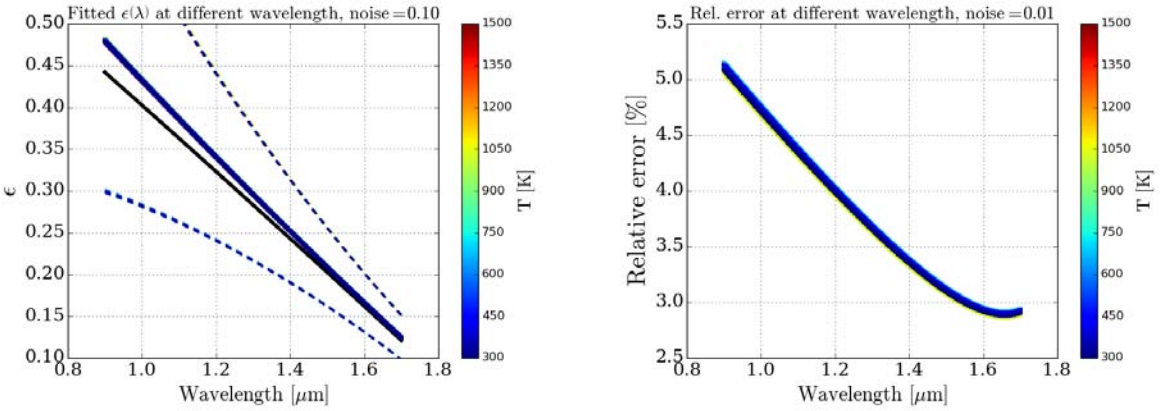

(c) Emissivity for 10% noise (d) Relative error for 1% noise

Figure 3.7.: Figure (a), (b), (c) show the behaviour of the emissivity at different temperatures for a noise level of 1%, 5% and 10% respectively and (d) shows the relative error of the emissivity for 1% noise level

3.4. Bremsstrahlung Model

In a tokamak, volume radiation like Bremsstrahlung can influence the measurement of the IR thermography. Therefore a study is carried out to understand how Bremsstrahlung influences the temperature measurement if it is not considered in the model. From the above study, it is now known that a wavelength dependent emissivity has to be taken into account. Synthetic data, taking thermal noise, electronic noise and a wavelength dependent emissivity into consideration, is generated for the spectrometer using equations 2.4 and 2.17:

$$\Gamma_{\text{spec}} = \varepsilon(\lambda) \cdot \Gamma_{\text{planck}} + b \cdot \Gamma_{\text{Bremsstrahlung}} + \Gamma_{\text{noise}} \tag{3.6}$$

$$\text{model}_3 = \varepsilon(\lambda) \cdot \Gamma_{\text{planck}} + b \cdot \Gamma_{\text{Bremsstrahlung}} \tag{3.7}$$

$$ratio = \frac{\int \varepsilon(\lambda) \cdot \Gamma_{planck} \cdot \mathrm{d}\lambda}{\int \varepsilon(\lambda) \cdot \Gamma_{planck} + b \cdot \Gamma_{\text{Bremsstrahlung}} \cdot \mathrm{d}\lambda} \tag{3.8}$$

$$b = \int \frac{\varepsilon(\lambda) \cdot \Gamma_{\text{Planck}}}{\Gamma_{\text{Bremsstrahlung}}} \cdot \left(\frac{1}{\text{ratio}} - 1\right) \cdot \mathrm{d}\lambda \tag{3.9}$$

where λ is the wavelength, T is the surface temperature, ε is the emissivity of the

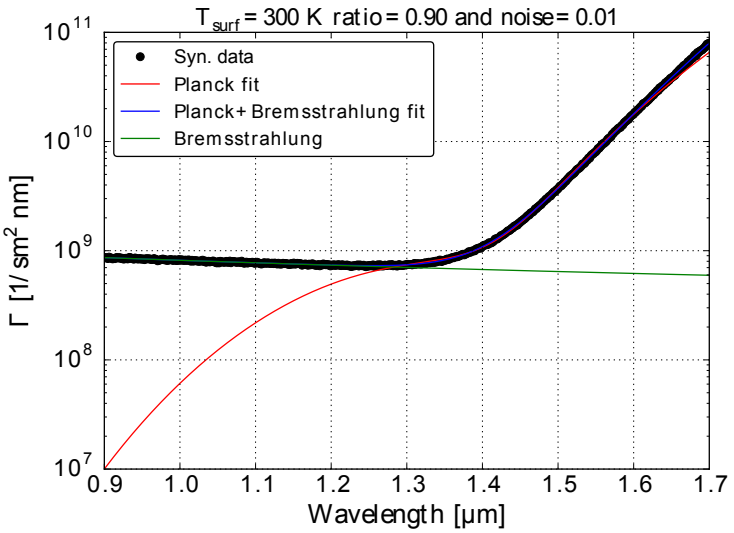

Figure 3.8.: Example of the synthetic data generated for a surface temperature of 300 K with 10% Bremsstrahlung and 1 % noise level.

surface and prefactor b, which is obtained by rearranging equation 3.8, gives the ratio of photon flux of black body radiation to Bremsstrahlung. For $b = 0.9$, 90% of black body radiation is present in the synthetic data and for $b = 0.1$, only 10% of black body radiation contributes to the generated data. For a given temperature the contribution of the black body radiation is kept constant, only the contribution of Bremsstrahlung (prefactor b) is varied. Equation 3.7 is the fit model which takes Planck's law with the

wavelength dependent emissivity (equation 2.4) and Bremsstrahlung (equation 2.17) into consideration.

Again 1000 spectra are generated to get statistically significant results. The parameters evaluated using model_2, gives the three prefactors of the polynomial emissivity function and the surface temperature. Since Bremsstrahlung is taken into consideration, additional parameters have to be considered, namely the prefactor b, the electron temperature T_e and the electron density n_e. The photon flux for Bremsstrahlung is calculated for an electron temperature of 10 eV and electron density of $1.0 \cdot 10^{19}\,\text{m}^{-3}$. To optimize the fit parameters of model_3 $(a_0, a_1, a_2, T, b, T_e, n_e)$ more efficiently, the polynomial function of the emissivity is rewritten as follows:

$$\epsilon(\lambda) = 10^{a_0} \cdot \left(1 + a_1^{'} \cdot \lambda + a_2^{'} \cdot \lambda^2\right) \tag{3.10}$$

Figure 3.8 shows an example of the synthetic data generated for a surface temperature of 300 K with 10% Bremsstrahlung contribution and a noise level of 1%. The resulting synthetic data (plotted in black dots) is the sum of Bremsstrahlung and Planck equation, Γ_{spec}. The green curve is the Bremsstrahlung contribution to the synthetic data and the blue curve (not visible due to overlapping with synthetic data) represent the fit for model_3 consisting of both Planck's equation and Bremsstrahlung. The red curve shows the fit for the model using Planck's law and considering a wavelength dependent emissivity, model_2. Figures 3.9 and 3.10 show the profiles at low and high temperature for a noise level of 1% and 5% respectively. Figure 3.9 shows the data for different ratios (between black body radiation and Bremsstrahlung) and surface temperature for 1% noise level. As seen in figure 3.9, the contribution of Bremsstrahlung at low surface temperatures (300 K) and short wavelength is dominant compared to high surface temperatures (1500 K). At high temperatures for 1% noise level the contribution of Bremsstrahlung is negligible for both ratio of 0.9 and ratio of 0.5. Taking figure 3.9 (a) and (c), it is seen that the photon flux increases with increasing contribution of Bremsstrahlung, i.e decreasing ratio. In figure 3.9, it is observed that model_2 (red curve) does not fit the data at low temperatures. Please note that sometimes model_2 fails to describe the synthetic data for short wavelengths and sometimes for long wavelengths, which is due to the internal algorithm of the fitting function used in python (computer language). The finding above holds also for different ratios, temperature and a noise level of 5% which is shown in figure 3.10. Due to the addition of Bremsstrahlung in the synthetic data, the model using only Planck's law with the wavelength dependent emissivity (model_2) predicts a higher temperature. Since the Bremsstrahlung flux has a descending slope as seen in figure 2.5 , which is added to the Planck equation with an ascending slope (figure 2.1), the data takes the form as shown in figure 3.9 (a) and (c). By fitting the data with a descending slope at small wavelengths and higher photon flux, the surface temperature is overestimated. This is because model_2 tries to fit the descending slope of a Planck's curve which describe higher surface temperatures at the given wavelength, see figure 2.1.

Figure 3.11 shows the surface temperature calculated for a ratio of 0.9 and an increasing noise level up to 5%. Figure 3.11 (a) and (c) shows the surface temperature evaluated using model_2. It is observe that the surface temperatures are overestimated significantly. The curve of model_2 appears to reproduce the synthetic data at high temperatures (figure 3.9 (b) and (d)) but still the surface temperature evaluated is significantly high. To be

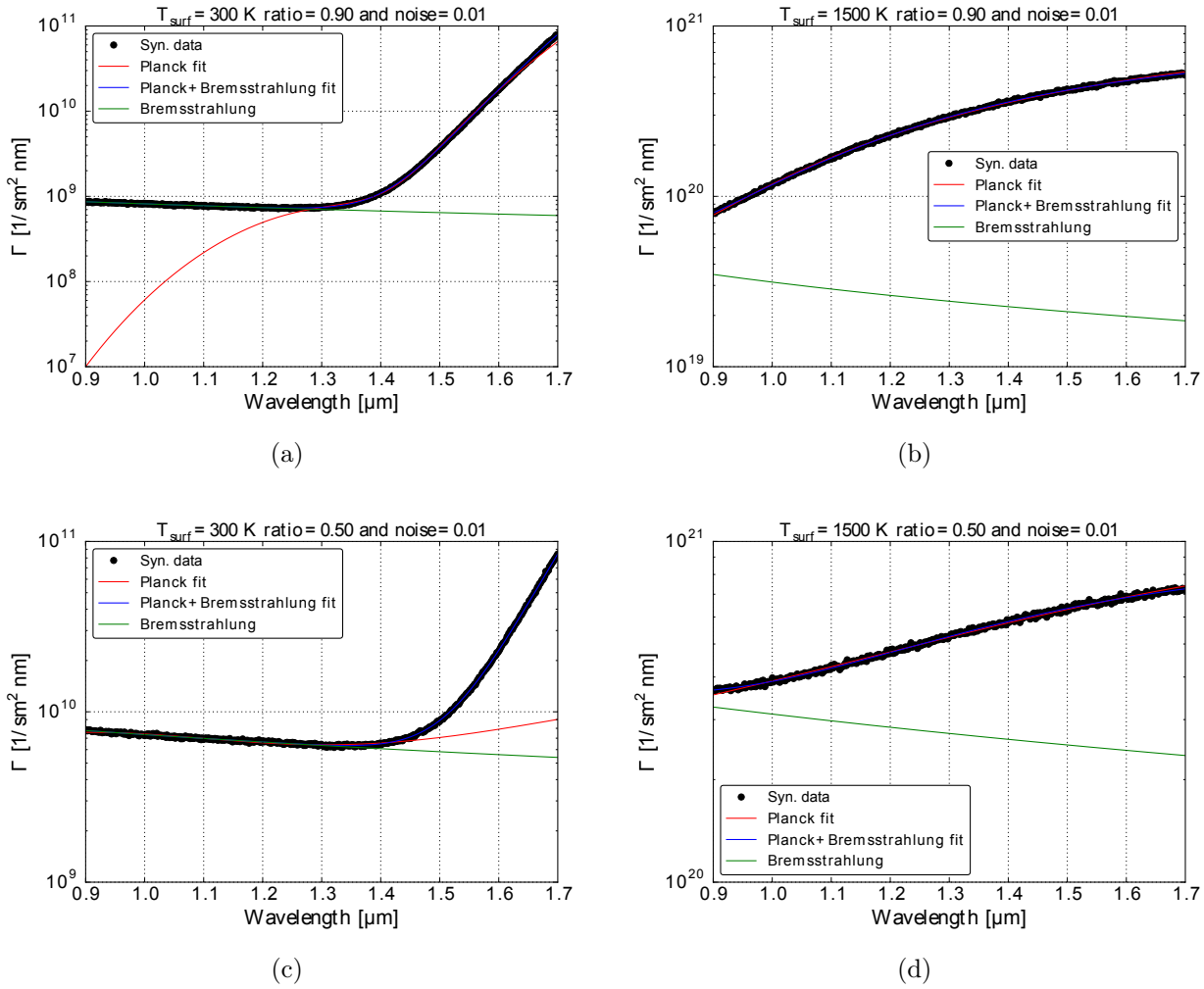

Figure 3.9.: Figure (a) - (d) show the spectrum of a surface temperature of 300 K and 1500 K respectively with 10% and 50% Bremsstrahlung contribution in the synthetic data for 1% noise level.

able to reproduce the shape of the spectra, the emissivity is underestimated for model$_2$ as shown in figure 3.12 (a) and (b). The underestimation of the emissivity also results in an overestimation of the surface temperatures. Note that due to the different notation of the emissivity function, the calculated emissivity is only relative (can be greater than one) and not absolute (between 0.4 - 0.1). The results of section 3.3 has shown that the emissivity decreases with increasing wavelength. The relative emissivity calculated is therefore assessed for this behaviour. This behaviour is also observed for the different ratios and increasing noise levels.

Figure 3.11 (b) shows the surface temperature evaluated for model$_3$ for a ratio of 0.9 and an increasing noise level up to 5%. It is observed that for 1% noise level, which corresponds to the noise level in the data of ASDEX Upgrade, the surface temperature is correctly evaluated. Interesting is that even for a ratio of 0.5 (3.11 (d)) , for 1% noise level a correct surface temperature is evaluated. As from 1100 K and for increasing noise levels, a systematic deviation is observed in the surface temperature evaluation. This behaviour

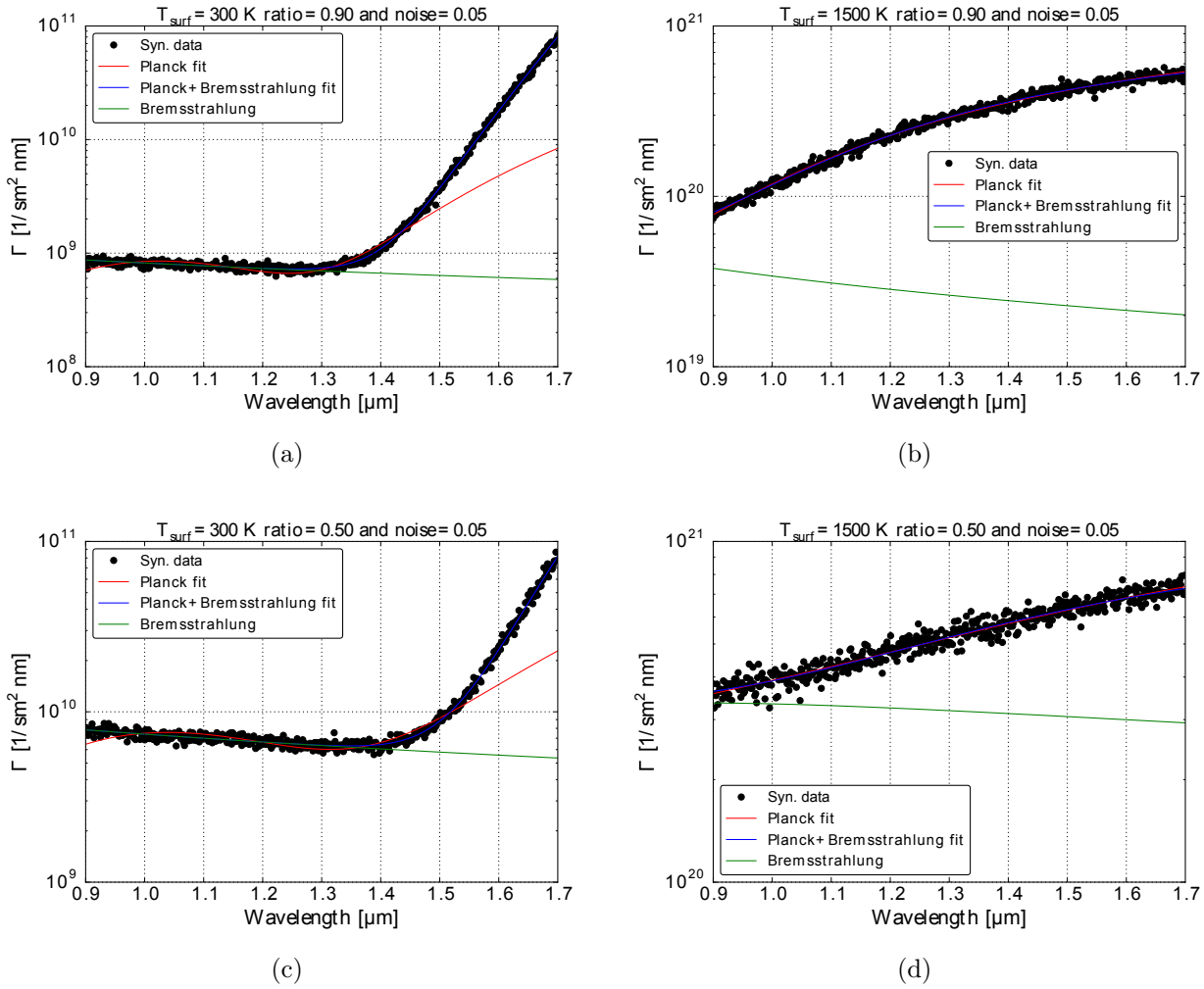

Figure 3.10.: Figure (a) - (d) show the spectrum for a surface temperature of 300 K and 1500 K respectively with 5% noise level with 10% and 50% Bremsstrahlung contributing to the synthetic data.

is also observed for a ratio of 0.5. Due to the polynomial function of the emissivity $\varepsilon(\lambda)$, the slope of the spectra become more shallow at high temperatures and with increasing noise levels. Therefore, it becomes difficult to disentangle Bremsstrahlung and black body radiation which then results in an underestimation of the surface temperature. Looking at the emissivity evaluated in figure 3.13 (b) it is observed that when the surface temperature is underestimated the emissivity is overestimated to reproduce the shape of the spectra.

In this section, the influence of Bremsstrahlung in the synthetic data was investigated. From the synthetic data, it was seen that at high surface temperatures the contribution of Bremsstrahlung is negligible. With Bremsstrahlung influencing the data, the evaluated surface temperature was overestimated when only Planck's law was considered. An overestimation of the surface temperature led to an underestimation of the emissivity. At the low noise level (1% noise corresponds to the noise level expected in ASDEX Upgrade measurements [27]) the surface temperatures evaluated using model$_3$ corresponds to that

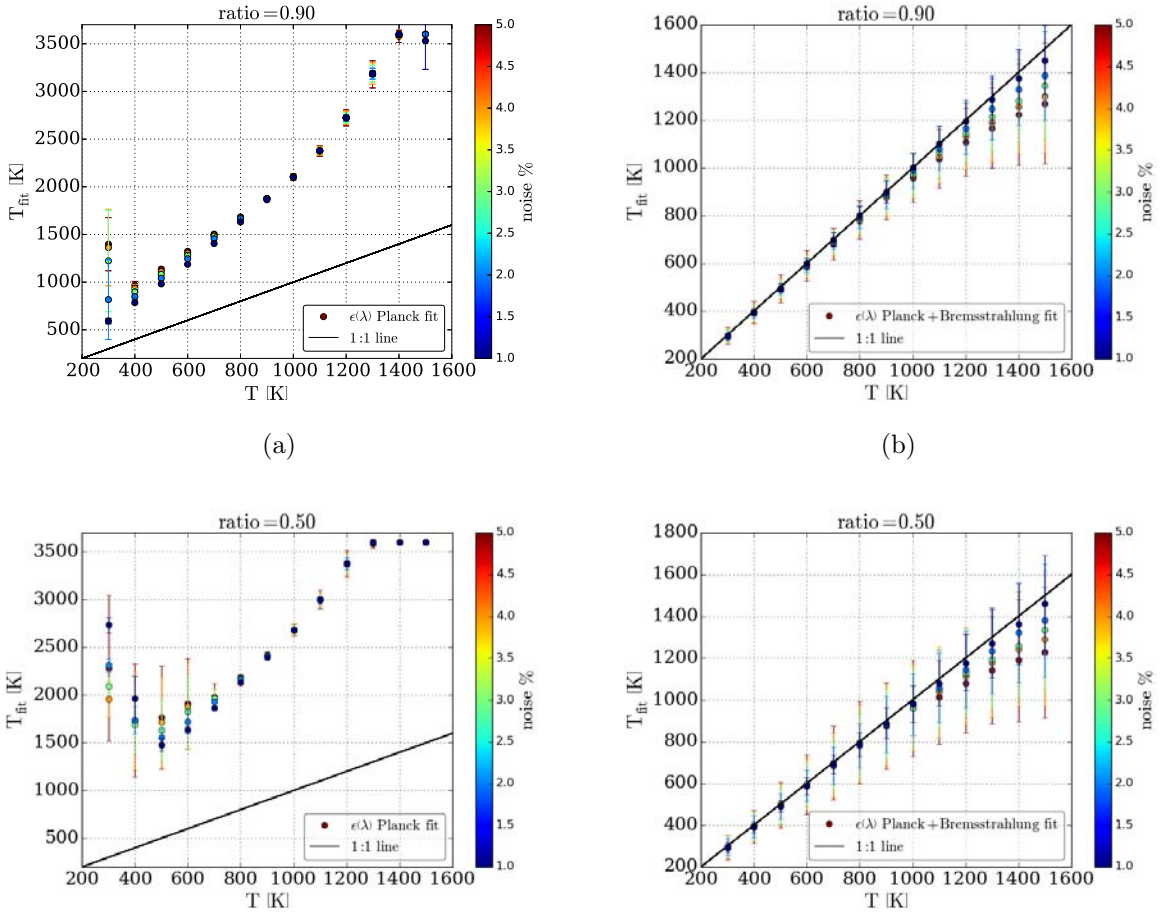

Figure 3.11.: The figure shows the surface temperature calculated using model_2 (left) and model_3 (right) for 1% up to 5% noise level. (a), (b) and (c), (d) represent the results for a ratio of 0.9 and 0.5 respectively.

initially used to generated the synthetic data. Thus, deducing that Bremsstrahlung needs to be considered in the model used for the temperature evaluation. In the same manner a wavelength dependent emissivity has to be used if the material parameters are unknown or else the temperature evaluation will be corrupted if the real emissivity is a function of the wavelength.

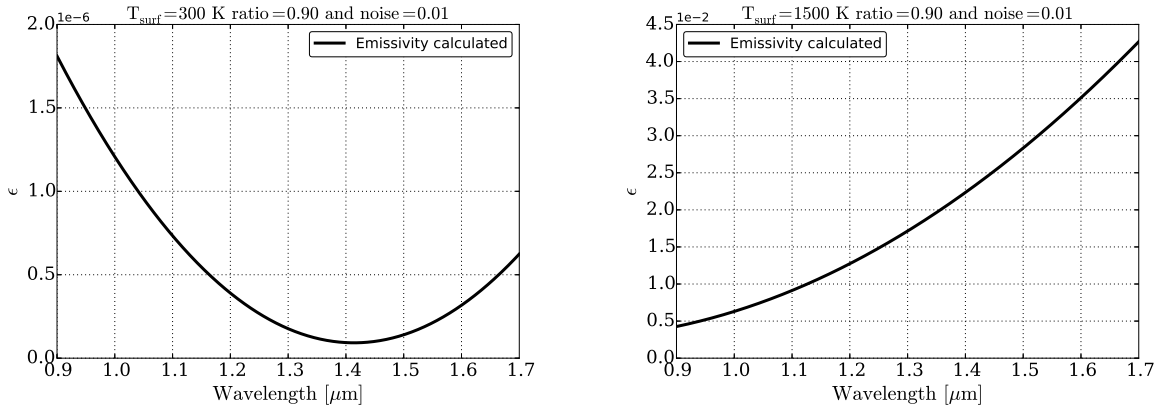

(a) (b)

Figure 3.12.: The figure shows the relative emissivity calculated using model$_2$ for 1% noise level. (a) and (b) represent the results for surface temperatures of 300 K and 1500 K respectively.

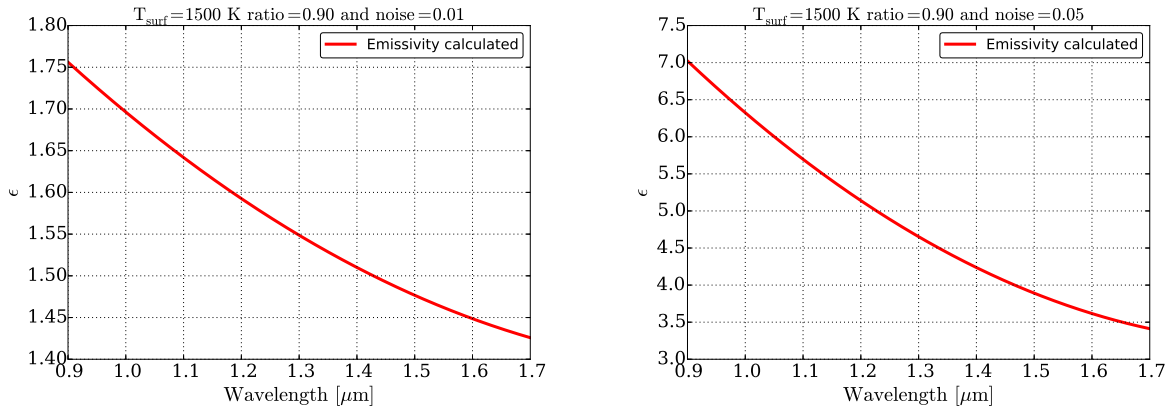

(a) 1% noise (b) 5% noise

Figure 3.13.: The figure shows the relative emissivity calculated using model$_3$ for 1% and 5% noise level and a ratio of 0.9.

4. Calibration

In the previous chapters the principle of IR thermography has been discussed. To apply these principles to real measurements further steps are required. The IR detectors are not ideal and therefore calibration of the system is mandatory. In this section the calibration of both integrating (e.g IR camera) and IR spectroscopic system is discussed.

4.1. Calibration of Integrating IR Systems

The IR detectors used for this thesis are CMOS (**C**omplemetary **M**etal **O**xide **S**emiconductors) based focal plane arrays (FPAs). In contrast to CCD sensors which have one read out logic for all the pixels, CMOS sensors have a read out logic for each pixel. This results in a nonuniform image. To obtain a uniform image, the so called gain and offset need to be accounted for. A method based on the integration time series can be used to calculate the gain and offset [28].

$$N_{digits} = a + b \cdot \Gamma \cdot \tau \tag{4.1}$$

$$\Gamma(\lambda) = \frac{2\pi c}{\lambda^4} \cdot \frac{1}{\exp\left(\frac{hc}{\lambda k_B T}\right) - 1} \, dA \, d\lambda \tag{4.2}$$

where N_{digits} is the number of counts measured by the sensor, a is the offset, b is defined as the gain, τ is the integration time used for the measurement and Γ is the photon flux.

The gain and offset have to be corrected for each pixel as they are all different. For the IR camera in ASDEX Upgrade, this correction has been performed by blocking the optical path of the detector with a uniform black body (e.g lens cap) and increasing the integration time step-wise. The number of counts measured is expected to be linearly proportional to the integration time. The offset and the gain values are determined by a linear regression between the counts and the integration time. Figure 4.1 shows that the gain and offset varies for every pixel. The individual gains are normalized to the median gain in order to obtain a uniform image while retaining the total response of the system. The offset is given by the Y-intercept.

The IR camera is calibrated using a black body with a known emissivity of 0.95 and the temperature is increased from 100 °C up to 1200 °C. The count rate for each temperature is measured. The relation between the count rate of a black body and photon flux is given by equation 2.1. Figure 4.2 shows that the count rate in dependence to the temperature of a black body for a wavelength of about 4.92 μm and an integrator with a capacity of $5.8 \cdot 10^6$ electrons [29]. It is observed that the count rate increases with increasing temperature and resolution of the detector. From the uniform image obtained, the surface temperature of the observed object can be determined as described in section 2.1.1.

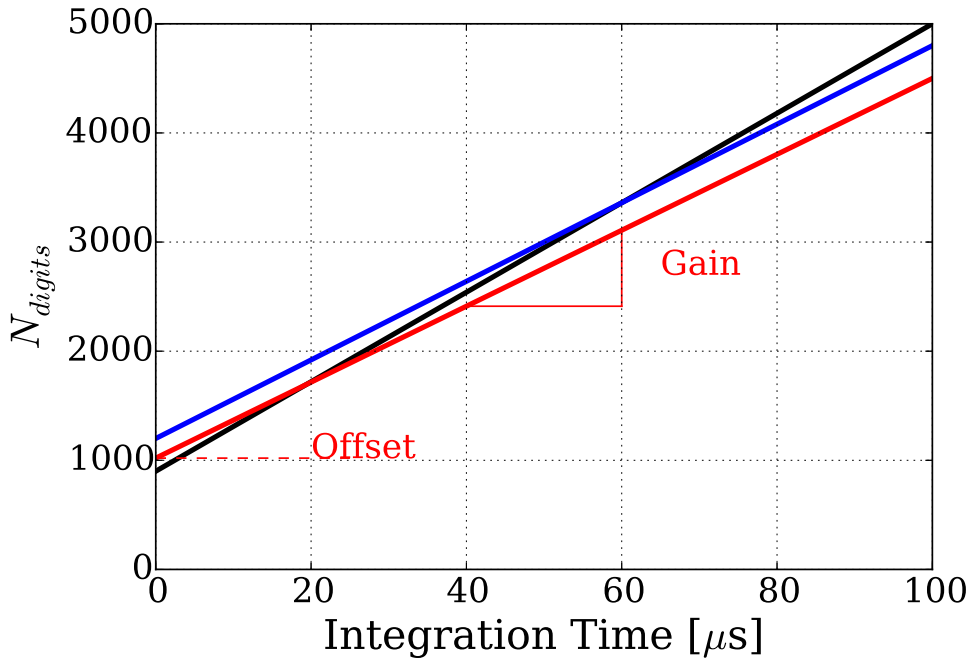

Figure 4.1.: The figure shows the variation of the gain and offset of some pixels.

4.2. Calibration of IR Spectrometer

The IR spectrometer has an InGaAs line array detector. The spectral response range of the spectrometer is $0.9 - 1.7\,\mu$m. The calibration of the IR spectrometer is more challenging compared to an integrating IR system. For an integrating IR system, the characterization of the detector and the temperature calibration can be done separately. For the IR spectrometer, the calibration of the detector and the measurement have to be carried out together as the illumination of the detector is not uniform. This is because the photon flux is a function of wavelength (for e.g the pixels) even for a constant temperature. The method used for the calibration is based on the integration time series. A black body is used for the calibration of the IR spectrometer. The emissivity of the black body is temperature independent and is assumed to be 0.95. The temperature of the black body is varied between 500 - 1200°C in steps of 100°C. For each temperature an integration time series from 10 μs up to 1 ms is acquired. For each integration time, 1000 spectra are acquired. The mean and standard deviation of each pixel is then calculated and results in an averaged spectrum for each combination of temperature and integration time.

The number of photons emitted is dependent on the temperature of the black body. The photons are diffracted by the grating of the spectrometer according to their wavelength. Each pixel observes only photons in a narrow wavelength interval. Since the calibration is done using a black body the photon emission is described by Planck's law:

$$\Gamma(\lambda, T) = \frac{2\pi c}{\lambda^4} \cdot \frac{1}{\exp\left(\frac{hc}{\lambda k_B T}\right) - 1} \, dA \, d\lambda \tag{4.3}$$

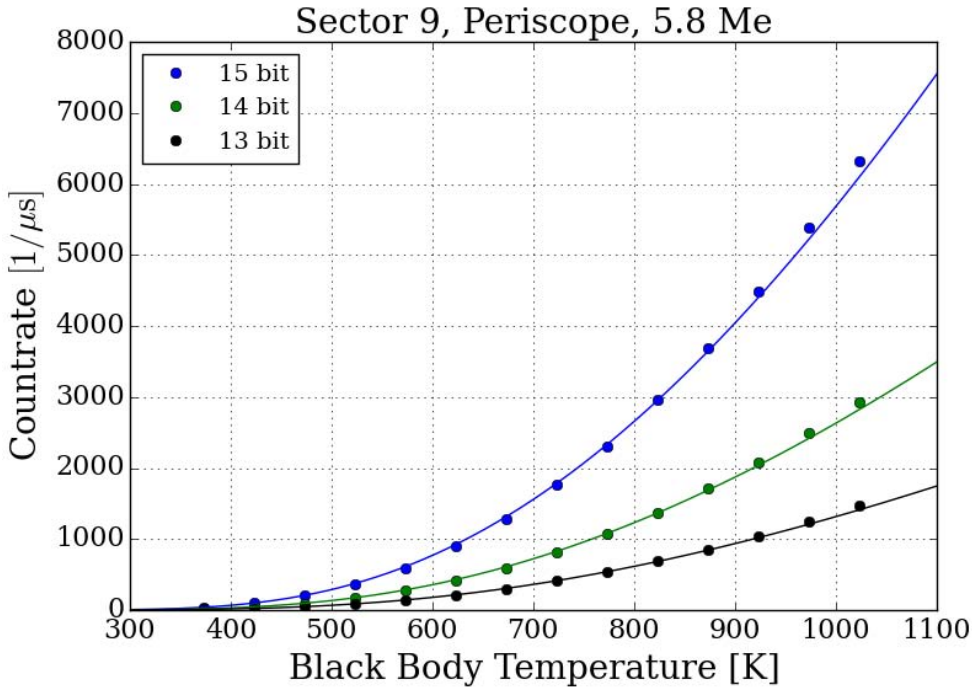

Figure 4.2.: The count rate in dependence of temperature for different detector resolution [29].

Using this, the model for photon rate D, for the photons arriving in the spectrometer is written as:

$$D = A_i \cdot \epsilon(T, \lambda) \cdot \Gamma(T, \lambda) \cdot \tau \tag{4.4}$$

$$A_i = a_i \cdot R(\lambda) \cdot dA \tag{4.5}$$

Where i is the index for the pixels, $R(\lambda)$ is the transmission coefficient of the system, dA is the solid angle for the calibration and a_i is the gain of each pixel. The spectrometer has a measurement offset due to thermal noise, electronic and readout noise for example. In addition each pixel has a different response to the incident photon flux, due to the different wavelength of the photons and possible variations in the production of the pixels. The following function is used to describe the measurements of the IR spectrometer, d_i:

$$\mathrm{d_i} = \mathrm{A_i} \cdot \epsilon(\mathrm{T}, \lambda) \cdot \Gamma(\mathrm{T}, \lambda) \cdot \tau + \sum_{\mathrm{j}=0}^{2} \mathrm{C_j} \cdot \tau^{\mathrm{i}} \tag{4.6}$$

where A_i is a parameter containing information about the transmission coefficient, linearity of the system and the gain of each pixel, $\Gamma(T, \lambda)$ is the photon flux (equation 4.3), τ is the integration time and C_i are the offsets. The parameters A_i, C_0,C_1 and C_2 are unknown, Bayesian statistics is used to infer the parameters based on the acquired data. For more details about Bayesian statistics please refer to appendix A.

Figure 4.3 (a) shows the uncalibrated spectrum for a black body temperature of 900° for different integration times. It is observed that the spectrum increases with increasing

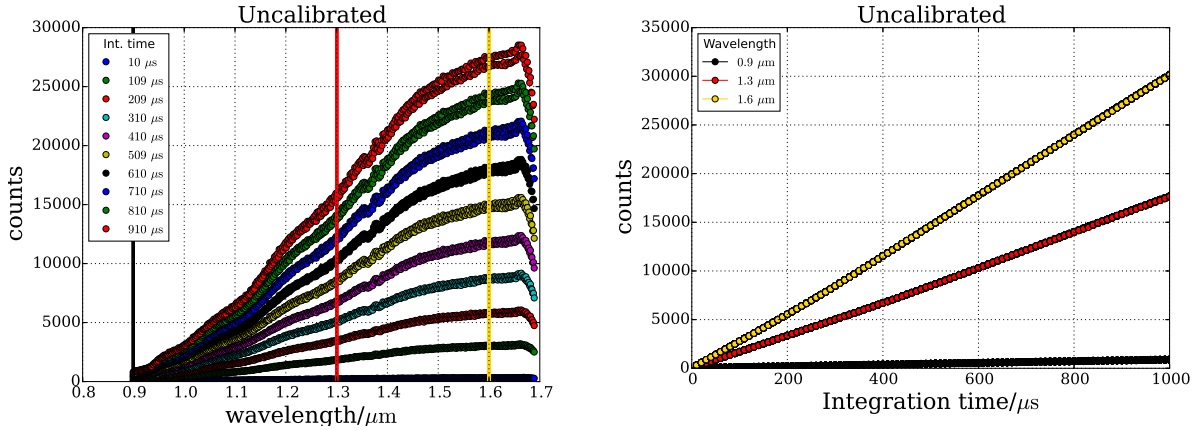

(a) Uncalibrated spectrum for 900°C

(b) Counts dependence on integration time.

Figure 4.3.: Figure (a) shows the spectrum obtained for different integration time (b) shows the linear dependence of counts on the integration time, i.e. the linear response of the detectors.

integration time. The double spectra observed is an artifact of the detector. The lines (black, red, yellow) marked in figure 4.3 (a) show, the wavelengths for which the measured counts is shown in figure 4.3 (b). It is observed that the number of counts measured for each wavelength increases linearly with the integration time but the gain of each wavelength is different.

Figure 4.4 (a) shows the average spectrum for different temperatures of a black body and figure 4.4 (b) (c) and (d) show the calibrated photon flux for a constant, first order and second order integration time respectively (coefficient C_0, C_1 and C_2 are switched on respectively). In figure 4.4(a) the number of counts, as measured by the IR spectrometer, is plotted against the wavelength for different temperatures. It is observed that for higher temperature the peak of the curves shift to lower wavelengths. Using Planck's equation, the data is calibrated for all integration time series and the photon flux obtained can be seen in figure 4.4 (b), (c) and (d). It is seen that the noise level decreases for increasing temperatures. It is observed that at low temperatures (773-873 K) the theoretical curve (dashed) does not coincide with the measurement. It might be that for low brightness measurements, the level of image noise increases. The model has been tested for integration time of higher orders, up to τ^5. The higher orders can be neglected as they do not influence the measurement significantly. The data is analyzed using equation 4.6, but without taking C_2 into consideration. Even though the data obtained is noisy for small wavelength and low temperatures, the theoretical curve agrees with the measured photon flux for temperatures higher than 700°. The coefficient C_0 are assumed to be a constant resulting from dark current. Dark current is defined as the current registered without photon detection in the spectrometer. For the thesis, it is concluded that C_2 and integration time of higher orders can be neglected but not considering C_0 and C_1 could lead to significant inaccuracy in the measurement.

It has been shown that the slopes (in figure 4.3 (b)) which represent the gain of each pixel is different and varies with the integration time and temperature simultaneously. Therefore, the calibration of the detector and the measurement have to be performed

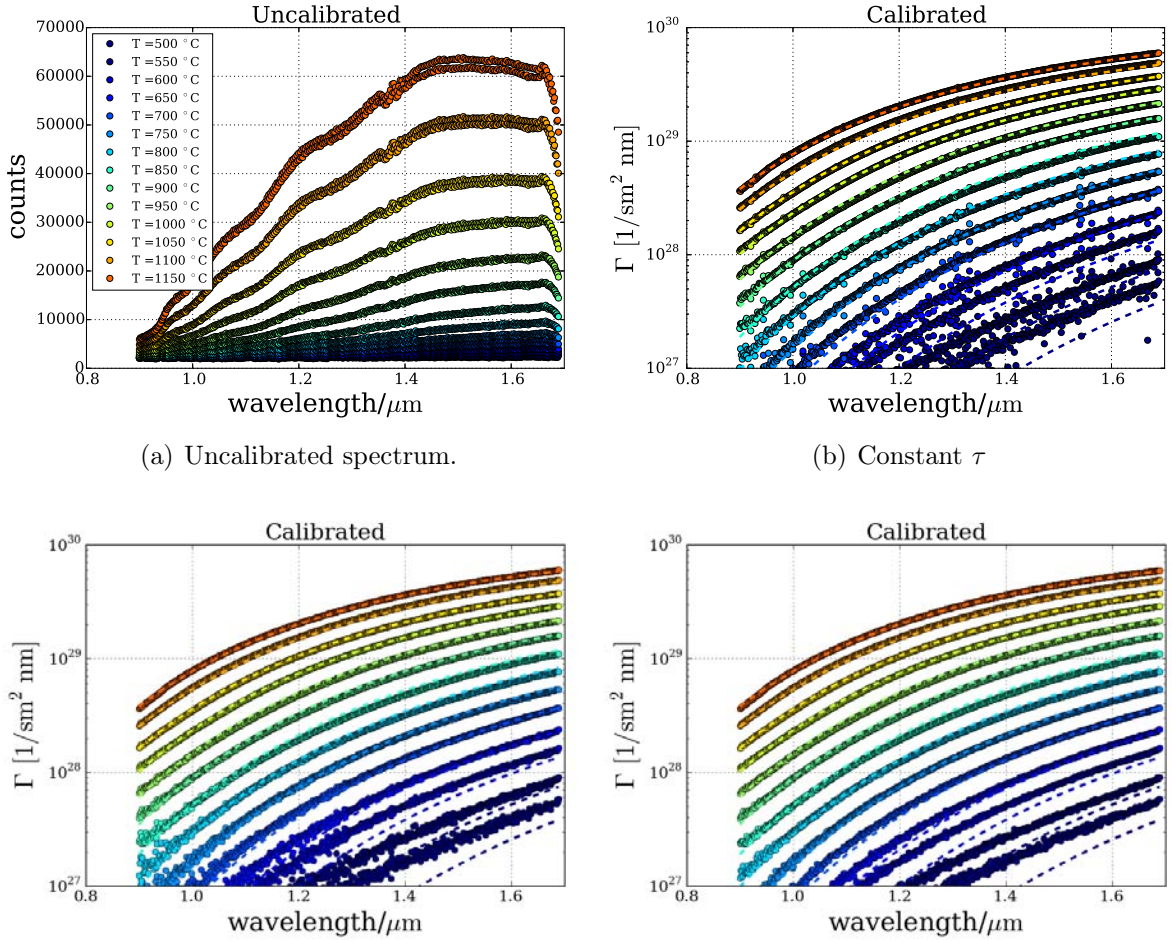

(a) Uncalibrated spectrum.

(b) Constant τ

(c) First order τ

(d) Second order τ

Figure 4.4.: Figure (a) shows the uncalibrated spectrum obtained and figure (b), (c) and (d) the photon flux of the calibrated data using Planck's fit for different offsets.

at the same time. This makes calibration of a spectroscopic IR system more complex compared to an integrating IR system. Using Bayesian statistics and combination of integration time series and a known black body at different temperature, the calibration has been achieved.

5. GLADIS

GLADIS (**G**arching **La**rge **Di**vertor **S**ample Test Facility) is a high heat flux (HHF) test facility, which is operated by the Max-Planck Institute for plasma physics in Garching. GLADIS is equipped with two individual 1.1 MW ion sources for testing of plasma facing components (PFC) under high heat flux, produce through ions, between 3 and 55 MW/m^2. Figure 5.1 shows the cylindrical vacuum chamber of GLADIS with a diameter and length of 1.5 m and 3.2 m respectively [30].

Figure 5.1.: An overview picture of HHF test facility GLADIS [30].

An experiment has been carried out to compare the surface temperature measurement of an IR spectrometer and a two color pyrometer. In addition thermocouples are used as a reference once the sample is thermalized. The GLADIS ion sources reproduce similar conditions as that of the neutral beam injector (NBI) system of ASDEX Upgrade in absence of plasma. Compared to ASDEX Upgrade NBI system, the ion sources in GLADIS do not have a neutralizer. Since there is no magnetic field in GLADIS, the ion beam is similar to the neutral beams in ASDEX Upgrade. The aim is to study the accuracy of the surface temperature measurement of the IR spectrometer.

5.1. Experimental Setup

Figure 5.2 shows the cross section of GLADIS. The water cooled vacuum chamber is equipped with two H^+ ion sources inclined to the horizontal axis of the facility. The target plane (1) is about 3 m from the ion sources. The IR spectrometer is mounted with an optical lens in front of a window such that the target plane is viewed.

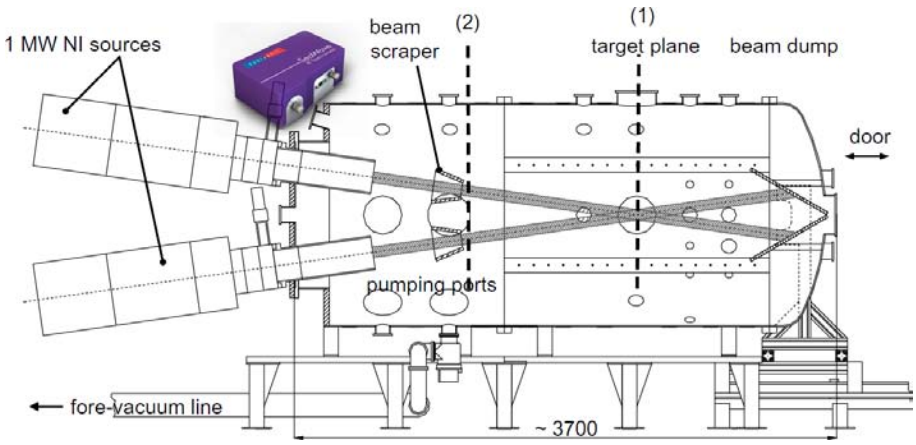

Figure 5.2.: The cross-section of HHF test facility GLADIS [30].

For the experiment only one NBI source has been used (top). As sample, a tungsten plug with a diameter of about 25 mm and a sand blazed surface, to increase the emissivity, is used. The bulk tungsten sample is mounted on a water cooled tungsten coated tile made of Carbon Fibre reinforced Composite (CFC). The sample itself is thermally only weakly contacted to the carrier to ensure an increase of the bulk temperature with each exposure. The surface temperature of a sample in GLADIS is routinely measured using a two color pyrometer. For the experiment a MAURER-digital IR two colors pyrometer, of the series QKTRD 1075, is used. The temperature measuring range is $500 - 1700\,°C$ and the spectral ranges are $1.4 - 1.75\,\mu m$ and $1.6 - 1.75\,\mu m$ [31]. The optic used for the pyrometer is of type A1080 with a measuring aperture of 0.5 mm. In addition, thermocouples are connected on the rear side of the sample which are used to determine the bulk temperature of the sample. The thermocouples used are type K and type N. Since the type K thermocouple measures only up to 1100°C, the type N thermocouple is used to measure higher temperatures. The maximum temperature measurement of type N thermocouple is up to 1260°C. The measurement of type K thermocouple can be used directly but that of type N is corrected as it is not calibrated for the system. A constant heat flux of $5\ \frac{MW}{m^2}$ is used for the experiment. The temporal evolution of the heat flux used for the operation at GLADIS has a rectangular shape. Solving the heat diffusion equation for a rectangular pulse gives a surface temperature rise proportional to the square root of the pulse duration [32]. Figure 5.3 shows the sample which is exposed to the heat flux. Figure 5.3(a) shows the sample before exposure to the heat flux. In figure 5.3(b), one can see the glowing bulk tungsten sample after the exposure to a beam pulse.

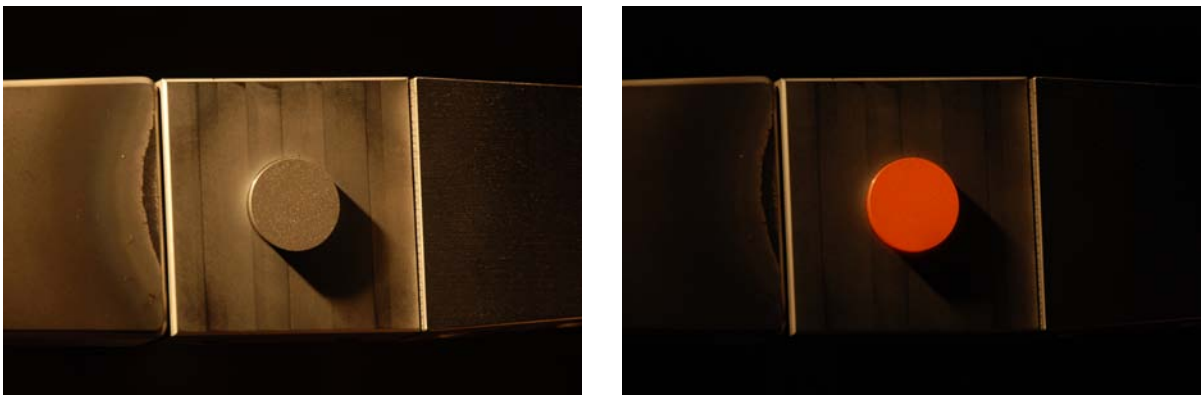

(a) Before HHF exposure (b) After HHF exposure

Figure 5.3.: Picture of the a tungsten plug (a) before exposure to heat flux and (b) after exposure

5.2. Models for Surface Temperature Evaluation

In this section different models are tested for the surface temperature evaluation of the IR spectrometer measurements.

The photon emission of an ideal black body is described by Planck's law:

$$\Gamma_{planck}(\lambda) = \varepsilon \frac{2\pi c}{\lambda^4} \cdot \frac{1}{\exp\left(\frac{hc}{\lambda k_B T}\right) - 1} \mathrm{d}A\mathrm{d}\lambda \qquad \left[\frac{1}{\mathrm{sm}^2\ \mathrm{nm}}\right] \tag{5.1}$$

The surface of the tungsten plug is not an ideal black body. The ratio of the surface emission to that of an ideal body is known as the emissivity ε. Refer to section 2.1.1 for more details. The emissivity of an ideal black body is one and that of the black body used to calibrate the IR spectrometer is 0.95. In contrast to the black body the emissivity of the plug's surface is unknown. The emissivity of tungsten can vary significantly depending on the surface conditions [24] . A polished surface has a lower emissivity compared to a sand blasted surface. In our case a sand blasted surface has been used. Since the emissivity of tungsten changes with wavelength and temperature [23, 24], a wavelength as well as a temperature dependent emissivity is used for the surface temperature evaluation. Since the emissivity is unknown, different emissivity models are considered for the evaluation:

$$\varepsilon_1 = \text{constant} \tag{5.2}$$
$$\varepsilon_2(\lambda) = a_0 \cdot ((1 + a_1 \cdot \lambda) \tag{5.3}$$
$$\varepsilon_3(\lambda) = a_0 \cdot ((1 + a_1 \cdot \lambda + a_2 \cdot \lambda^2)) \tag{5.4}$$
$$\varepsilon_4(\lambda, T) = a_0 \cdot ((1 + a_1 \cdot \lambda + a_2 \cdot \lambda^2) \cdot (1 + a_3 \cdot T)) \tag{5.5}$$
$$\varepsilon_5(\lambda, T) = a_0 \cdot ((1 + a_1 \cdot \lambda + a_2 \cdot \lambda^2) \cdot (1 + a_3 \cdot T + a_4 \cdot T^2)) \tag{5.6}$$

$$model_1 = \varepsilon_1 \cdot \Gamma_{planck} \tag{5.7}$$
$$model_2 = \varepsilon_2(\lambda) \cdot \Gamma_{planck} \tag{5.8}$$
$$model_3 = \varepsilon_3(\lambda) \cdot \Gamma_{planck} \tag{5.9}$$
$$model_4 = \varepsilon_4(\lambda, T) \cdot \Gamma_{planck} \tag{5.10}$$
$$model_5 = \varepsilon_5(\lambda, T) \cdot \Gamma_{planck} \tag{5.11}$$

where a_i are the fitting parameters.

5.3. Evaluation

In this section an overview of the surface temperature evaluated using the different models are given. The surface temperatures evaluated for the IR spectrometer are compared to the two color pyrometer and thermocouple measurement. The temperature and wavelength dependency of the emissivity is discussed and the heat flux is determined for each surface temperature evaluated and compared to that measured at GLADIS.

5.3.1. Overview

The surface temperature is determined by fitting the different models to the data of the IR spectrometer. No Bremsstrahlung is taken into account for the surface temperature evaluation since there is no plasma in GLADIS.

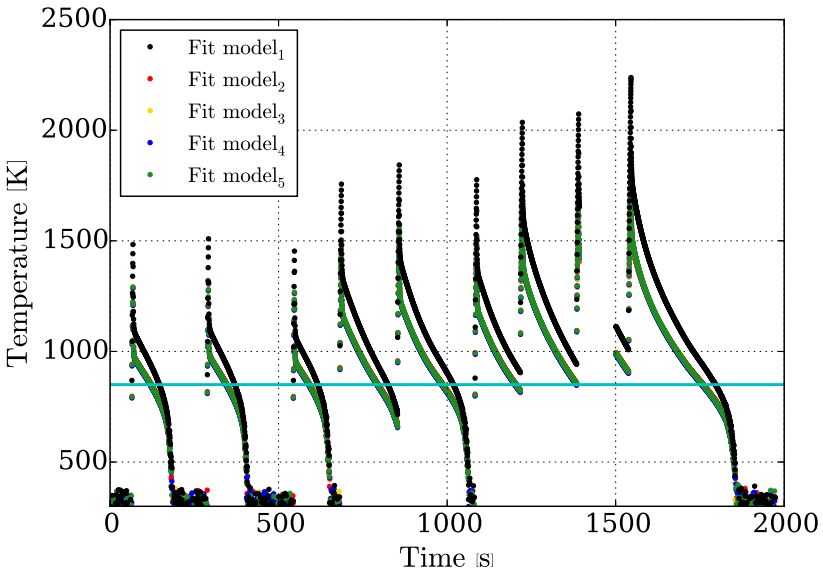

Figure 5.4.: GLADIS pulses as evaluated for the spectrometer.

The experiment is started with the tungsten plug at room temperature. The temperature of the tungsten plug is increased stepwise by several exposures of a moderate heat flux. Figure 5.4 show the surface temperature evolution of different pulses carried out in GLADIS. The surface temperature is determined using the different fit models, from the IR spectrometer measurement. In figure 5.4 only $model_1$ and $model_5$ are visible. The surface temperatures evaluated by $model_2$, $model_3$ and $model_4$ are overlapped by that evaluated using $model_5$ and are therefore not visible. In figure 5.4 at about 850 s, it is seen that the bulk temperature of the tungsten plug increases after several exposures to the heat flux. At about 1000 s, the plug is allowed to cool down. As from 1300 s, the plug is exposed to several heat flux exposures and since the time gaps between the experiments are small, the base temperature of the tungsten plug is again increased. From figure 5.4, it is also observed that at 300 K, the models fail to evaluate the surface temperature due to the low signal measured. This is deduced by the observation of the scattered points. Between 300 K and 700 K, no data points are measured due to the low signal to noise ratio. Therefore, a lower detection limit of 850 K (cyan line) is assumed for the spectrometer in GLADIS.

5.3.2. Single Pulse

Figure 5.5 shows the surface temperature evolution for the third pulse in figure 5.4.

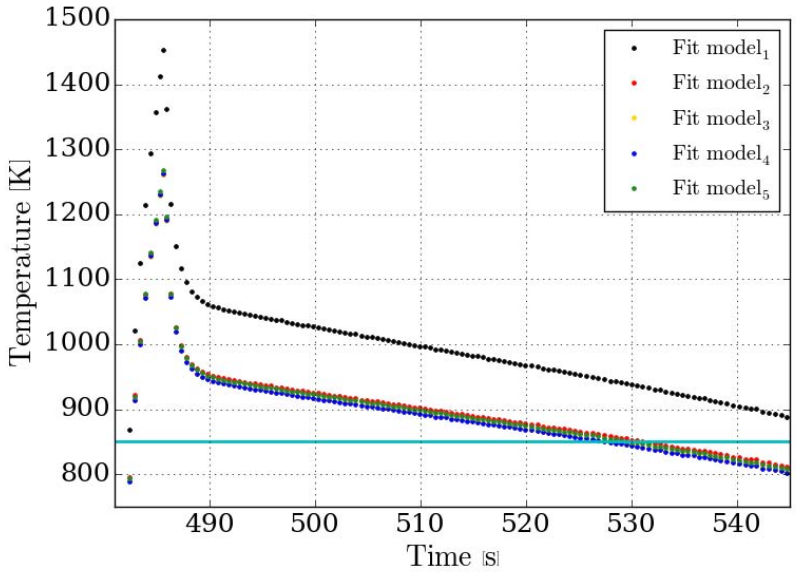

Figure 5.5.: Third GLADIS pulse as evaluated for the spectrometer.

The cyan line indicates the lower detection limit of the spectrometer. The black curve represents the surface temperature evaluated using a constant emissivity. The surface temperatures as evaluated using the models considering a wavelength or wavelength and temperature dependent emissivity do not vary significantly. A sharp increase of the surface temperature is observed at the beginning of the pulse as the tungsten plug is exposed to the heat flux. The surface temperature decreases instantaneously when the neutral

beam is switched off, thus indicating fast cooling of the surface. Since the surface of the plug is hot and the plug's bulk temperature low, the heat diffuses into the bulk which explains the fast cooling. After about 15 s it is observed that the surface temperature decreases slowly. This is because the bulk of the plug has reached a homogeneous temperature distribution. The slow cooling is a result of heat loss due to radiation and heat transfer to the cooled carrier structure.

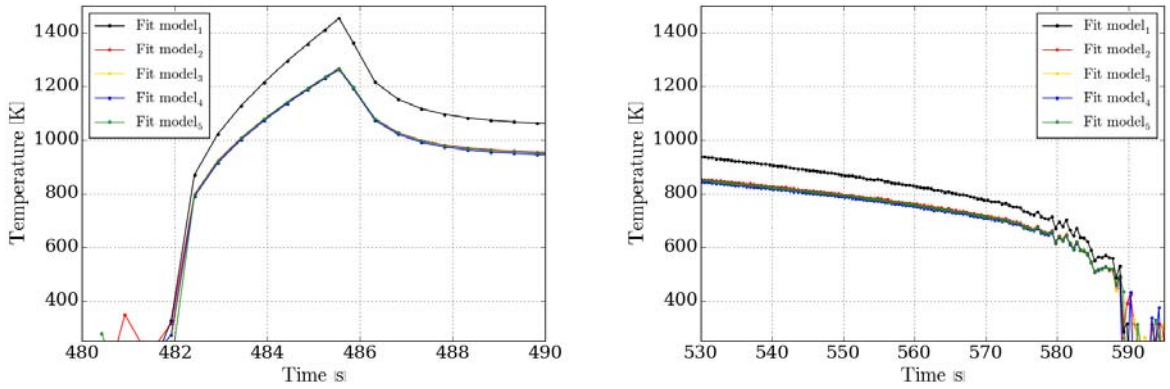

(a) (b)

Figure 5.6.: Temperature evolution of a GLADIS pulse (a) at the beginning and (b) the cooling curve after the pulse.

Figure 5.6 (a) shows the start of the pulse in figure 5.5. The NBI is switched on at about 482 s and switched off at 485.8 s, resulting in a pulse duration of about 3.8 s. The surface temperature at the beginning of the pulse should increase proportionally to the square root of time, further discussion is in section 5.3.5. Figure 5.6 (b) shows part of the cooling curve of the plug's surface when the equilibrium is reached, thus showing the slow cooling of the plug.

5.3.3. Comparison to Two Color Pyrometer and Thermocouples

Figure 5.7 shows the temperature profile of the pulses in GLADIS as evaluated for the pyrometer (shown in magenta), the thermocouple type N (shown in cyan) and that of thermocouple type K (shown in salmon). Around 15 s, after the NBI is switched off, thermal equilibrium of the tungsten plug is reached.

Again, since the plug is isolated, it has a low heat conductance to the surrounding and therefore the temperature decreases slowly. In the first two pulses, the pyrometer has been readjusted so that the cooling curve is in agreement with the thermocouples. In the last two pulses, it is seen that the thermocouple K is saturated at about 1100°C as its temperature limit is reached. The thermocouple type N is able to measure up to 1260°C, which is seen in the last pulse of figure 5.7, where the thermocouple (cyan) saturates. In figure 5.8 (a) the temperature profiles of the four devices used during the experiment and the first pulse of figures 5.4 and 5.7 are shown. The evaluated temperature is plotted against the duration of the experiment. The surface temperature obtained for

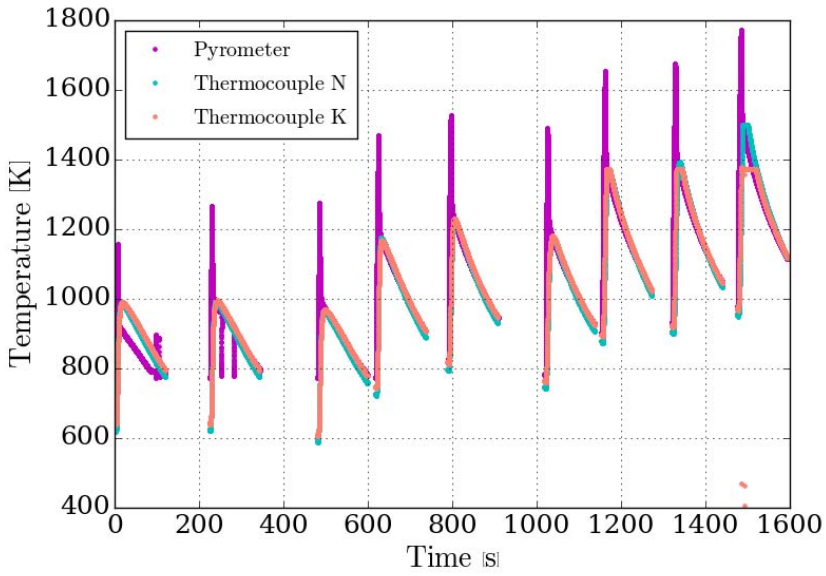

Figure 5.7.: Temperature measurements using the different devices used at GLADIS.

the pyrometer is shown in magenta. The bulk temperature evaluated for the tungsten plug using the thermocouple type N is marked in cyan and that of type K is shown in salmon. Figure 5.8 (b) shows a zoom into figure 5.8 (a). It is seen that the pulse duration is about 4 s, starting at about 482 s and ending at about 486 s.

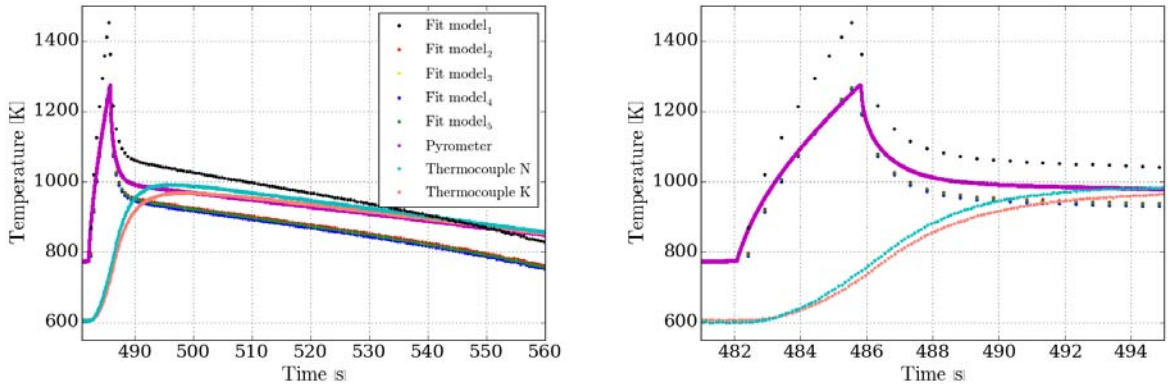

(a) (b)

Figure 5.8.: Figure (a) shows the temperature profile of a pulse in GLADIS and figure (b) the zoom in of Pulse (a).

At the beginning of the pulse the surface temperature increases with the square root of time. The temperature falls instantly after the peak because at that point the NBI is shut down and as expected the surface temperature decreases instantly and then slowly. The two color pyrometer is calibrated such that, when the plug is in equilibrium the cooling curve of the pyrometer follows that of the thermocouples. In figure 5.8 (b), it is observed that the surface temperature evaluated by assuming a constant emissivity

(fit model_1) is significantly overestimated compared to the surface temperature measured by the pyrometer. The surface temperature evaluated for the spectrometer, including a wavelength dependent emissivity, is close to the surface temperature measured by the pyrometers.

In figure 5.9 the surface temperature between 482 s and 535 s for pyrometer ($\text{Temperature}_{\text{Pyro}}$) is plotted against those evaluated for the IR spectrometer with the different fit models ($\text{Temperature}_{\text{Fit}}$). It is observed that the temperature evaluated using a constant emissivity overestimates the surface temperature from the beginning of the pulse whereas taking at least a wavelength dependent emissivity, the surface temperatures measured by both devices are the same at the beginning of the pulse (1:1 line). As seen in the figure 5.9, when a thermal equilibrium is achieved the temperature evaluated using the different models, which includes wavelength as well as temperature dependent emissivity, underestimates the surface temperature.

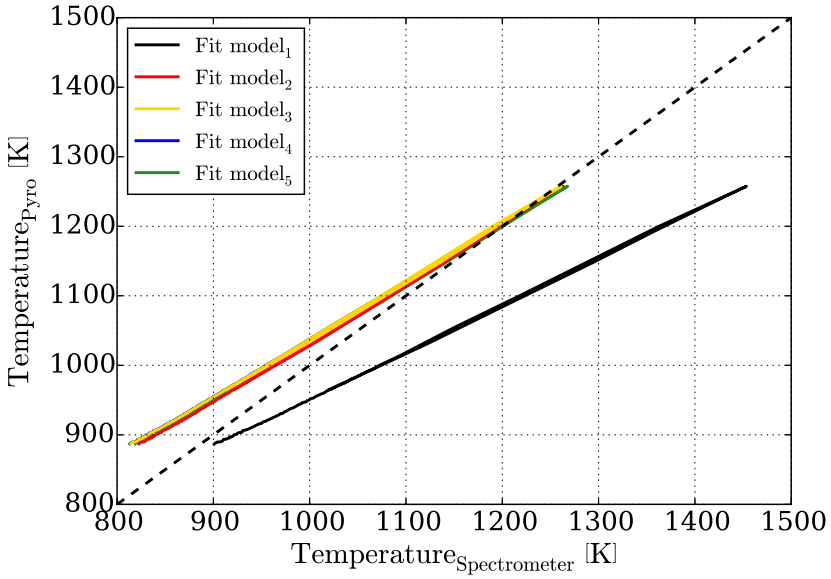

Figure 5.9.: The figure shows the temperature of the pyrometer in dependence to that of the spectrometer.

Figure 5.10 (a) shows the surface temperature measured during the cooling phase of the tungsten plug in dependence to the temperature measured by thermocouple type K. The decrease in the surface temperature indicates the cooling curve phase, for example the pyrometer cools down from 950 K to about 850 K ($x-$axis). The temperature difference is defined as, $\text{Temperature}_{\text{difference}} = \text{Temperature}_{\text{Thermo,k}} - \text{Temperature}_{\text{spec}}$. For the pyrometer, it is observed that the temperature difference decreases during the cooling phase. Since model_1 overestimates the surface temperature, the temperature differences are partly negative.

To investigate the surface temperature discrepancy, the emissivity including temperature dependency is discussed in the next section.

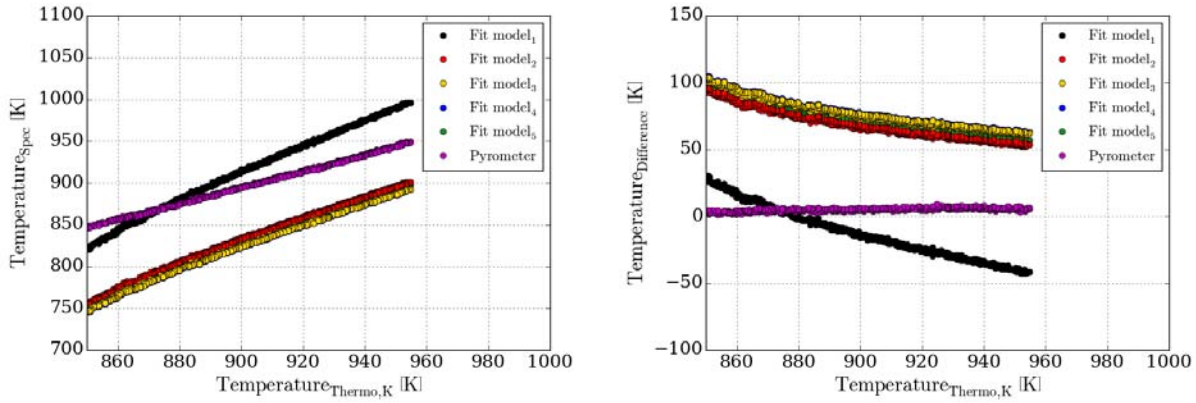

(a) (b)

Figure 5.10.: Figure (a) shows the temperature of the cooling curve as measured by the spectrometer in dependence to that of the pyrometer and figure (b) shows the temperature difference in dependence to that of thermocouple K.

5.3.4. Emissivity

The exact viewing angle of the spectrometer is unknown, therefore the absolute emissivity cannot be determined but relative emissivity. Figure 5.11 shows the relative emissivity calculated for model$_1$, model$_2$, model$_3$,model$_4$ in dependence of the wavelength. It is marked that the calculated relative emissivity, figure 5.11 (a), is in agreement with [24] (shows that the emissivity of tungsten decreases with increasing wavelength). Figure 5.11 (b) shows the temperature dependence of the relative emissivity calculated. The black color represents the relative emissivity calculated for a wavelength of 0.9 μm and in red the relative emissivity for 1.7 μm. In dotted lines, the relative emissivity using equation 5.5 is plotted and the solid lines represent the relative emissivity of equation 5.6. Comparing the relative emissivity of wavelength 0.9 μm to that of wavelength 1.7 μm, it is seen that the relative emissivity decreases with increasing temperature.

For the surface temperature measurement using the two color pyrometer in GLADIS, the ratio of the emissivities is assumed to be constant, $\frac{\epsilon_1}{\epsilon_2} = 1.06$. Since the two color pyrometer does not include a temperature dependent emissivity, it is likely the cause for the surface temperature discrepancy. From the study, it is deduced that the best model for the surface temperature evaluation would be model$_4$, where a linear temperature dependence of the emissivity is assumed.

5.3.5. Heat Flux Evaluation

The heat flux is evaluated from the temperature evaluated using the analytic solution of the semi infinite equation. The solution obtained analytically is valid only for the curve with rising temperature till the maximum of the temperature is achieved.

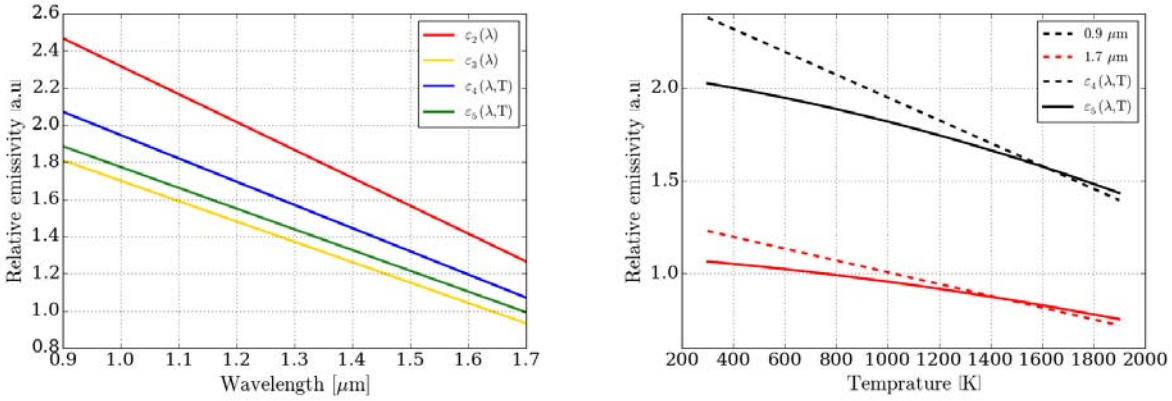

(a) relative emissivity in dependence to wavelength

(b) relative emissivity in dependence to temperature

Figure 5.11.: Figure (a) shows the relative emissivity calculated for the different fit models at 800 K (b) shows the temperature dependence of the relative emissivity.

The surface temperature is calculated as follows [33]:

$$\mathrm{T} = \frac{2}{\sqrt{\pi}} \cdot \frac{1}{\sqrt{\kappa \rho c_p}} \cdot q \cdot \sqrt{t} \tag{5.12}$$

where T is the surface temperature, κ is the thermal conductivity of the material and ρ is the density, c_p is the specific heat capacity of the material used q is the heat flux density and t is the given time. The heat flux during the experiment is known, the semi infinite solution is used to validate it. Using equation 5.12 the temperature evolution measured is fitted. The calculated heat flux density of the spectrometer and pyrometer is compared to the exact values of the heat flux density used during the experiment. A heat flux of 5 $\frac{\mathrm{MW}}{\mathrm{m}^2}$ is set for the experiments.

The heat flux distribution of the beam in GLADIS is measured at the target plane with an inertially cooled copper calorimeter. The calorimeter is composed by 34 thermally insulated copper plugs which are separated by a distance of 15 - 30 mm. The local heat flux is evaluated from the temperature rise of each copper plug. The temperature rise of the plugs are measured by thermocouples in the thermal equilibrium after the neutral beam is switched off. A Gaussian fit to the evaluated heat flux provides the beam profile [30]. Figure 5.12 shows the heat flux distribution measured on the target. From the profile obtained, it is seen that the spot size of the beam at the target plane is about 180 mm. The calculated heat flux of each pulse and for each model used to evaluate the surface temperature are listed in table 5.1.

Comparing the results in table 5.1, it is seen that the heat flux calculated for the pyrometer is slightly higher than 5 $\frac{\mathrm{MW}}{\mathrm{m}^2}$ and that for model_1 is significantly overestimated. Please note that pulse 1 is used to adjust the two color pyrometer and has therefore no usable data. The overestimation of the heat flux calculated using model_1 is a result of the overestimated surface temperature. Considering the results obtained for model_2, model_3, model_4 and model_5, it is seen that the heat flux calculated is between 6 and 7 $\frac{\mathrm{MW}}{\mathrm{m}^2}$. If the emissivity is too low, the surface temperature is overestimated. The overestimation

Pulse	**1**	**2**	**3**	**4**	**5**	**6**	**7**	**8**	**9**
$\mathbf{Model_1}$ $\left[\frac{\mathrm{MW}}{\mathrm{m}^2}\right]$	8.57	9.67	9.30	8.74	8.26	8.44	8.52	8.47	8.67
$\mathbf{Model_2}$ $\left[\frac{\mathrm{MW}}{\mathrm{m}^2}\right]$	6.67	7.60	7.32	6.50	6.06	6.23	6.08	5.97	5.98
$\mathbf{Model_3}$ $\left[\frac{\mathrm{MW}}{\mathrm{m}^2}\right]$	6.83	7.75	7.46	6.82	6.41	6.57	6.57	6.51	6.66
$\mathbf{Model_4}$ $\left[\frac{\mathrm{MW}}{\mathrm{m}^2}\right]$	6.89	7.80	7.52	6.93	6.55	6.69	6.75	6.72	6.94
$\mathbf{Model_5}$ $\left[\frac{\mathrm{MW}}{\mathrm{m}^2}\right]$	6.87	7.79	7.50	6.86	6.46	6.61	6.63	6.58	6.76
Pyrometer $\left[\frac{\mathrm{MW}}{\mathrm{m}^2}\right]$	-	6.36	6.03	5.75	5.43	5.56	5.46	5.22	5.14

Table 5.1.: In the table the calculated heat flux using the surface temperature evaluated for each model and the pyrometer are listed.

of the surface temperature could results in a higher heat flux. For pulse 2 and pulse 3, the ratio of the emissivity is changed to 1.04 and 1.03 respectively. The emissivity is changed manually so that the temperature measured by the two colors pyrometer and the thermocouples are in agreement when thermal equilibrium is achieved. The emissivity correction for these two pulses would explain the heat flux obtained for the pyrometers. Also, the slight overestimation of the heat flux would imply that the emissivity ratio is not necessarily constant. It could be that the emissivity has a temperature dependence which is not taken into account in the temperature evaluation of the pyrometer in GLADIS.

5.4. Summary

The IR spectroscopic measurement has been tested in GLADIS. Using different models, which include wavelength and temperature dependency of the emissivity, the surface temperature is evaluated. The surface temperature has been validated against the thermocouples and the two color pyrometers. The results show that the IR spectrometer is able to detect the sharp temperature increase of each pulse. From the temperature discrepancy observed, it is deduced that for the surface temperature evaluation using the spectrometer, a temperature dependent emissivity has to be considered. Taking a constant emissivity, leads to an overestimation of the surface temperature. The experiment has been carried out without prior knowledge of the emissivity. Thus, showing that no prior knowledge of absolute or relative emissivity is required for the temperature evaluation using IR spectroscopy.

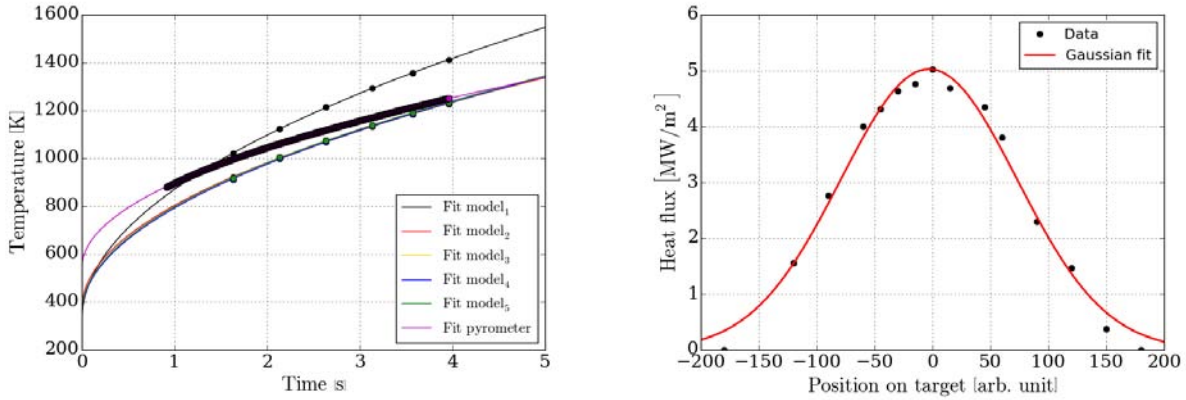

(a) Heat flux of pulse 3

(b) Heat flux distribution

Figure 5.12.: Figure (a) shows the fit to determine the heat flux of each model and that of the pyrometer and figure (b) shows the gaussian fit to the measured beam profile [30].

6. Experiments in ASDEX Upgrade

In this chapter the calibration of the spectrometer for the experiments in ASDEX Upgrade is described. Using synthetic data, the premature triggering of the HST is discussed. Data obtained at ASDEX Upgrade for technical shots are evaluated and discussed. The heat flux is validated for a semi infinite target (refer to section 6.5) using the surface temperature evaluated for the spectrometer. Piggy back measurements (measurements dedicated to others which were used for the IR spectroscopy) taken in the presence of plasma, using the spectrometer, are shown and discussed.

6.1. Experimental Setup

As described in section 1.4, the neutral beam of the fourth source of the second neutral beam box (source 8) hits the heat shield almost radially. The IR spectrometer is mounted so that the shine through location of source 8 is observed.

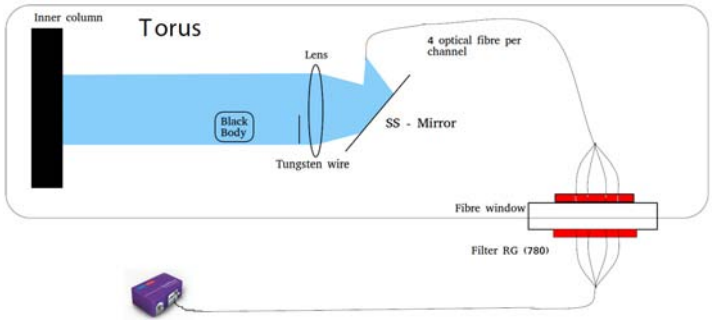

Figure 6.1.: The experimental set up during the calibration of the spectrometer in ASDEX Upgrade [34].

Figure 6.1 shows the experimental setup. The rectangular box, in which the torus is illustrated, represents the vacuum vessel. The light coming from the heat shield is directed by a lens and a mirror to optical fibres. The optical fibres are mounted on a support (marked in red) in front of the fibre window. On the other end of the fibre window, other optical fibres are connected on the support which transmit the light coming from the vessel to the spectrometer. Only one fibre is used for the calibration and during the experiments. In addition to the IR spectrometer, an IR camera has been positioned to observe the shine through location on the heat shield directly.

6.2. Calibration in ASDEX Upgrade

At the end of the maintenance period of ASDEX Upgrade, before the closure of the vacuum vessel, the IR spectrometer is calibrated using a black body. The black body is placed on the optical path in the vacuum vessel, shown in figure 6.1. The temperature of the black body is increased gradually and the number of counts is measured. The data is calibrated as discussed in chapter 4. Figure 6.2 (a) shows an example of raw data received from the IR spectrometer. The data corresponds to a temperature of 1173 K of the black body for an integration time. Figure 6.2 (b) shows the uncalibrated spectra after the number of counts measured at 1073 K (usable data obtained as from 1073 K) is subtracted as background for a non uniformity correction. It is observed that the number of counts measured in ASDEX Upgrade is significantly lower compared to the calibration in the laboratory, refer to chapter 4. Also, the number of counts measured between 1.25 - 1.5 μm is almost zero. This behaviour is analyzed in detail in section 6.3. Figure 6.3 shows the relative transmission obtained during the calibration. Comparing the number of counts measured in figure 6.2 (b) and the relative transmission curve, 6.3 (a), it is observed that the transmission is low at about 0.95 μm and almost zero between 1.2 and 1.5 μm.

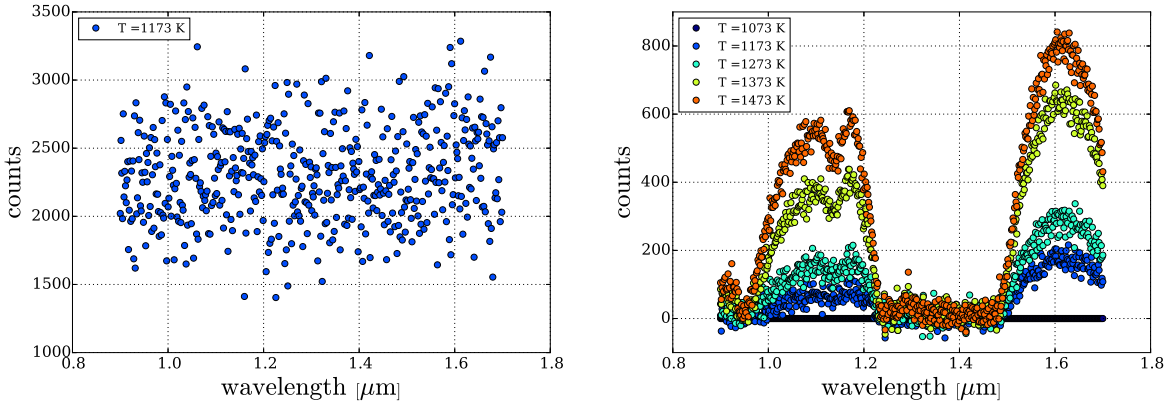

(a) RAW data for 1173 K.

(b) Background subtracted spectrum.

Figure 6.2.: Figure (a) shows the number of counts measured at 1173 K for an integration time and figure (b) shows the uncalibrated spectrum obtained after subtracting the number of counts as background measured at 800 K.

Since large wavelength intervals are blocked by the optical components, the transmission of the optical components of ASDEX Upgrade have been examined.

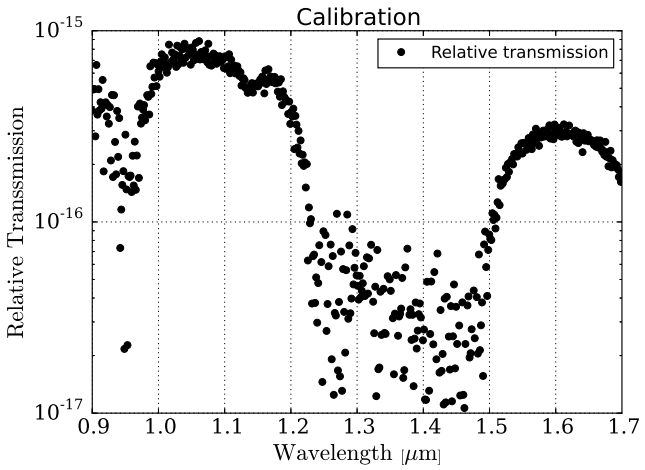

Figure 6.3.: Figure shows the relative transmission as determined from calibration.

6.3. Transmission of Optical Components

Each optical component has been tested in the laboratory to determine which one is responsible for the low transmission. First a measurement is carried out by placing a paper in front of the lens. The data from this measurement is used as background. Then a tungsten filament without any additional optical components is used to obtain a reference spectrum.

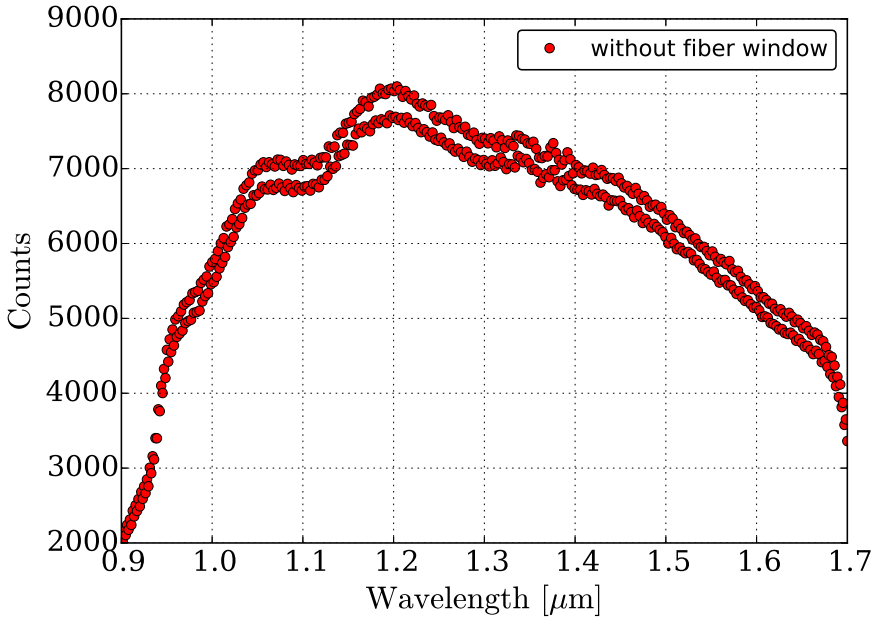

Figure 6.4.: The background subtracted signal measured by the spectrometer as reference

Figure 6.4 shows the number of counts measured by the IR spectrometer when the tungsten lamp is placed directly in front of the lens. The double spectra observed is an artifact of the detector. The measurement is repeated with the different optical components.

6.3.1. Fibre Window

A fibre window, identical to the one mounted in ASDEX Upgrade is tested by placing it in front of the lens.

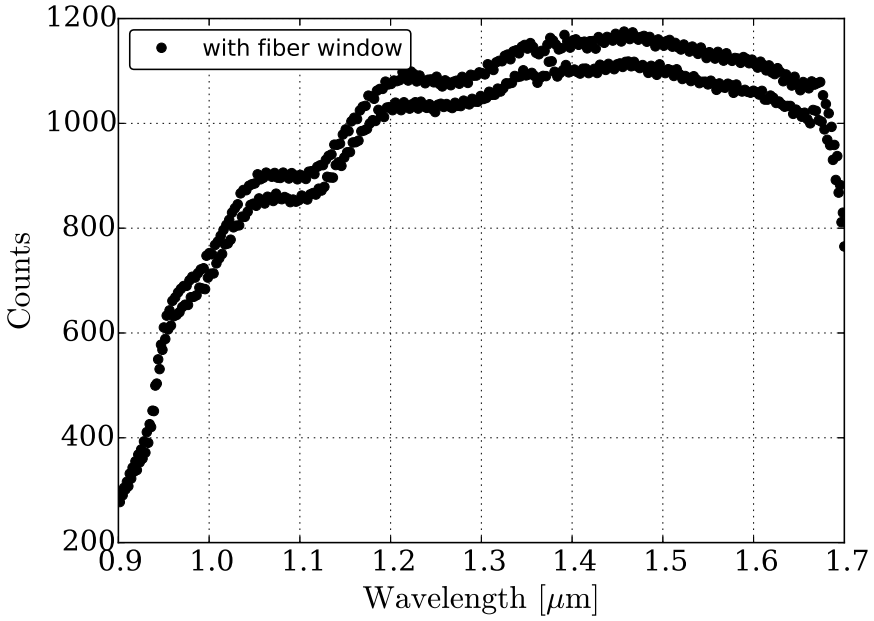

Figure 6.5.: The number of counts measured by the spectrometer with a plastic optical fibre as reference

Figure 6.5 shows the number of counts measured, after the background is subtracted, when the fibre window is placed in front of the lens. Comparing figure 6.4 and 6.5, it is observed that the fibre window absorbs the photons evenly, as the number of counts decreases for all wavelengths in the spectrum. This implies that the wavelength dependent dip cannot be due to the fibre window.

6.3.2. Optical Fibre

The IR spectrometer is connected to ASDEX Upgrade via an optical fibre. Since the fibre window did not show poor transmission the optical fibre, which is used for the diagnostics in ASDEX Upgrade, is tested. In the laboratory plastic optical fibres with a high transmission in the IR are used. In ASDEX Upgrade these optical fibres cannot be used due to the requirement of baking (to remove absorbed water and gas from the plasma facing components by heating the vacuum vessel at about 150°C [35]) the vacuum vessel. Instead of plastic optical fibres, optical fibres which can tolerate higher temperatures are

used. One end of the optical fibre used in ASDEX Upgrade is placed in front of the tungsten lamp while the other end is placed in front of the lens. Figure 6.6 (a) shows the profile obtained from the measurement.

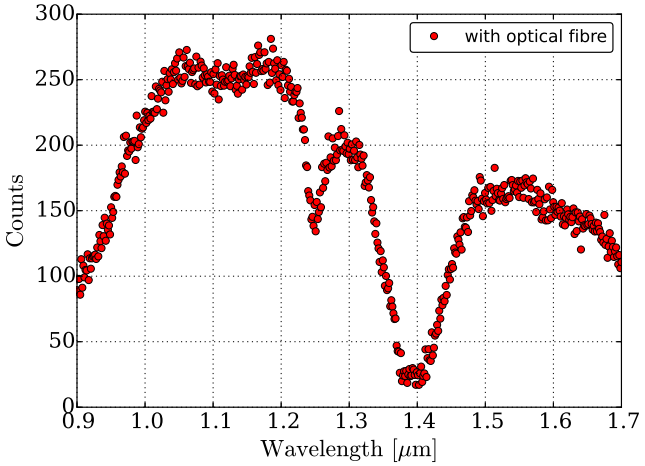

(a) Transmission of optical fibre measured.

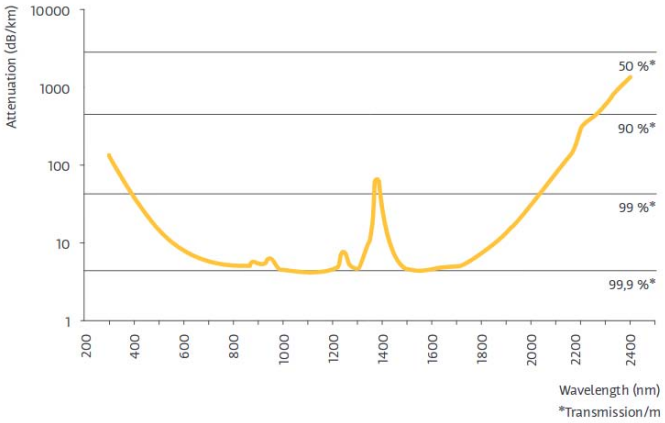

(b) Attenuation of optical fibre.

Figure 6.6.: Figure (a) shows the background subtracted signal obtained when the optical fibre used in ASDEX Upgrade is examined and figure (b) shows the attenuation curve of the optical fibre given by the manufacturer [36].

It is seen that the measurement with the optical fibre shows the same dips in the transmission that have been observed during the calibration. Figure 6.6 (b) shows the attenuation values of the optical fibre used in ASDEX Upgrade relative to the wavelengths, as provided by the manufacturer [36]. It is observed that the at 0.95, 1.2 and 1.4 μm, the attenuation increases, which is in agreement with the transmission profile measured in the laboratory. This leads to the conclusion that the optical fibre used in ASDEX Upgrade has a poor transmission in the near IR range. Comparing figure 6.3 with 6.6, it is observed that the dip measured during the calibration is between 1.2 and 1.5 μm whereas during the laboratory measurement, the dip in the transmission curve is at two wavelengths, namely 1.25 μm and 1.4 μm. Due to the low signal transmission or neutron

damage of the optical fibre the two dips are observed as one. It was not possible to change the fibres in the vacuum vessel for the experiments.

6.4. Effect of Transmission on HST

In this section the influence of the transmission determined during the calibration of the spectrometer is discussed using synthetic data.

The assumed response of the HST does not include the wavelength dependent transmission of the optical fibre. Synthetic data with the original response and data including the transmission determined are generated. The transmission and response of each diode is multiplied by Planck's equation and noise is added to calculate the photon flux, which is equivalent to the working principle of the current HST system. Since a low relative transmission is measured during the calibration of the spectrometer in ASDEX Upgrade, the influence of the transmission on the HST signal is tested. The transmission of the optical components measured in ASDEX Upgrade is applied to the known wavelength dependent response of the HST system. Integrating the photon flux over the sensitivity range gives the signal of each diode. The surface temperature is then calculated by taking the ratio of the signals as discussed in section 2.2.2.

Figure 6.7 shows the photon flux calculated for surface temperatures ranging from 500 K up to 3600 K. Figure 6.7 (a) shows the photon flux generated for the HST system in dependence to the wavelength range of the IR spectrometer. Figure 6.7 (b) shows the signals obtained for each diode, when the transmission is considered. It is observed that the signal calculated between 1.0 μm and 1.4 μm is significantly low compared to what is expected for the HST system. The silicon diode is observed to have a higher photon flux at 3600 K than the germanium diode at 3600 K, showing that the transmission of the optical fibres (see figure 6.3) changes the signal significantly.

The hardware used to monitor the surface temperature for the inner column protection evaluates the surface temperature from the logarithmic ratio of the signal from the silicon and germanium diode.

Figure 6.8 (a) shows the logarithmic signals ratio calculated in dependence to the surface temperature determined. The black curve shows the signal evaluated the normal HST signal and the logarithmic signal ratio considering the transmission measured during the calibration is shown in red.

The red curve shows that at low temperatures the influence of the relative transmission measured during the calibration is negligible but at high temperatures the signal ratio is higher than that measured by the normal HST. Due to the transmission curve, the silicon diode measures a higher photon flux compared to the germanium diode and leads to a higher signal ratio. Figure 6.8 (b) shows the surface temperatures evaluated with respect to the real surface temperatures. In red the surface temperature measured for the signal including the relative transmission curve is plotted. The surface temperature measured by the HST is assumed to be correct. For the signal including the relative transmission (red curve), it is observed that the surface temperature evaluated corresponds to the surface temperature determined by the current HST system at low temperatures only.

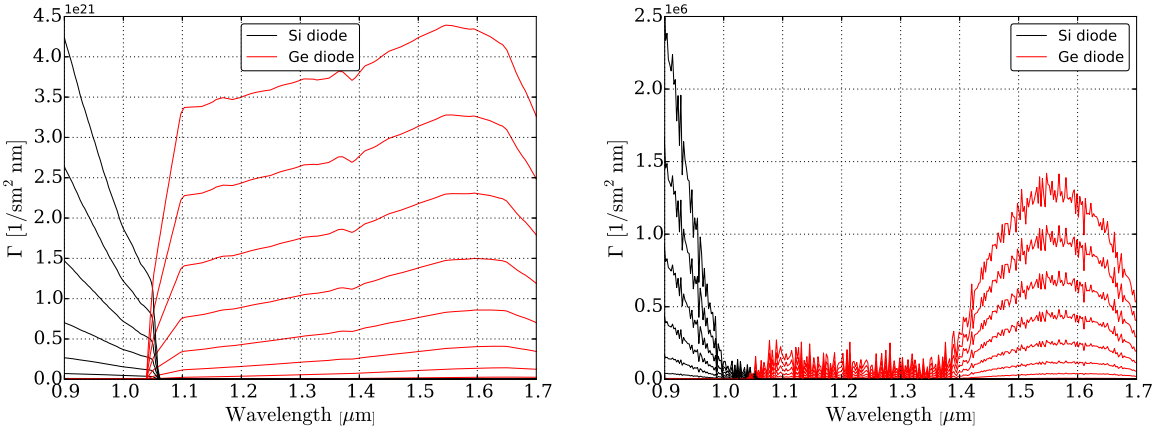

(a) Signal expected for HST.

(b) Signal for the HST with the transmission evaluated during AUG calibration.

Figure 6.7.: Figure (a) shows the total signal as expected for the HST system and figure (b) shows the total signal as expected for the HST with the transmission evaluated during the calibration of the spectrometer in AUG.

Starting from 900 K, the influence of the relative transmission increases with increasing temperatures. As the surface temperature increases, Planck's curve shifts toward smaller wavelength, see figure 2.1. Therefore, the photon flux measured by the silicon diode is higher than the germanium diode resulting in an increase of the signal ratio. Thus, the surface temperature evaluated is significantly overestimated.

Using the knowledge acquired from the synthetic data, it is deduced that the HST system in ASDEX Upgrade would be triggered, with a consequent switching off of the NBI, as the surface temperature limit set would be reached. For the ASDEX Upgrade data analysis the measured tramsmission is taken into consideration.

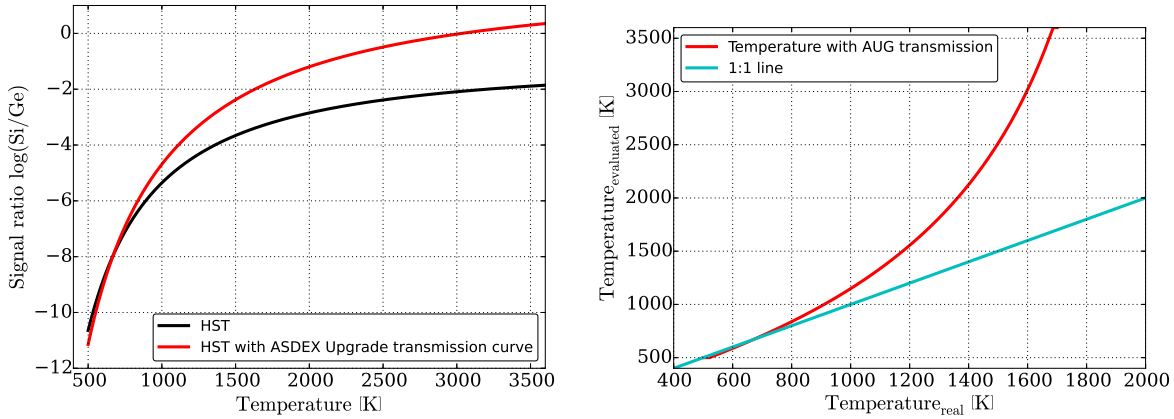

(a) Logarithmic signal ratio evaluated for HST

(b) Temperature evaluation.

Figure 6.8.: Figure (a) shows the ratio of silicon to germanium signal and figure (b) shows the evaluated temperature as measured by the HST.

6.5. NBI Pulses without Plasma

In this section the technical shots carried out to test the IR spectrometer are described and the results are discussed.

In ASDEX Upgrade NBI pulses without plasma are routinely performed to commission the HST system. The NBI has a rectangular temporal pulse shape with a constant heat flux density. Part of the heat shield in ASDEX Upgrade has recently been changed from tungsten coated graphite to steel. Since the spectrometer is mounted to view the shine through location on the inner heat shield of the source 8 of the NBI, only source 8 is used for the experiment. Source 8 deposits its heat load on the steel tiles. The peak surface temperature tolerable during operations is determined by the melting temperature of steel which is about 1500°C. The semi infinite solution of the 1D heat conduction equation is applied to the short pulse duration, where the heating time is smaller than the time the heat needs to diffuse through the tile. For a diffusion length d the time taken for the heat to diffuse in is given by [37]:

$$t = \frac{d^2}{8.5\alpha} \tag{6.1}$$

$$\alpha = \frac{\kappa}{\rho c_p} \tag{6.2}$$

Here the material parameters are ρ, κ and c_p, which are density, thermal conductivity, specific heat capacity, respectively, and α is defined as the diffusivity. The material parameters for the steel tiles are the following:

- Thermal conductivity, κ : 25 $\frac{\mathrm{W}}{\mathrm{mK}}$
- Density, ρ : 7700 $\frac{\mathrm{kg}}{\mathrm{m}^3}$
- Specific heat capacity, c_p : 450 $\frac{\mathrm{J}}{\mathrm{kgK}}$

The steel tile in ASDEX Upgrade is about 14 mm thick, 210 mm long and 87 mm wide [22]. For $d = 14\,\text{mm}$ and $\alpha = 7.22 \cdot 10^{-6}\frac{\text{m}^2}{\text{s}}$, the critical heat diffusion time is about 3 s. The pulse duration of the NBI shots were much smaller than the critical heat diffusion time and the diffusion length calculated for the NBI shots are much smaller than the thickness of the steel tile. Therefore, the semi infinite solution can be applied and, the surface temperature evaluated is given as [33]:

$$T(t) = \frac{2}{\sqrt{\pi}} \cdot \frac{1}{\sqrt{\kappa \rho c_p}} \cdot q \cdot \sqrt{t} \tag{6.3}$$

Using this equation, the maximum allowed pulse duration is calculated as follows:

$$\tau = \frac{\pi \kappa \rho c_p \cdot T_{max}^2}{4 \cdot q^2} \tag{6.4}$$

and the temperature decay, for a pulse duration τ, after the heat flux is switched off is described as follows [38]:

$$T_{max} = \frac{2}{\sqrt{\pi}} \frac{q}{\sqrt{\kappa \rho c}} \sqrt{\tau} \tag{6.5}$$

$$T(t) = T_{max} \cdot \left(\sqrt{1 + \frac{t}{\tau}} - \sqrt{\frac{t}{\tau}} \right) \tag{6.6}$$

Equations 6.3 and 6.6 are fitted to the evaluated surface temperature to determine the heat flux density.

The maximum heat flux calculated for the inner heat shield for source 8 is between 8 - 33 $\frac{\text{MW}}{\text{m}^2}$ depending on the accelerating voltage of the beam. For a full power a maximum pulse duration of 78 ms is allowed assuming a start temperature of steel tile of 373 K and a maximum surface temperature of 1534 K. To be able to collect more data points with the IR spectrometer, the pulse duration is increased by reducing the heat flux density of the NBI. Therefore, the technical shots were carried out with a reduced neutral beam voltage of 50 kV giving a neutral beam power of 0.72 MW which corresponds to a heat flux density of 9.5 $\frac{\text{MW}}{\text{m}^2}$. For this heat flux and the maximum tolerable temperature rise of 1534 K for the heat shield, a maximum pulse duration of 1.77 s is calculated. With these settings, the pulse duration is varied as shown in table 6.1. The HST system was active to assure machine safety.

Even though a pulse duration of 1.1 s was requested for shot 34152, the pulse duration achieved was 0.93 s, since the HST system switched off the NBI.

From the evaluation of the GLADIS data, it is deduced that at least a linear wavelength dependent emissivity is needed to derive the temperature from the measured signal. Taking the measured transmission into account and using the following model, the data for ASDEX Upgrade are anlyzed:

$$\text{Model}_{\text{AUG}} = a_0 \cdot (1 + a_1 \cdot \lambda) \cdot \Gamma_{\text{Planck}} \tag{6.7}$$

Shot	Pulse duration requested $[s]$	Pulse duration achieved $[s]$
34121	0.5	0.5
34122	0.8	0.8
34129	0.8	0.8
34152	1.1	0.93

Table 6.1.: In the table the pulse duration of each shot is listed.

$$\Gamma_{\text{Planck}} = \varepsilon \frac{2\pi c}{\lambda^4} \cdot \frac{1}{\exp\left(\frac{hc}{\lambda k_B T}\right) - 1} \tag{6.8}$$

Figure 6.9 shows the raw data of the IR spectrometer. Before the NBI is switched on, the HST system is tested using a tungsten filament. The surface temperature of the tungsten filament is evaluated in a way similar to that of the NBI shots. When the tungsten filament is switched on, a temperature of about 2600 K is achieved, and since this temperature is above the limit set, the HST system has to switch off. The switching off the HST system means that the safety system of the machine is working properly and only then the NBI system gets the clearance to operate. For the technical shot, the system is set such that 10 s after the tungsten filament is switched off, the NBI starts to operate.

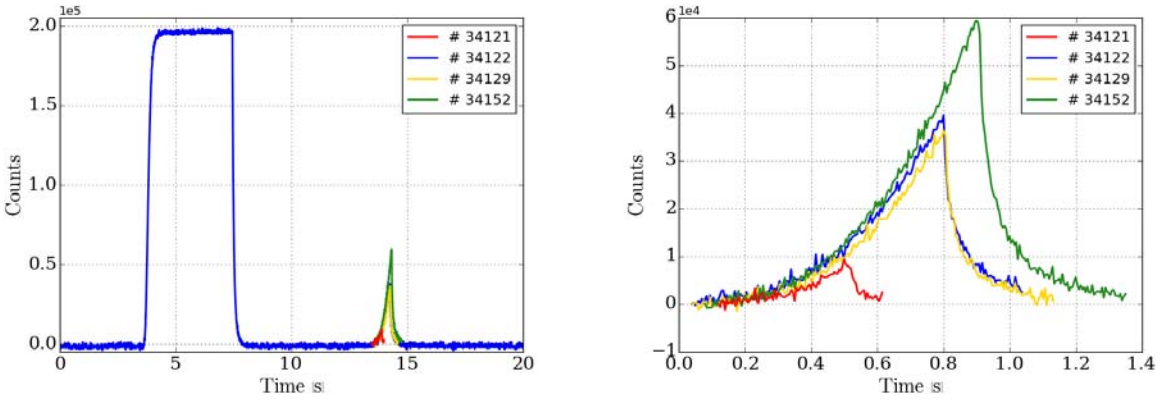

(a) (b)

Figure 6.9.: Figure (a) show the signal obtained for the four technical shots and figure (b) shows a zoom in of the four shots only.

Figure 6.9 (a) shows the total counts obtained for the tungsten filament (square signal) and the four shots. Figure 6.9 (b) shows a zoom in of figure 6.9 (a), where the total counts of the four shots are plotted in dependence to the pulse duration.

Figure 6.10 (a) shows the surface temperature evaluated for all the four shots. A lower detection limit of 1100 K is found for the IR spectrometer measurements in ASDEX Upgrade. Comparing the lower detection limit of GLADIS, which is 850 K (see figure 5.5), it is seen that the credibility limit for the ASDEX Upgrade measurement is higher. This is because the optical components used in GLADIS have a better transmission, therefore more signal is obtained for the surface temperature evaluation. The scattered points at the beginning and at the end show an increased noise level. With increasing surface temperature the noise is decreased. Figure 6.10 (b) shows the surface temperature evaluated for shot 34152 with the semi infinite fit to validate the heat flux.

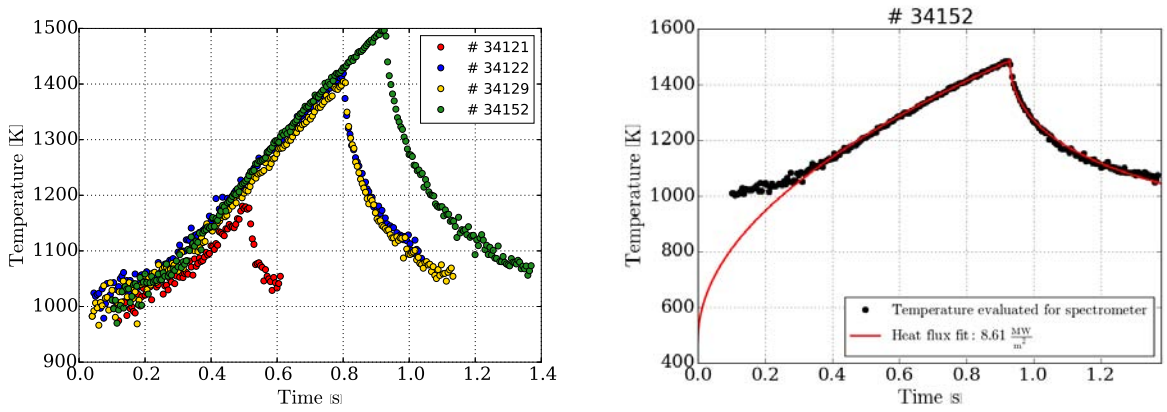

(a) (b)

Figure 6.10.: (a) shows the surface temperature evaluation of the four technical shots and (b) shows an example of the surface temperature of shot 34152 with the semi infinite fit

The same has been done for the IR camera. The IR camera is not calibrated for the steel targets. Therefore, the calibration of the IR camera has been adapted to be in agreement with the peak temperature of the spectrometer.

Figure 6.11 (a) shows an image of the temperature distribution on the inner column. The area used to evaluate the surface temperature is marked by the black rectangle. The area is chosen such that no hot edges are included in the surface temperature evaluation. The heat flux evaluated for both IR spectrometer and IR camera are listed in table 6.2. There are no data for shot 34121 because the shot is used to find the correct position, which is the center of the beam profile on the inner column. The heat flux calculated for both IR measurements are later compared to the heat flux evaluated by the NBI group.

The emissivity value has been changed in the programm used to get data of the IR camera, such that the peak temperatures of the IR camera and spectrometer are in agreement. For example, the peak temperature of the spectrometer for shot 34152 is 1483 K. To evaluate a peak temperature about 1483 K for the IR camera, the emissivity value used is 0.14, as shown in figure 6.12 (a). Figure 6.12 (a) shows that with increasing emissivity the evaluated peak temperature decreases. Figure 6.12 (b) shows the heat flux calculated for the IR camera in dependence of the emissivity. For an emissivity of 0.14, the heat flux calculated from equation 6.3 and equation 6.6 is about 13 $\frac{\mathrm{MW}}{\mathrm{m}^2}$, see table 6.2. For the

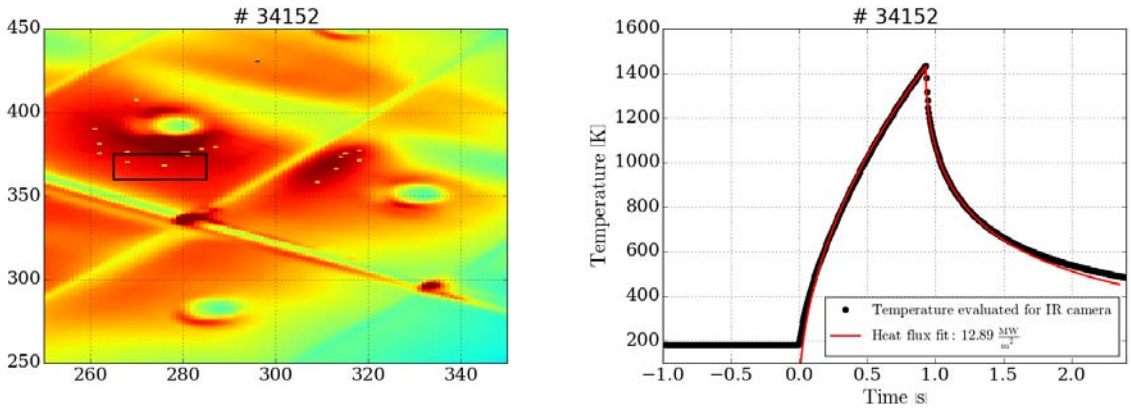

(a) (b)

Figure 6.11.: Figure (a) shows an image of the temperature distribution on the target and (b) shows the surface temperature evaluated with the semi infinite fit to validate the heat flux.

Shot	**Heat flux spectrometer** $\left[\frac{\mathbf{MW}}{\mathbf{m^2}}\right]$	**Heat flux camera** $\left[\frac{\mathbf{MW}}{\mathbf{m^2}}\right]$
34121	8.05	No data
34122	8.15	12.90
34129	8.09	12.85
34152	8.61	12.89

Table 6.2.: In the table the heat flux evaluated for the IR spectrometer data and IR camera are listed.

heat flux of both IR devices to be in agreement, an emissivity of 0.30 is needed for the IR camera. Since the peak surface temperature is significantly lower than evaluated for the spectrometer, this value is not used. The adapted calibration of the IR camera might be incorrect, thus leading to a deviation in the evaluated heat flux.

Figure 6.13 (a) shows the total heat flux at 9 m distance from the source as evaluated by the NBI group. To get the heat load on the wall, the angle of the beam onto the inner heat shield needs to be taken into account. Figure 6.13 (b) shows the FWHM calculated for the beam profile [39]. From figure 6.13 it is seen that the maximum heat flux is about 13 $\frac{\mathrm{MW}}{\mathrm{m^2}}$ in 9 m distance from the inner heat shield and the shine through location on the wall has Full Width Half Maximum of about 20 cm. The IR camera has been positioned such that the center of the shine through location is observed. The deviation in the heat flux reported in table 6.2 is because the spectrometer measures an averaged surface temperature whereas for the IR camera the position of the maximum temperature

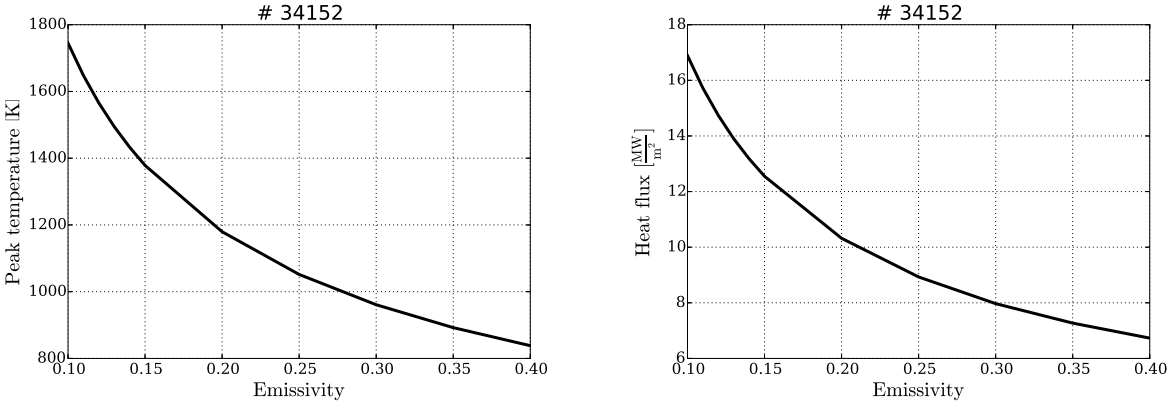

(a) Peak temperature of IR camera

(b) Heat flux calculated for IR camera

Figure 6.12.: Figure (a) shows the peak temperature obtained in dependence of the emissivity and (b) shows the heat flux evaluated for different emissivity value.

is evaluated. It is also possible that the spectrometer did not view the center of the shine through location but rather on the edge of the beam profile.

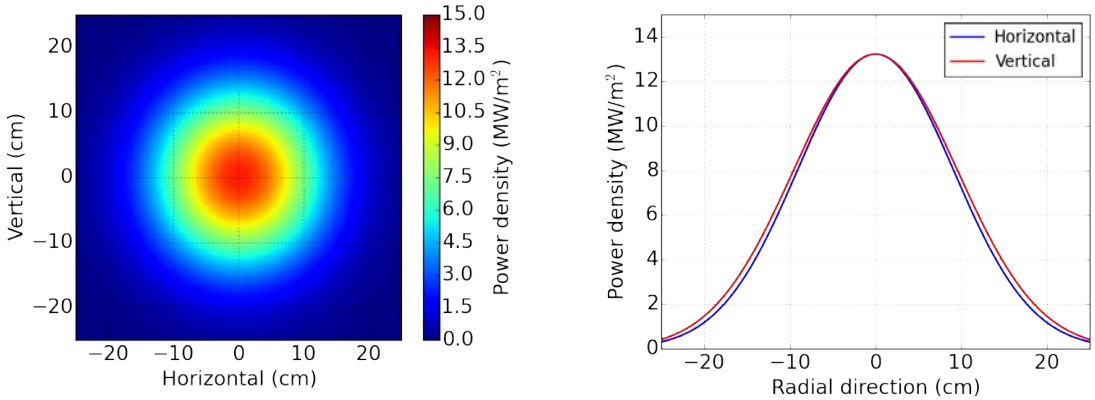

(a) Theoretical heat flux evaluated

(b) Heat flux distribution

Figure 6.13.: Heat flux distribution at 9 m from the source [39].

Figure 6.14 (a) show the temperature image of shot 34152 taken by the IR camera. Four areas, marked by the black rectangles, are chosen on the temperature image to investigate the heat flux distribution. Figure 6.14 (b) shows the heat flux evaluated for each area against the approximate position on the steel tiles.

Figure 6.15 shows the dependence of the heat flux, evaluated on the heat shield, on the beam divergence for a beam power of 0.72 MW. It is observed that with increasing divergence the heat flux evaluated decreases. The NBI group has measured the divergence with beam emission spectroscopy and a divergence of $0.76^{+0.18}_{-0.14}$ degrees for the main component energy component [39]. The heat flux expected for a divergence of 0.8° is about 8 $\frac{\mathrm{MW}}{\mathrm{m}^2}$, which corresponds to the heat flux evaluated for the spectrometer data. The radial extent of the beam predicted by the NBI group is in agreement with the

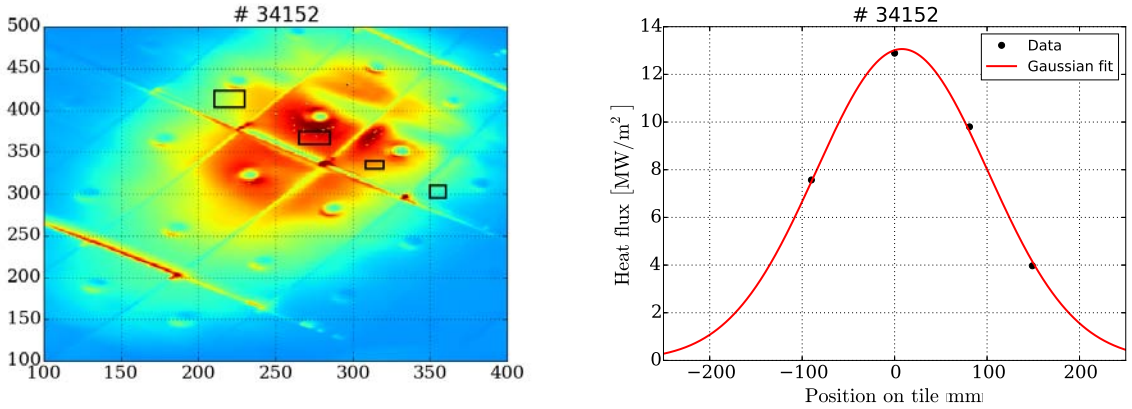

(a) Positions of the data on the tiles

(b) Heat flux distribution

Figure 6.14.: Figure (a) shows the area taken to calculate the heat flux and figure (b) shows the approximate beam profile calculated for the IR camera

measured beam profile by the IR camera. We can conclude that deviation in the heat flux evaluated using the spectrometer and IR camera is due to the adapted calibration of the camera.

A second set of discharges with the full beam power has been performed to study the influence of the gas and the residual magnetic field on the beam deposited heat flux. Even though there was no magnetic field set for the discharges, a small amount of magnetic field can exist due to a small current in the magnetic field coils, which will be called residual magnetic field (rmf), in this work. This is due to the large flywheel generator (EZ2) which was not completely switched off. The behaviour of the neutral beam is investigated with and without gas in the vacuum vessel. For comparison three discharges (34362, 34363 and 34365) were carried out without any magnetic field, i.e, no residual magnetic field was present. Since the discharges are performed with the maximum beam power of 2.5 MW, the maximum pulse duration allowed is 78 ms. The details of the different discharges are listed in table 6.3.

Figure 6.16 shows the heat flux evaluated for two discharges in the presence of deuterium gas. The difference between figure 6.16 (a) and 6.16 (b) is that for discharge 34328 residual magnetic field was present and for discharge 34365 there were no magnetic field. Comparing figure 6.16 with figure 6.10 (b) it is observed that due to the very short pulse duration less data points are recorded. From table 6.3 it is seen that the heat fluxes evaluated for $B = 0$, do not differ significantly in the presence of gas. With the residual magnetic field, a significant difference in the evaluated heat flux is observed in the presence of gas. Discharges 34335 and 34363 were not performed on the same day. The small deviation of the heat flux evaluated could be that the configuration of NBI was not exactly the same for both experiments.

From figure 6.17 is is seen that for normally assumed divergence of 0.8°, the expected heat flux, for a full power beam, is about 28 $\frac{\mathrm{MW}}{\mathrm{m}^2}$. The heat flux evaluated for discharge 34328 and 34329 are in agreement with the expected heat flux. For discharge 34331, 34334 and 34335, the evaluated heat flux is about 40 $\frac{\mathrm{MW}}{\mathrm{m}^2}$. Since the presence of the gas alone should not influence the measurement in case without the residual field, a possible

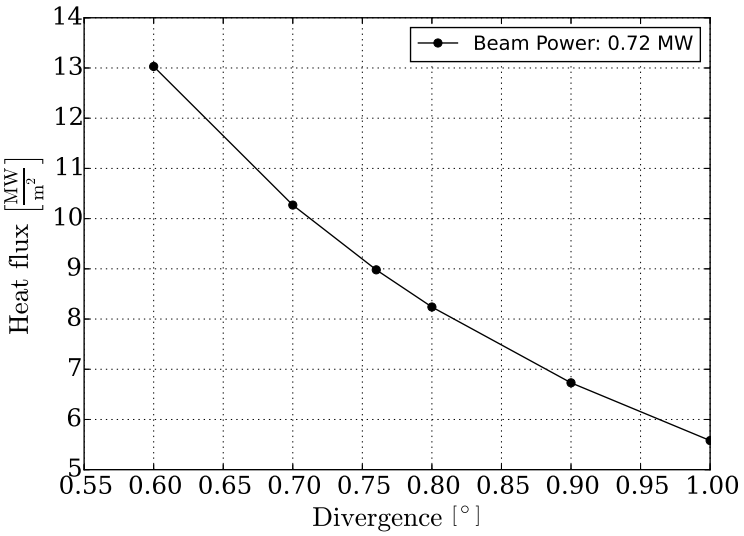

Figure 6.15.: The figure show the heat flux on the inner heat shield evaluated for different beam divergence for a minimum beam power of 0.72 MW [39]

explanation for the deviation of the heat flux value could be that the divergence of the beam has changed. In Figure 6.17 it is seen that a small increase of 0.05°, leads to a significant decrease in the heat flux expected. This is because the area on which the heat load is deposited increases for a wider beam. Another possible explanation for heat flux deviation is that the beam shifted due to the residual magnetic field. In the presence of deuterium gas, ions are generated due to collisions with the gas and charge separation. Since a residual magnetic field is present, the ions are deflected. Thus, the position of the heat load deposition of the neutral beam on the heat shield is shifted. Figure 6.18 shows the influence of the residual magnetic field on the beam. It is seen that the beam shift increases with increasing residual magnetic field. A residual magnetic field of 3 mT leads to a beam shift of about 6 cm. The shifting of the neutral beam results in a lower heat flux measurement as the spectrometer does not view the center of the beam, but the edge. The residual magnetic field is most likely to be the cause of the deviation in the heat flux evaluated.

Using the surface temperature determined by the spectrometer data, the heat flux has been validated. A deviation in heat flux evaluated for the spectrometer and IR camera is seen. The IR camera is not calibrated for the steel tile and has therefore been adapted to be in agreement with the peak temperature of the spectrometer. The deviation in heat flux evaluation might be due to the adapted calibration of the IR camera. For the heat flux evaluation, a divergence of 0.8° is usually calculated [39]. For this divergence it is seen that the heat flux evaluated by the spectrometer is in agreement with the heat flux predicted by the NBI group for the 50 kV shots where the exact divergence is unknown. Discharges were performed to study the influence of gas and residual magnetic field on the neutral beam. For the discharges with a full beam power of 2.5 MW, the heat flux determined are within the error bars of the beam divergence. The results show that the presence of deuterium gas alone does not have a significant influence on the neutral beam.

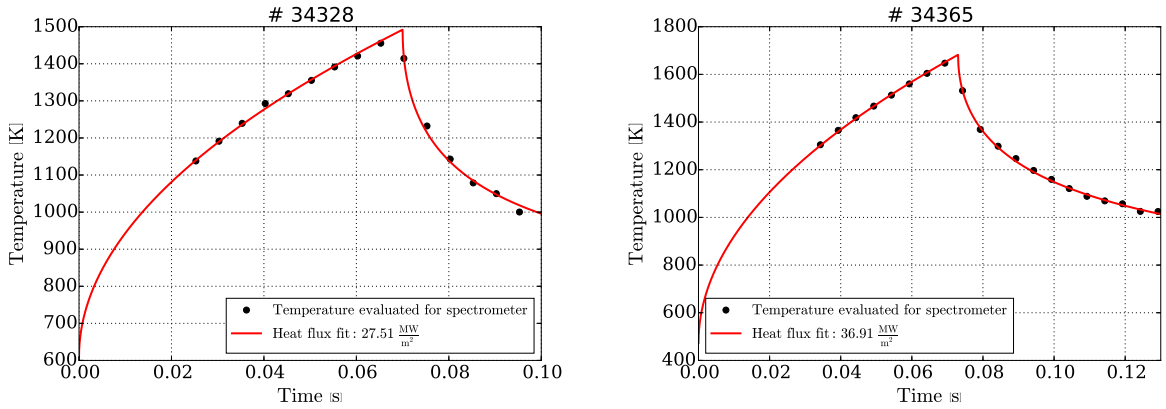

(a) With residual magnetic field

(b) No magnetic field

Figure 6.16.: Example of 2 shots carried out in the presence of deuterium gas.

Compared to the gas, it is seen that a residual magnetic field of a few mT influences the measurement significantly when gas is present.

Shot	**Pulse duration** [ms]	**Gas**	**Magnetic field**[mT]	**Heat flux** $\left[\frac{\mathbf{MW}}{\mathbf{m^2}}\right]$
34328	70	D	rmf	27.51
34329	70	D	rmf	28.44
34331	70	-	rmf	39.31
34334	60	-	rmf	41.04
34335	70	-	rmf	41.14
34362	73	D	0	37.27
34363	73	-	0	38.01
34365	73	D	0	36.91

Table 6.3.: In the table the heat flux evaluated for the IR spectrometer data for a maximum beam power of 2.5 MW are listed.

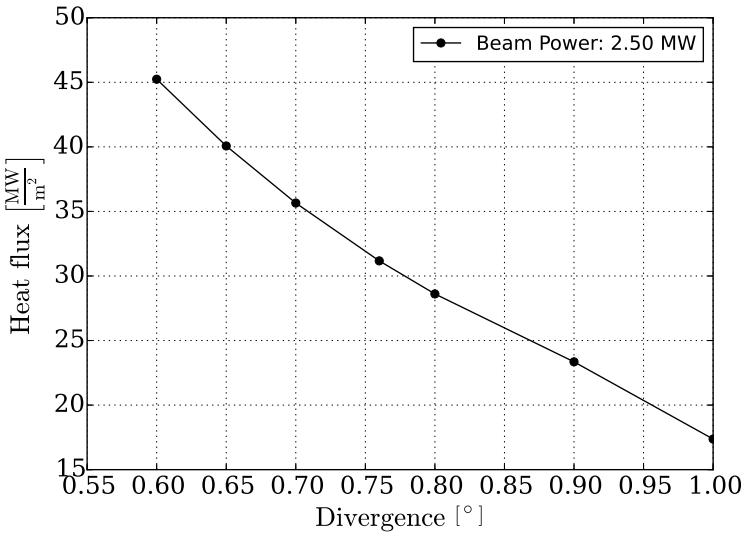

Figure 6.17.: The figure shows the heat flux evaluated on the inner heat shield for different beam divergence for a maximum beam power of 2.5 MW [39]

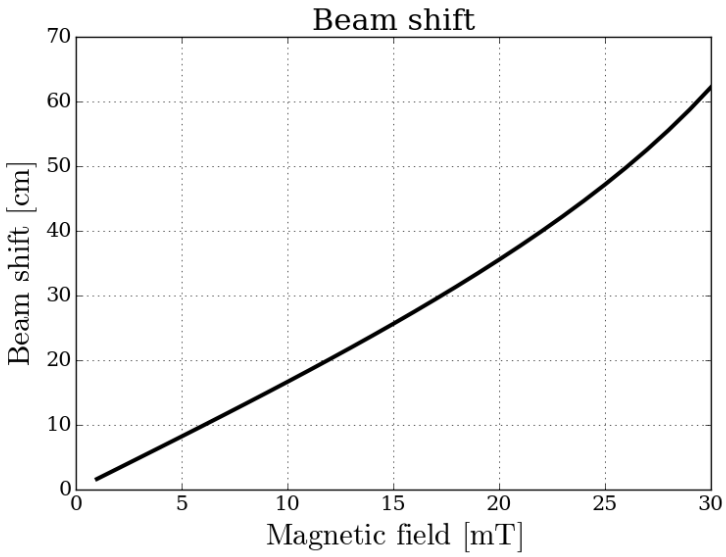

Figure 6.18.: The figure shows the effect of residual magnetic field on neutral beam.

6.6. Measurement during Plasma Operation

In this section the evaluation of measurements performed by the IR spectrometer in the presence of plasma is discussed. The discharges performed were not dedicated to test the spectrometer, they were performed piggy back.

6.6.1. Observed Shine Through

Figure 6.19 (a) shows the signal obtained for discharge 34138. Physics goal of the discharge was investigation of the impact of so-called energetic particle modes on fast-ion confinement and current drive for the collective Thomson scattering diagnostics. The parameters for this plasma discharge are:

- Toroidal magnetic field, B_t : $-2.6\,\mathrm{T}$
- Electron density, n_e : $5.8 \cdot 10^{19}\,\mathrm{m}^{-3}$
- Total NBI heating power : $5.9\,\mathrm{MW}$

For the heating power three neutral beam sources are used, one of which is source 8. Source 8 operated with the maximum power of 2.5 MW for 7.6 s. Since the signal to noise ratio is low, the measurement obtained was not from the beginning of the discharge. This explaines the peak of the pulse at about 5.5 s. For a technical shot with maximum power, a pulse duration of 78 ms is allowed, as 100% of the neutral beam power is deposited onto the heat shield. Since a plasma with electron density of $5.8 \cdot 10^{19}\,\mathrm{m}^{-3}$ is present, the shine through is only 4% [40]. Therefore a longer pulse duration is allowed. Figure 6.19 (b) shows that the surface temperature is successfully evaluated from the signal measured in the presence of plasma. It is observed that at the beginning and at the end of the signal the surface temperature evaluated has a high uncertainty which is represented by the scattering of the data..

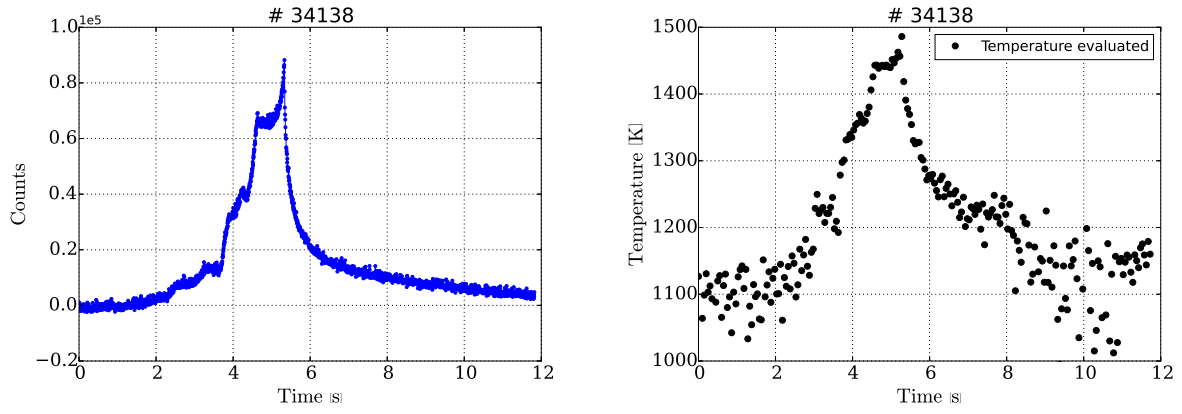

(a) (b)

Figure 6.19.: Figure (a) shows the raw data of shot 34138 and figure (b) shows the surface temperature evaluated.

The measured pulse is not described by the square-root of time since the shine through varied over time. Also, no heat flux evaluation is performed since the base temperature of the tiles is below the measurement threshold. Discharge 34138 is an example that spectroscopic measurement during a discharge is possible. No influence of Bremsstrahlung has been observed during the early phase of the 2017 campaign of ASDEX Upgrade.

6.6.2. Line Radiation

In the following discharge an interesting event is detected. The discharge 34140 is carried out to demonstrate post-disruption runaway electron beam control and to extend the understanding of the runaway electron physics and of their interaction with injected gas and magnetic perturbation. The parameters for this plasma discharge are:

- Toroidal magnetic field, B_t : $-2.6\,T$
- Electron density, n_e : $3.0 \cdot 10^{19}\,m^{-3}$
- Total NBI heating power : $0\,MW$
- Heating power, ECRH : $1.76\,MW$

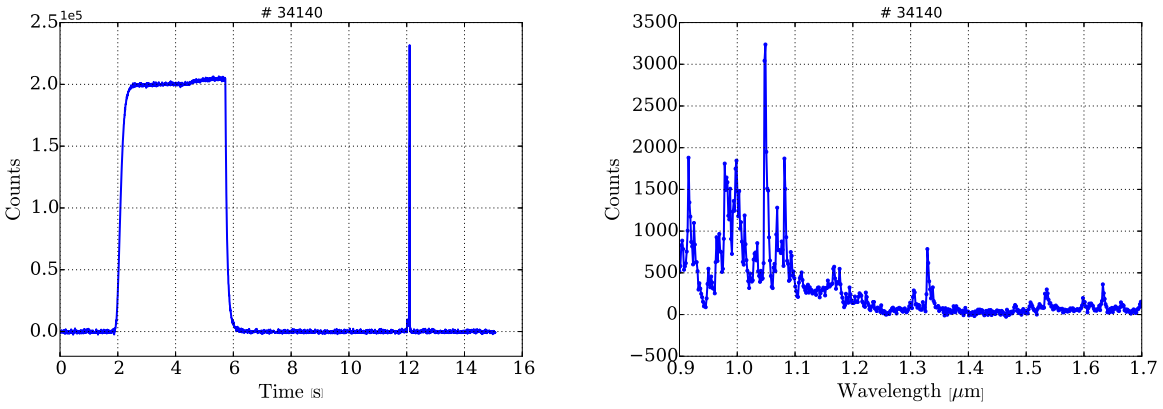

(a) (b)

Figure 6.20.: Figure (a) shows the raw data of shot 34140 and figure (b) shows an example of a spectrum.

Figure 6.20 (a) shows the signal of the tungsten filament and the signal measured during plasma discharge 34140. A strong photon emission is observed during the disruption even though no NBI heating has been used. The signal of discharge 34140 is compared to that of discharge 34138 to investigate if the signal obtained is due black body radiation. It is observed that no cooling curve is present in the signal, thus deducing that the event measured is not a thermal effect. Figure 6.20 (b) shows a spectrum of the signal. Thus, concluding that the event detected by the spectrometer is line radiation. During the disruption gas is injected into the device which is excited and thus causing line radiation. The evaluation of the data of this discharge is challenging. Impurities like argon and neon are injected in the plasma and the targets are partly made up of steel and the graphite tiles are coated with tungsten. The line radiation observed could be from all

materials given above. After searching for the possible line radiation in the wavelength range of the IR spectrometer on the website of NIST (National Institute of Standards and Technology), following results are obtained for the different elements:

- Argon : 440 lines
- Neon : 429 lines
- Tungsten : 115 lines
- Iron : 4261 lines

Taking all the four elements into consideration, it means that in the wavelength range of the spectrometer 5245 lines spectra exist. Therefore, the spectra obtained are compared to the ASDEX Upgrade spectroscopy group. In the visible range spectrometer, spectra for Ar and Ar I is observed [41]. The spectra for Ar I obtained from the visible spectrometer measurement are compared to those obtained from NIST for the spectral range of the IR spectrometer. It is difficult to compare the results, as the relative intensity of the spectra obtained from NIST are all constant for the spectral range of the IR spectrometer. Due to the multitude possible transitions, there is no clear indication of the source of the line radiation. Nevertheless, the IR spectrometer is able to detect the line radiation, which is a positive result for the new diagnostic.

6.7. Summary

During the calibration of the spectrometer, it has been observed that the background subtracted signal has a non uniform distribution. Large wavelength intervals are blocked by the optical components $\lambda < 0.95\,\mu$m and $\lambda = 1.2 - 1.5\,\mu$m. Different optical components have been investigated for the poor transmission. It has been deduced that the optical fibre used in ASDEX Upgrade has a poor transmission in the spectral range of the spectrometer. The fibre window mounted in ASDEX Upgrade absorbed the photons evenly. The influence of the poor transmission on the HST is shown by synthetic data. It is seen that with increasing temperature, the surface temperature evaluated is overestimated.

NBI shots were performed to test the spectrometer in ASDEX Upgrade and an IR camera is used simultaneously to observe the shine through location. From the experimental results, it is observed that the spectrometer has a lower detection limit of 1100 K for the measurement in ASDEX Upgrade. This is due to the low signal level. Nevertheless the surface temperature has been successfully evaluated from the spectrometer data. Using the evaluated surface temperature the heat flux is validated using the semi infinite solution of heat conduction. It has been observed that the heat flux evaluated for the spectrometer and IR camera deviates. The reason for the deviation could be the adapted calibration of the IR camera, since it is not calibrated for the steel tiles. Discharges in the presence of deuterium gas and residual magnetic field were performed to investigate their influence on the neutral beam. It has been observed that the presence of gas alone does not influence the neutral beam as much as the residual magnetic field. In the presence of both residual magnetic field and gas, it could be that the position of the heat load deposition of the neutral beam is shifted. In the presence of gas, the neutral beam can form ions by collisions. The ions are then deflected by the residual magnetic field causing

the ionized particles of the beam to shift, which results in the spectrometer not viewing the center of the shine through location but its edge.

Piggy back measurements in the presence of plasma has been taken. The surface temperature has been successfully evaluated. Line radiation during a disruption has been detected by the spectrometer, thus showing the spectroscopic measurement during a plasma discharge is possible.

7. Conclusion and Outlook

In this section, the different work done to calibrate and test the IR spectrometer developed for the Heat Shield Thermography is summarized. Suggestions for the improvement of the IR spectroscopic diagnostic are given and discussed as an outlook.

7.1. Conclusion

The aim of the thesis is to test an IR spectrometer to characterize the spectral emission from the inner column of the machine, the so-called heat shield, which is designed to protect the machine against heat loads which can arise in particular, from shine through of the neutral beam injection.

To begin with, synthetic data is used to analyze the effect of emissivity and Bremsstrahlung on the evaluation of the surface temperature. The results from the synthetic data show that a wavelength-dependent emissivity needs to be considered in the temperature evaluation. A constant-emissivity fit leads to a corrupted surface temperature evaluation if the experimental emissivity is wavelength dependent. The presence of the Bremsstrahlung influences the measurement significantly at low surface temperatures. At high surface temperatures the contribution of Bremsstrahlung is negligible. If only a Planck radiation law including a wavelength-dependent emissivity is considered in the models for the analysis of data containing volume radiation, the surface temperature is overestimated. For the HST system, this would mean that the NBI is triggered before the actual surface temperature limit is reached. Therefore, in general Bremsstrahlung has to be taken into account in the analysis of the experimetal data. For the real time measurements, cases where Bremsstrahlung is present can be extracted by comparing the emissivity evaluated with known emissivity of the material, to verify if the surface temperature evaluated is correct or not.

The IR spectrometer has been calibrated in the laboratory (in the absence of plasma) against radiation from a black body. The IR spectrometer measures the number of photons, therefore to determine the surface temperature Planck's law is fitted to the data. After the characterization of the spectrometer in the laboratory, it is tested in the high heat flux test facility (GLADIS) which uses ion injectors for heat load testing of plasma facing components. GLADIS has a similar set up as ASDEX Upgrade except that no plasma and no neutralizers are present. The surface temperature of a tungsten plug is increased by exposure to the beam and is measured by the IR spectrometer. From the evaluation of the data, it is seen that the sharp temperature increase is detectable by the spectrometer. This is important for the real time diagnostic, so that the NBI in ASDEX Upgrade can be switched off on time. It is observed that the surface temperature evaluated using a constant emissivity is overestimated, which is in agreement with the

synthetic data. From the GLADIS results, it is deduced that at least a linear wavelength dependency of the emissivity needs to be included in the data analysis.

NBI shots without plasma have been carried out to test the spectrometer in ASDEX Upgrade. Two sets of discharges were carried out. The first set consists of four dedicated shots with reduced beam power of 0.72 MW and the second set of discharges were performed with full beam power of 2.5 MW to study the influence of gas and residual magnetic field on the beam deposited heat flux. The evaluation of the data shows that the spectrometer is able to detect the signal but not from the beginning of the NBI pulse. The maximum tolerable peak temperature during operation is about about 1500 K. For the spectrometer a credibility limit of 1100 K is deduced from the ASDEX Upgrade measurements. This indicates that the signal to noise ratio is low and from the calibration a poor transmission of the optical fibre has also been measured. Nevertheless, the surface temperatures of all the discharges could be evaluated and the heat flux is validated by the semi infinite solution of the heat diffusion equation. The heat fluxes evaluated from the first set of measurements using the reduced beam power are in agreement with those calculated by the NBI group. The heat flux evaluated for the second set of measurements using shorten pulses at full beam power shows that the presence of gas itself does not influence the neutral beam significantly but the residual magnetic field does. In the presence of the residual magnetic field and gas, less heat flux is observed. The neutral beam can form ions by collisions with the gas particles. In the presence of the residual magnetic field, the ions are deflected and therefore less particles hit the wall. Thus, the heat load measured on the shine through location is smaller compared to that evaluated when the magnetic field is zero. The deflection of the ions causes the position of the heat load deposition of the neutral beam to shift, thus widening the shine through location on the wall. This results in the IR spectrometer not viewing the center of the shine through location but its edge.

From piggy back measurements it is seen that the spectrometer is able to detect signals in the presence of plasma and the surface temperature evaluation is plausible. Line radiation has been successfully detected during a plasma disruption experiment. The evaluation of the line radiation is challenging because around 5000 possible transitions are present in the wavelength range of the spectrometer. From the piggy back measurements, it is deduced that spectroscopic measurement during a plasma discharge is also possible.

To conclude, the IR spectrometer has been:

- characterized in the laboratory by a black body,
- successfully tested in GLADIS and
- successfully tested in ASDEX Upgrade.

We can draw the conclusion that the IR spectrometer is a viable replacement of the two colors pyrometer used up to now for the HST system.

7.2. Outlook

For this thesis a commercially available IR spectrometer was used as diagnostic. The measurements presented in the thesis shows that the IR spectrometer is able to detect the signal but unfortunately not from the beginning of an NBI pulse. From the experiments carried out to test the IR spectrometer, it is observed that the credibility limit for the surface temperature evaluation is about 1100 K in ASDEX Upgrade. For a safety system, such a high credibility limit is not acceptable. For an improved safety system, it is important that the surface temperature can be evaluated for lower temperature. Thus, when the NBI is switched on, the surface temperature can be monitored from the beginning of the pulse. Therefore for the commissioning of the IR spectrometer in ASDEX Upgrade improvements are necessary:

- **1. Use of a cooled detector**
- **2. Wider spectral range in IR range**
- **3. Use of optical components with higher transmission**

1: The spectrometer tested in the thesis is made with an uncooled detector. Due to the uncooled detector, the electronic background is high and therefore it was difficult to differentiate between noise and actual signal during the experiments. For a safety system, an IR spectrometer with a cooled detector is needed so that the signal to noise ratio is higher. The more signal detected by the IR spectrometer, the better the surface temperature evaluation is.

2: The spectrometer tested in the thesis has a spectral range of 0.9 to 1.7 μm. With poor transmission between 1.2 to 1.4 μm, the uncertainty in the measurement is high, as 25% of the wavelength range sees no signal. By choosing a wider spectral range, for example 0.9 to 2.5 μm, only 12% of the wavelength range sees no signal, thus decreasing the uncertainty in the measurements.

3: During the calibration of the spectrometer in ASDEX Upgrade it has been found that the optical fibre currently in use has a poor transmission in the spectral range of 1.2 to 1.4 μm. For the commissioning of the IR spectrometer in the machine, the optical fibre needs to be replaced by one which allows full transmission in the spectral range of the IR spectrometer. In addition to replacing the optical fibre, choosing a wider spectral range is also a possibility. The current optical fibre used is not suitable for longer wavelengths in IR range, as the attenuation increases with increasing wavelength.

For a safety system a real time diagnostic is essential. During the experiments the data were first saved and were evaluated later. But to monitor the surface temperature of the target, it is important that the data measured are available immediately for evaluation. Thus, the surface temperature increase can be monitored as soon as the NBI is switched on. No problems connected to this step are expected.

Acknowledgement

I would like to thank my academic supervisors Prof. Emanuele Poli and Thomas Eich who enabled this thesis and for giving me valuable suggestions for my work. I can only guess, how much work it takes to accompany a master thesis.

Thank you to Albrecht Herrmann for the great assistance during the work on my thesis and helping me to understand the safety system of ASDEX Upgrade.

A special thanks goes to Bernhard Sieglin for his constant guidance and supervision. I know, how much time you spent on pointing me into the right direction!

I would like to thank the whole ASDEX Upgrade team for helping and supporting me during the experiments. Obviously I cannot list every name here.

I want to thank Henri Greuner and Bernd Böswirth for their help on the GLADIS measurements both technically and in answering my questions.

Thank you to Michael Faitsch and Dirk Nille for the productive coffee breaks and for the feedback, which brought my work forward.

I want to thank my whole family for their great support, especially my parents who always believed in me and my sister who helped me with bringing a smile back to my face during the most stressful times. And thanks to you Thomas for believing in me and supporting my studies and for your endless patience.

Appendix A.

Statistics

For the evaluation of the surface temperature, Bayesian statistics is used. A brief introduction will be given in this chapter.

A.1. Bayesian Statistics

To determine the different parameters of the model Bayesian statistics is used. Since the parameters are unknown, they are described probabilistically. Bayesian probability involves the manipulation of conditional probabilities. The Bayesian inference is defined as follows:

$$\mathrm{p}(A|B) \tag{A.1}$$

where A is a hypothesis, B is the data and $p(A|B)$ is a measure of the plausibility of hypothesis A given the truth of the information represented by data B.

The probabilities are manipulated using the sum and product rules since they provide the desired logic to handle the situation of incomplete information.

$$\text{Sum rule :} \quad \mathrm{p}(A|B) + \mathrm{p}(\overline{A}|B) = 1 \tag{A.2}$$

$$\text{Product rule :} \quad \mathrm{p}(A,B|C) = \mathrm{p}(A|C)\mathrm{p}(B|A,C) \tag{A.3}$$

$$= \mathrm{p}(B|C)\mathrm{p}(A|B,C) \tag{A.4}$$

Two hypothesis that are separated by a comma assert that both are true. $\overline{A}$ means the proposition is not correct. One of the most important calculating rules is the Bayes' theorem, which is derived by rearranging the terms on the right hand side of equation A.4. Bayes' theorem is define as follows:

$$\mathrm{p}(A|B,C) = \frac{\mathrm{p}(A|C)\mathrm{p}(B|A,C)}{\mathrm{p}(B|C)} \tag{A.5}$$

Equation A.5 can be written in a general form:

$$\mathrm{p}(H_i|D,I) = \frac{\int \mathrm{p}(H_i|I)\mathrm{p}(D|H_i,I)}{\mathrm{p}(D|I)} = 1 \tag{A.6}$$

where H_i is the proposition asserting that a hypothesis of interest is true, I is the proposition representing the prior information, D is the proposition representing the data.

p(D|H_i,I) is the likelihood function which assess the probability of the observed data arising from the hypothesis, p(H_i|I) is known as the prior and reflects the prior information in the absence of data, D and p(H_i|D,I), the posterior probability, gives the probability of the hypothesis after consideration of the data. p(D|I) is the integral of p(H_i|I)p(D|H_i,I) over all H_i which is an ignorable normalizing constant. Being a normalizing constant, p(D|I) does not affect the shape of the posterior probability distribution. Hence, the posterior probability distribution is written as seen in equation A.7.

$$\mathrm{p}(H_i|D, I) \propto \mathrm{p}(H_i|I)p(D|H_i, I) \tag{A.7}$$

A.2. Likelihood and Priors

The Central Limit Theorem states that the sum of independent and identically distributed random variables tend to a normal distribution even if the variables themselves are not normally distributed. Hence, assuming a normal distribution, the likelihood is written as follows:

$$\mathrm{p}(d_i|D_i(H), \sigma_i, I) = \frac{1}{\sigma_i\sqrt{2\pi}} \exp\left(\frac{(d_i - D_i(H))^2}{2\sigma_i^2}\right) \tag{A.8}$$

where d_i is the data measured for each pixel with an uncertainty σ_i and $D_i(H)$ is the predicted data given H_i.

Assuming that the parameters are continuous and not discrete, it is useful to calculate the probability density function (PDF) of the parameters. All the rules of the Bayes' theorem mentioned above hold for the PDF and all the sums are replaced by integrals. The global likelihood of a parameter is therefore:

$$\mathrm{p}(\mathrm{d_i}|\mathrm{D_i}, \mathrm{I}) = \int \mathrm{p}(\mathrm{p}|\mathrm{D_i}, \mathrm{I})\mathrm{p}(\mathrm{d_i}|\mathrm{D_i}, \mathrm{p}, \mathrm{I})\,\mathrm{d}p \tag{A.9}$$

To evaluate the posterior, the priors of the parameters are needed. The different parameters, p_i themselves are not of interest and are known as nuisance parameters. Compare to the frequentist method, Bayesian inference can use marginalization to get rid of the nuisance parameters. Marginalization is the procedure of integrating out the uninteresting parameters. Since the parameters are unknown and the data obtained by the spectrometer does not hold any information about any specific parameter, non-informative priors are needed. Two such priors are uniform prior and Jeffreys prior. The priors are defined as follows:

$$\text{Uniform prior} : \mathrm{p}(p_i|I) = \frac{1}{p_{i,max} - p_{i,min}} \tag{A.10}$$

$$\text{Jeffreys prior} : \mathrm{p}(p_i|I) = \frac{1}{p\,\ln(p_{i,max}/p_{i,min})} \tag{A.11}$$

Here p_{max} and p_{min} refers to the assumed range in which the value of parameter p should lie. A disadvantage of the uniform prior is that the range of parameter p should not be too large, else it would lead to an overestimated value.

For the evaluation of the surface temperature and the unknown parameters the posterior probability is needed. The posterior probability is proportional to the product of the likelihoods and the priors. The posterior probability is also the sum of each parameter's prior and the negative logarithm of the likelihood.

A.3. Application of Bayesian Probability

For the estimation of the surface temperature, the likelihood, p(D|H_i, I) and the prior probability, p(H_i|I) are calculated. The likelihood depends on the measured data, the estimated uncertainty of the data and the distribution of the uncertainty. The spectrometer measures the number of photons, even though the individual counts obey a Poisson distribution, if the measurement is repeated many times, a large number of averages is then determined. According to the Central Limit Theorem the averages will be distributed normally. Therefore, a normal distribution is used for the uncertainty.

To calculate the likelihood, the negative logarithm of equation A.8 is minimize, as the probability can be very small. The negative logarithm of the normal distribution is used for the numerical calculation of the temperature:

$$-\ln\left(\mathrm{p}(d_i|D_i,\sigma_i,I)\right) = \frac{1}{2}\ln\left(\sigma_i\sqrt{2\pi}\right) + \frac{(d_i - D_i(H))^2}{2\sigma_i^2} \tag{A.12}$$

Since the absolute values are not of interest, the constant part can be neglected and is as follows:

$$-\ln\left(\mathrm{p}(d_i|D_i,\sigma_i,I)\right) \propto \frac{(d_i - D_i(H))^2}{2\sigma_i^2} \tag{A.13}$$

The surface temperature is calculated using the parametrized model by parameters **p**. To calculate the posterior, not only the likelihood but also the priors of the parameters p_i, describing the measurement, are needed. Similar to the likelihood, the negative logarithm of equations A.10 and A.11 are used for the numerical calculation.

$$-\ln\ \mathrm{p}(p_i|I) = \ln\left(p_{i,max} - p_{i,min}\right) \tag{A.14}$$

$$-\ln\ \mathrm{p}(p_i|I) = \ln\left(x \cdot p_{i,max}/p_{i,min}\right) \tag{A.15}$$

Now that the likelihood and the priors are determined, the posterior probability can be calculated using equation A.7. Again for the numerical calculation, the negative logarithm of the posterior probability is used:

$$-\ln(\mathrm{p}(H_i|D,I)) \propto -\sum_i \ln(\mathrm{p}(H_i|I)) - \sum_j \ln(p(D|H_j,I)) \tag{A.16}$$

Bibliography

[1] Wikipedia. Nuclear fusion. https://en.wikipedia.org/wiki/Nuclear_fusion#/media/File:Deuterium-tritium_fusion.svg.

[2] Steffen Potzel. *Experimental Classification Of Divertor Detachment.* PhD thesis, University of Bayreuth, Germany, 2012.

[3] John Wesson. *Tokamaks, 3rd Edition.* Oxford University Press, 2004.

[4] H.S. Bosch. *Basic nuclear fusion, lecture script.* IPP Summer University, Munich, 2014.

[5] ITER: https://www.iter.org/mach.

[6] Wikipedia. Tokamak. http://en.wikipedia.org/wiki/Tokamak.

[7] IPP: http://www.ipp.mpg.de/16208/einfuehrung.

[8] B. Sieglin. *Divertor Power Load Studies In All Metal ASDEX Upgrade and JET.* PhD Thesis, Max-Planck Institute for Plasma Physics, Boltzmanstraße 2, Garching München, 2014.

[9] R. Neu et al. Overview on plasma operation with a full tungsten wall in ASDEX Upgrade. *Journal of Nuclear Materials*, 438, Supplement:S34 – S41, 2013.

[10] IPP: http://www.ipp.mpg.de/16340/stand.

[11] IPP (internal link): http://www.aug.ipp.mpg.de/open/.

[12] W. Demtröder. *Experimentalphysik 3, 4. Auflage.* Springer, 2010.

[13] R. Siegel and J. Howell. *Thermal Radiation Heat Transfer.* CRC Press, July 25, 2011.

[14] Lowel EDU. Color temperature in imaging:. http://lowel.tiffen.com/edu/color_temperature_and_rendering_demystified.html.

[15] B. Sigelin et al. Power load studies in jet and asdex upgrade with full-w divertors. *Plasma Phys. Control. Fusion*, 55(12).

[16] K.-P. Möllmann M. Vollmer. *Infrared Thermal Imaging.* Wiley-VCH, Weinheim, 2010.

[17] H. R. Griem. *Principles of Plasma Spectroscopy, 2nd Edition.* University of Maryland, College Park, 1997.

[18] Abramowitz and Stegun. *Handbook of Mathematical Function.* National Bureau of Standards, Department of Commerce U.S., 1964.

[19] J Cooper. Plasma spectroscopy. *Reports on Progress in Physics*, 29(1):35, 1966.

[20] BWTEK. Spectrometer introduction. http://bwtek.com/spectrometer-introduction/.

[21] Vinay C. Raj and S. V. Prabhu. Measurement of surface temperature and emissivity of different materials by two-colour pyrometry. *Review of Scientific Instruments*, 84(12):124903, 2013.

[22] I. Zammuto, L. Giannone, A. Houben, A. Herrmann, and A. Kallenbach. Long term project in asdex upgrade: Implementation of ferritic steel as in vessel wall. *Fusion Engineering and Design*, 98:1419 – 1422, 2015. Proceedings of the 28th Symposium On Fusion Technology (SOFT-28).

[23] C. Zhang, E. Gauthier, C. Pocheau, C. Balorin, J.Y. Pascal, M. Jouve, M.H. Aumeunier, X. Courtois, Th. Loarer, and M. Houry. Surface temperature measurement of the plasma facing components with the multi-spectral infrared thermography diagnostics in tokamaks. *Infrared Physics and Technology*, 81:215 – 222, 2017.

[24] Y.S. Touloukian and D.P. DeWitt. *Thermal radiative properties: metallic elements and alloys*. Thermophysical properties of matter. IFI/Plenum, 1970.

[25] Adam Mazikowski and Krzysztof Chrzanowski. Non-contact multiband method for emissivity measurement. *Infrared Physics and Technology*, 44(2):91 – 99, 2003.

[26] R. Matyszkiel T. Piqtkowski M. Szulimm Z. Bielecki, K. Chrzanowski. Infrared pyrometer for temperature measurement of objects of both wavelength- and time-dependent emissivity. *Opt. Appl.*, 29(3):285–292, 1999.

[27] B. Sieglin. *Private communication*. 2017.

[28] B.Sieglin. Real time capable infrared thermography for asdex upgrade. *Review of Scientific Instruments*, 86(11):113502(1–6), 2016.

[29] B. Sieglin. Pelicand cameraccalibration (internal link). http://www.aug.ipp.mpg.de/~bsieglin/PelicanD/calibration/S9_A/2015_09_08_no_window/index.html.

[30] High heat flux facility GLADIS: Operational characteristics and results of W7-X pre-series target tests. *Journal of Nuclear Materials*, 367–370, Part B:1444 – 1448, 2007.

[31] Dr. Georg Maurer GmbH Optoelektronik. Non-contact temperature measurement. http://www.maurer-ir.de/index.php/en/component/content/article/68.html.

[32] Jui teng Lin and Thomas F. George. Laser-generated electron emission from surfaces: Effect of the pulse shape on temperature and transient phenomena. *Journal of Applied Physics*, 54:382, 1983.

[33] Carslaw and Jaeger. *Conduction of heat in solids*. Oxford University Press, University of York, Heslington,York UK, 1986.

[34] A. Herrmann. Hitzeschild thermographie (internal link). http://www.aug.ipp.mpg.de/~ircd/, 1998.

[35] V. Rohde, R. Dux, A. Kallenbach, K. Krieger, and R. Neu. Wall conditioning in asdex upgrade. *Journal of Nuclear Materials*, 363:1369 – 1374, 2007. Plasma-Surface Interactions-17.

[36] CeramOptec. Optran polymide uv/wf. `http://www.ceramoptec.de/en/products/fibers/optran-uv-wf.html`.

[37] A. Herrmann. *Wärmetechnische Kriterien für die Optimierung Trägheitsgekühlter Divertoren*. 25 November 1999.

[38] A. Herrmann. Limitations for divertor heat flux calculations of fast events in tokamaks. *Contribution at the 28th EPS Conference on Controlled Fusion and Plasma Physics*, pages 2109 – 2112, 2001.

[39] N. den Harder. *Private communication*. 2017.

[40] A. Herrmann. Shine through data and safety levels for fast control system (internal link). `http://www.aug.ipp.mpg.de/~ircd/`.

[41] R. Dux. *Private communication*. 2017.

Name: Raheesty Devi Nem Matrikelnummer: 784943

Erklärung

Ich erkläre, dass ich die Arbeit selbständig verfasst und keine anderen als die angegebenen Quellen und Hilfsmittel verwendet habe.

Ulm, den .....

Raheesty Devi Nem